# Accurate Characterisation of Refractive Components for Future CMB Missions

A thesis submitted for the Degree of

**Master of Science**


Presented by

**Niall Tynan B.A.(Phy) P.G.Dip.(Phy)**




**Maynooth University Department of Experimental Physics,**

**Maynooth University,**

**Maynooth, Co. Kildare, Ireland.**


**07 June 2016**

Department Head

Prof. J. Anthony Murphy

Supervisor

Dr. Marcin Gradziel

# Table of Contents

## Abstract

The focus of this thesis is on the experimental verification and computational modelling of refractive components for operation in the terahertz frequency band for future missions to measure the Cosmic Microwave Background (CMB) radiation. The specific components that were characterised were a set of dielectric lenses. These were made as part of a European Space Agency contract to further the refractive technology in the terahertz band of the frequency spectrum. Two different types of prototype lens were made for this project in Cardiff University and testing performed at Maynooth University (MU) and Cardiff University. An antireflection coating was applied to the prototype lenses and measured to test its effectiveness. During the manufacturing process some issues were detected, including a difference in refractive index between the finished lens and the sample batch material. In addition the lenses were found to have become warped during the application of the antireflection coating. This was due to the material not undergoing an annealing process before manufacture of the lenses.

The measurements carried out helped to identify and resolve the discrepancy between the refractive index of the test batch supplied, used to measure refractive index, and the actual lens, through comparison with the model developed and the simulations carried out by the TICRA company in Denmark. The measurements also tested the coating that was applied to the lens surface and confirmed good performance at 100 GHz and fall off at a lower frequency of 75 GHz, as expected. After an initial set of measurements of the lenses, improvements were made to the alignment system and the lenses were retested. This resulted in measurements with reduced offsets of the components in the system.

A computer simulation of the measurement setup was performed using an in house software package called Maynooth Optical Design and Analysis Laboratory (MODAL) to assess the accuracy of the measurements and test the model. The model showed good agreement between the feed horn measurements and simulations for all horns. The offsets in the physical system had to be included in the model in order to obtain agreement between the real and modelled systems. Computational simulations were performed for the uncoated lenses and showed good overall agreement but discrepancy in the comparison with high resolution measurements.

Results of simulations of coated lenses differed from the measurements since the coating was not implemented in the computational model.

# Chapter 1: Background Theory and Work

## 1.1 Introduction

In the early part of the 20th century cosmologists were developing new ideas on the origin of the Universe. There were two main competing models called the 'Steady State Model' and 'The Big Bang Theory'. The discovery of radiation called the Cosmic Microwave Background (CMB) led to the Big Bang Theory being favoured as the model for the formation of the early Universe. The CMB signal is the only signal in nature which conforms most precisely to a blackbody. The temperature of the blackbody is 2.73 K with the peak frequency of the blackbody at 282.8 GHz. Its discovery has led to the development of new instruments to measure this weak signal, in particular space based telescopes. This has driven the technological development of sub-mm wave telescope systems, both in terms of optical design and receiver electronics.

Missions such as COBE and WMAP to study the CMB marked a transition from purely theoretical cosmological work on the formation of the Universe, to experimental testing and verification of these theories. One of the most recent missions was Planck. It was designed to very accurately measure the variations in the temperature of the CMB across the sky giving us a sky map of the CMB. This gave us insights into the structure of the early Universe and allowed for the testing of theories to obtain a better understanding of our origins. As such, the development of high performance optical and electronic components and computer aided design of optical systems has enabled us to gain greater understanding of the early Universe, by measuring and analysing the features of the CMB.

While progress has been made in quantifying the CMB, some of its features, expected to be within the signal, still remain to be detected. This has led to a call for proposals to further the technology of optical systems to enable increased measurement sensitivity of the CMB. This chapter covers the background leading to the research topic on which the work completed for this thesis was based.

## 1.2 First theories on the origin of the Universe

With the technological advances made in the early 20th century there was an increase in observation of the distant Universe. This led to development of new theories to explain the phenomena observed in the Universe as well as the formation of the Universe itself. In 1946 a Russian scientist, who was working in America, named George Gamow proposed an idea of a Universe expanding from a central point. Gamow and his collaborators proposed the Universe expanding from a substance of electrons, protons and photons, referred to by the term ylem by R. A. Alpher and G. Gamow. (Alpher, Bethe and Gamow 1948)

Another theory was being proposed at the same time by a group of scientists led by Fred Hoyle. They proposed a Universe that exists and has existed in a continuous state for an infinite amount of time. This theory was known as the 'Steady State' theory. Hoyle was given time to broadcast his theory with a sequence of aired shows on the BBC in 1949. In these he referred to Gamow's theory as the 'Big Bang Theory' in an attempt to make it seem simple. This was in fact the first mention of the 'Big Bang Theory', which would go on to be more widely accepted by the scientific community. The theories were put forward but at the time there was no way in which to verify them. Ralph Alpher and Robert Herman published a paper shortly after Gamow in 1948 that predicted the level of the afterglow that should have been left in the Universe if such a big bang had occurred. If this signal could be detected it would push the Big Bang Theory to the fore as the best explanation for the origin of the Universe as we see it. (Alpher and Herman 1948)

In 1959 a new telescope was built to support Project Echo. This project was to enable communication between two stations on the ground by reflecting the signal from the ground based emitter off a high altitude balloon. The ground based receiver was a horn antenna called the Holmdel Horn Antenna, located in Holmdel, New Jersey. In order to extract the weak signal coming from the balloon the background signals had to be removed. The astronomers using the antenna in 1964-65 were Dr. Arno Penzias and Dr. Robert Wilson. They removed the known effects of radar and radio broadcasting and cooled the telescope to 4 K to minimise receiver noise.

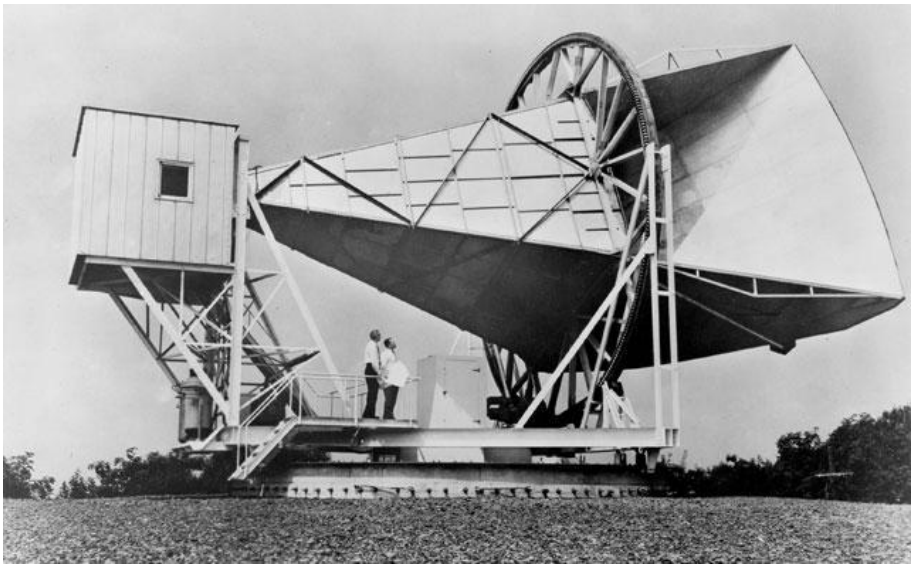

Picture 1: The Holmdel Horn Antenna used to perform the first detection of the CMB.

Despite these precautions they noticed a residual low constant signal that could not be accounted for. The signal was spread uniformly over the sky and present day and night. They discounted the possibility of the source being the Sun, Earth or the Galaxy. It now became an extraterrestrial signal that had to be explained. It was subsequently linked to the Big Bang theory and identified as radiation from the Big Bang. This was a monumental discovery for which Penzias and Wilson were awarded the Nobel Prize in physics in 1978. Following this discovery further work was required to measure, understand and extract information from this the oldest signal in the Universe, the Cosmic Microwave Background. (Bradley and Dale 2007)

## 1.3 Cosmic Microwave Background (CMB)

The Cosmic Microwave Background (CMB) radiation was produced by the Big Bang at the beginning of the Universe. Early in the Universe's formation there is expected to be a period of rapid expansion called Inflation. This rapid expansion is believed to have generated gravitational waves that cause stretching and compression between points in space. The Universe then experienced a period of gradual expansion and cooling. Due to the very high density of energy and thus heat, at this stage of the Universe's history no atoms could form. The Universe was thus in a highly coupled state with photons continuously interacting with the charged particles. Photons were unable to travel large distances due to these interactions and therefore had a small mean free path. Eventually the Universe cooled sufficiently for hydrogen to form. This period

of the Universe's evolution is called the recombination. The mean free path of the light increased dramatically because of this reduction in the number of free charged particles to interact with. It took place approximately 380,000 years after the Big Bang and is the period from which we see the oldest light in the Universe, the Cosmic Microwave Background radiation.

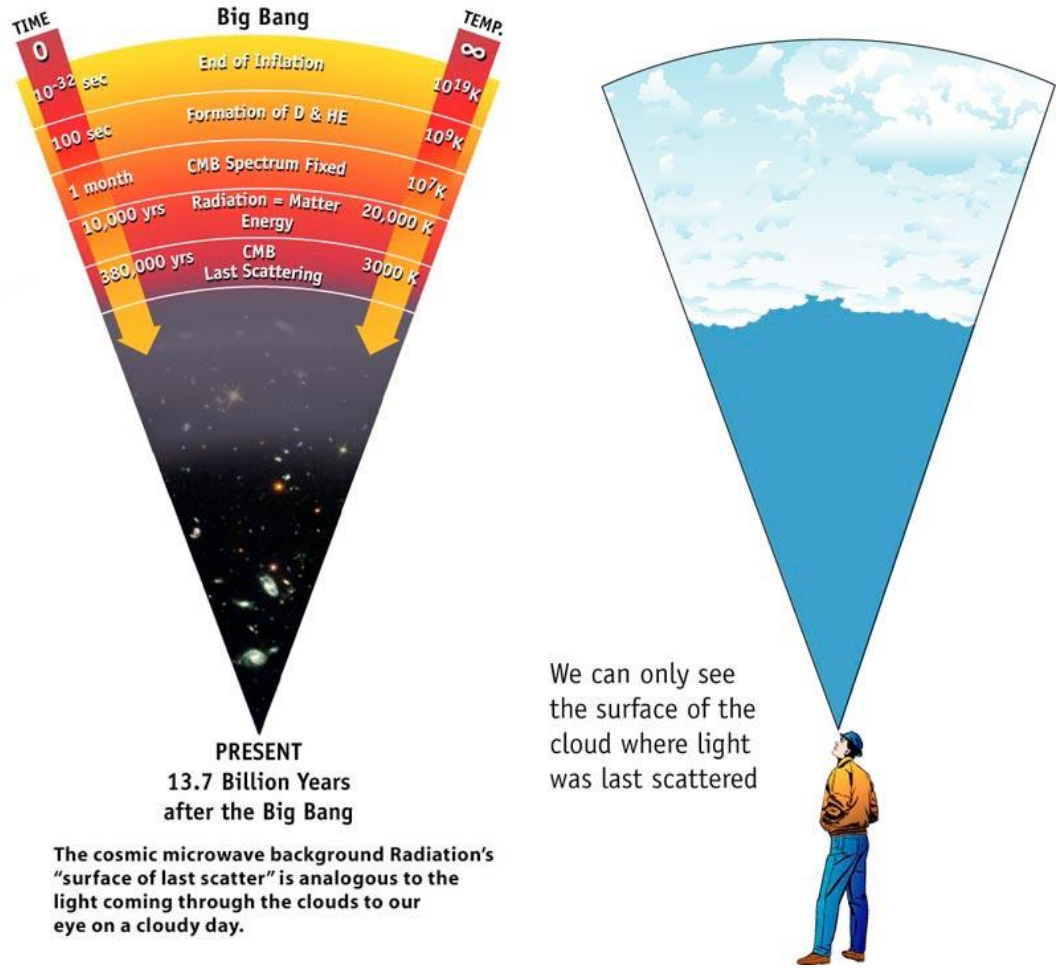


Figure 1: Descriptive diagram to describe the last surface of scattering for the CMB. Image source (NASA 2012).

Due to the short mean free path of photons in the early Universe all the information we receive is from after the recombination period. The matter with which the photons last interacted with is called the surface of last scattering; see Figure 1. From the Big Bang onwards the Universe has been expanding with a speed greater than the speed of light. This means the photons from the Big Bang have not been able to travel fast enough for all to have passed our position in the Universe. From our position we can therefore see this light from 380,000 years after the Big Bang arriving from all around us. We see these photons arriving from the last charged particle they interacted with but

this is not always from the surface of last scattering. During its journey to the receiver the photon can interact with other particles. This is a secondary scatter that affects the properties of the radiation. Large gravitational fields affect the radiation through gravitational lensing.

The interaction of the photons with the charged particles is typically through a process of scattering known as Thompson Scattering. This involves absorption of the light by the charged particle and subsequent re-emission in a random direction. Assuming the radiation incident on the particle is uniform, with no net polarisation, and incident on the particle from the opposite side to the observer, they will also see an unpolarised signal. Photons incident on the particle from a position other than directly behind will generate polarised scattered signal. This is because the electric and magnetic fields have to be perpendicular to the direction of propagation.

If the radiation from all directions around the particle is uniform there will still be no net polarisation as the influence from every direction separated by 90 degrees will balance. Net polarisation of the light will only result if there is a higher intensity of light from a particular direction. This can be caused by temperature difference between the two directions. Figure 2 shows an example with the regions separated by 90 degrees to each other causing a net polarisation in the direction of the cold region due to higher intensity radiation from the hot region. (Hu and White, A Polarisation Primer 1997)

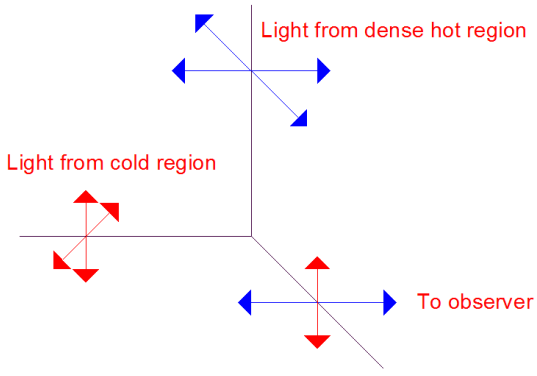


Figure 2: Thompson scattering is the scattering of light by an intervening charged particle. In this example hot and cold regions in the early Universe are separated by 90 degrees we get a net polarisation pointing towards the cold region due to higher intensity from the hot region. This polarisation contributes to the E-mode of the CMB. In the image above the hot region corresponds to the light from the blue arrow and the cold region the light from the red arrow.

Density perturbations in the early Universe cause scalar effects on the signal we observe. This scalar effect on the CMB creates a distinguishable effect in the

polarisation pattern we observe. The pattern caused by scalar effects has a purely gradient component to the polarisation pattern. The pattern is called the E-mode.

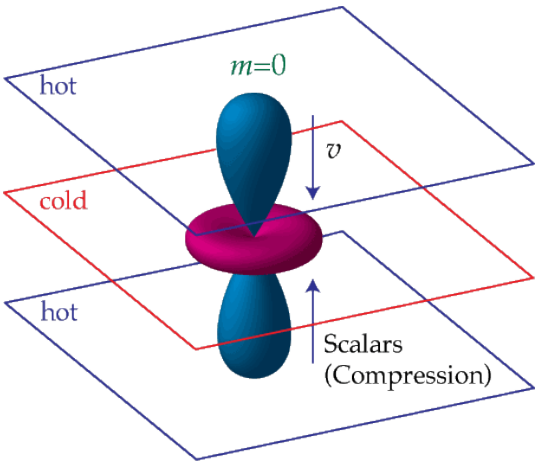


Figure 3: Representation of a scalar effect influenced by the distribution of radiation around a particle. Image source (Hu, Quadrupole Types and Polarisation Patterns 2001).

The gravitational waves caused by Inflation in the early formation of the Universe are believed to have also indirectly affected the CMB signal. It is believed that these waves left a signature that should be detectable in the divergent component of the CMB. Polarisation with a divergent pattern is called the B-mode. This effect on the CMB would be very small and thus hard to detect. Any matter it interacts with on its way from the surface of last scattering to our telescopes also affects the CMB radiation. This can cause gravitational lensing that leads to some of the stronger E-mode signal being coupled to the B-mode or creating a false B-mode component in the radiation.

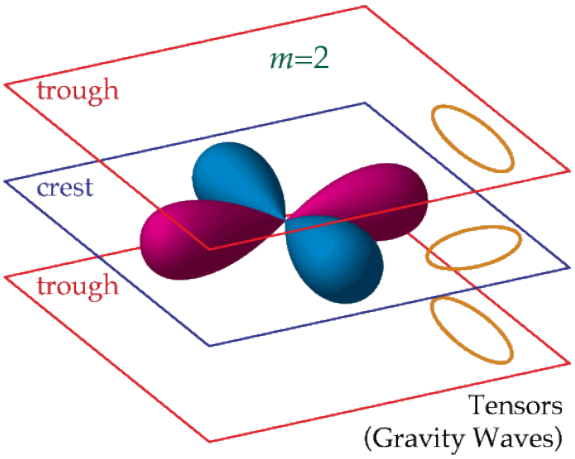


Figure 4: Representation of the effect on a particle by tensor effects. Image source (Hu, Quadrupole Types and Polarisation Patterns 2001).

The divergent polarisation pattern, B-mode, of the CMB would have a very different pattern across the sky from the curl polarisation pattern, E-mode, and can thus

be distinguished from it. In Figure 5 we can see the change in polarisation across the sky depending on the effect causing the pattern.

Figure 5: On the left is a representation of the E-mode polarisation pattern. The right shows the polarisation pattern associated with the B-mode. Image source (Team B-Pol 2007).

## 1.4 First Space Based Missions to Measure CMB

Since the initial discovery of the CMB, several satellites were designed to measure the CMB radiation. COBE was a space telescope designed by NASA and launched on November 18$^{th}$ 1989. It was the first mission designed to measure the CMB, using three onboard instruments. The Far Infrared Absolute Spectrophotometer (FIRAS) allowed measurement of the intensity CMB across a wide frequency range to determine how close the CMB radiation is to a black body. The Differential Microwave Radiometer (DMR) was used to measure variations of the CMB across the sky. The Diffuse Infrared Background Experiment (DIRBE) was used to measure emission from cold dust clouds. (Boggess, et al. 1992)

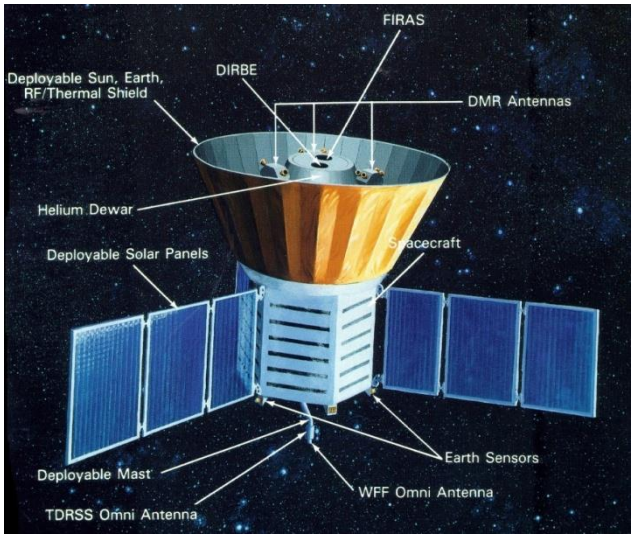


Picture 2: Pictorial depiction of the COBE satellite after launch. Image source NASA.

COBE succeeded in measuring the CMB across the sky creating the first sky map of the CMB using the DMR instrument. The DMR consisted of three radiometers measuring different frequency bands centred on 31.4, 53 and 90 GHz. The radiometers are fed by two horns placed on opposite sides of the spacecraft and angled at 30 degrees with respect to the central axis of the spacecraft. The radiometer therefore measures the difference between two points on the sky separated by a 60° angle with an angular resolution of 7°. This data was analysed and a power spectrum map was created of the sky seen in Figure 6.

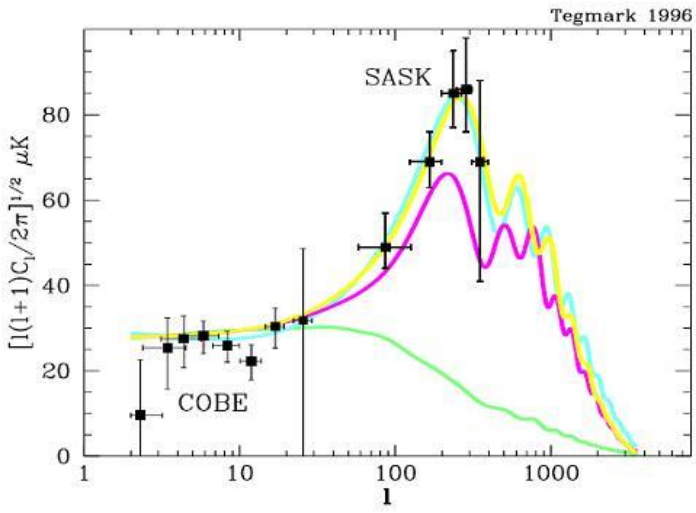


Figure 6: Power spectrum data points from COBE compared against theoretical CMB model curves for the power spectrum derived by Sugiyama (1995).The *x*-axis is the multipole moment numbers and the *y*-axis is the temperature variance. The vertical error bars include pixel noise and cosmic variance. The horizontal error bars show the window function used. Image source (Tegmark 1996).

COBE had shown the CMB signal is the best blackbody in nature. The temperature of this blackbody has changed on its journey as the photons wavelengths have stretched with the expansion of space. This results in a blackbody power distribution consistent with a temperature of 2.73 K. At this temperature the peak in intensity lies at a wavelength of 1.06 mm with equivalent frequency of 282.8 GHz. The CMB telescopes therefore had to be designed to measure the signal close to this wavelength or frequency.

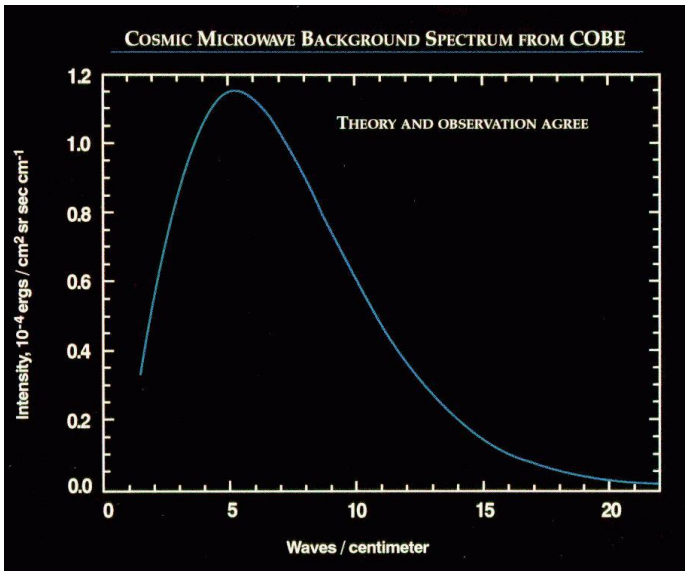


Figure 7: Black body curve for the Cosmic Microwave Background. Image source (NASA 2013).

Another satellite mission was sent in June 2001 to take more accurate maps of the CMB. It was called the Wilkinson Microwave Anisotropy Probe (WMAP). The objective was to take further measurements of the CMB detecting the anisotropies with an increased sensitivity and angular resolution over COBE. WMAP used a similar optical configuration as COBE with a two mirror telescope feeding an array of ten horns on opposite sides of the spacecraft. Each horn was designed to receive a different frequency band. The horns bands were centred around the following frequencies: one horn for a band centred on 22 GHz, one for 30 GHz, two for 40 GHz, two for 60 GHz and four for 90 GHz. The angular resolution of the telescope ranged from 0.23° at 90 GHz to 0.93° at 22 GHz. The project ran until 19th of August 2010 collecting data and produced the best power spectrum of the CMB at the time, as seen in Figure 8.

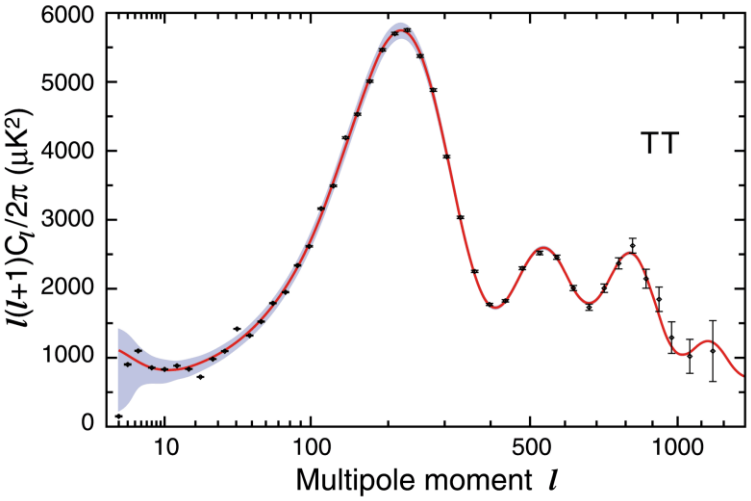


Figure 8: Nine year results from the WMAP telescope showing the power spectrum. Compared to the COBE power spectrum we can see more data points at smaller angular size and reduced error bars which has reduced the number of possible models. Image source (Bennett, et al. 2013)

The results, shown in Figure 8, are vastly improved over those in Figure 6. The error bars on the data obtained at low multipole order are greatly reduced and there is more data at higher multipoles. This considerably constrains the possible values for parameters in competing cosmological models.

## 1.5 Latest CMB Missions

A ground based telescope, called QUaD, was used to measure the CMB in two frequency bands centred at 100 and 150 GHz. This telescope was based at the South Pole and was a combination of two experiments, the Q and U Extragalactic Survey Telescope (QUEST) and the Degree Angular Scale Interferometer (DASI). It was designed to quantify the CMB signal with high angular resolution and good signal to noise ratio. The results were to be used with the WMAP measurements to apply constraints to the cosmological parameters and attempt to measure or constrain the possible level of the B-mode component of the CMB. Most CMB experiments use optical systems designed entirely using mirrors. QUaD used a combined optical system of two mirrors and two lenses (O'Sullivan and Cahill 2008).

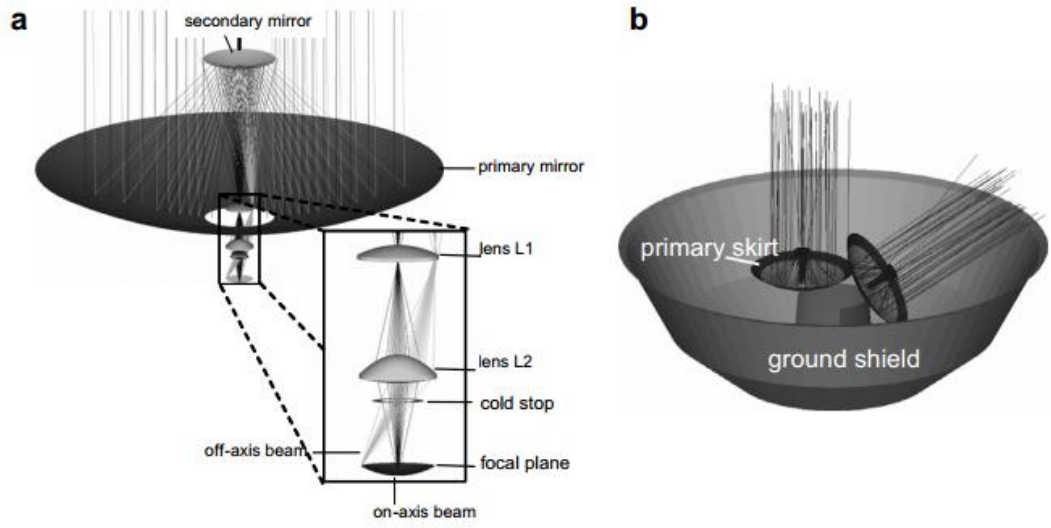


Figure 9: (a) The QUaD telescope front-end optics. (b) The telescope (shown in two positions) with the ground shield and the skirting around the primary mirror. Image source (O'Sullivan and Cahill 2008).

Results from the QUaD experiment constrained the values for the cosmological parameters beyond those reached by WMAP. The mission also put constraints on the upper limits of the B-mode signal power level. With new limits set for the signal level of the CMB a mission needs to be designed with increased sensitivity to measure signals below this upper limit. (Brown, Ade and O'Sullivan 2009)

Planck was launched by the European space agency on 19th of May 2009 with the goal of taking at least two full sky maps with higher sensitivity and resolution than any previous mission. The mission succeeded in taking five maps of the sky and was shut down on 23rd of October 2013. The satellite contained two instruments, the low frequency instrument (LFI) and the high frequency instrument (HFI). LFI was designed to operate at frequencies from 27 to 77 GHz using an array of 22 horn antennas. HFI was designed to operate at frequencies from 84 GHz to 1 THz using 52 bolometer detectors. (ESA 2009)

The surveys completed by Planck produced the best power spectrum, in both resolution and sensitivity, of the CMB so far. As such it allowed us to further constrain cosmological parameters and removed uncertainty in the data values at higher multipole moments, see Figure 10. (Planck Collaboration 2014)

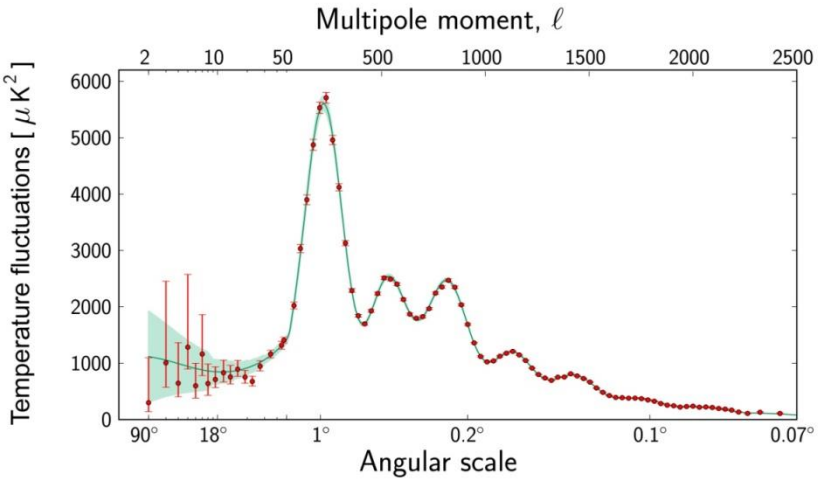


Figure 10: Planck power spectrum data. The data extends to lower angular scale and has reduced error bars compared to the work done by WMAP. Image source (Planck Collaboration 2014).

Background Imaging of Cosmic Extragalactic Polarisation (BICEP) is a recent project aimed at measuring the B-mode component of the CMB. It is a ground based telescope located at the South Pole. BICEP has had two incarnations so far, with BICEP2 recently releasing what was thought to be the first measurement of the B-mode component of the CMB although subsequently it was announced that this was likely due to polarised foregrounds. A further project, BICEP3, started operation in the summer of 2014 and will try to succeed in quantifying the B-mode component of the radiation. This detection would give us an incentive to return to space in order to measure the B-mode component of the CMB across the entire sky. The detection of the B-mode component of the CMB would provide support for inflation theory and would affirm our understanding on the development of the early Universe.

Further results from Planck have been released in 2015 from analysis of all the work done by Planck and including results from BICEP2 and the Keck array. This has led to increased precision on cosmological constants and a lower upper limit on the level of the B-mode component of the radiation. The information is displayed as the ratio of tensor to scalar component of the CMB, tensor being the B-mode and scalar the E-mode. This ratio is now confined to less than 0.09. This information leads to some inflationary models being disfavoured and provides us with a minimum level of sensitivity for the next satellite designed to measure the CMB in order to detect the B-mode component of the radiation. (Planck Collaboration 2015)

## 1.6 Proposed Mission, B-Pol, Background

In 2005 the European Space Agency called for proposals for space missions set to launch from 2015-2025. In this proposal ESA outlined their cosmic vision, which is the set of questions about the Universe they intended to answer during the set of missions from 2015-2025. The questions were split into four sections. The first was to answer questions on the formation of planets and the requirements for habitable planet environments. The second was to solidify our knowledge of the solar system and the planets within it. The third was to determine the physical laws of the Universe including the first detection of gravity waves from the Big Bang. The fourth was to increase our knowledge of the early Universe and its formation.

In order to answer the third question, to detect gravity waves, and as part of the fourth objective, to gain further knowledge on the formation of the Universe, a mission called B-Pol was proposed. The proposal was prepared by a large collaboration of scientists from different institutions. Roles were divided into three groups to work on different technical areas of the project and a fourth group of coordinators for the project. One group was dedicated to designing the telescope instrument, another to work on the background science and the final group's task was to identify and create ways to remove noise present in the signal from foregrounds.

A full list of collaborators can be found using the following citation (B-Pol collaboration 2007). This mission's aim was to detect the primordial gravitational waves of the CMB through detection of the B-mode component of the CMB signal. A telescope was designed as part of this proposal in order to achieve these objectives. To determine the requirements of the telescope required to detect this signal, comparison was drawn with previous missions. The Planck telescope was predicted to measure the E-mode with increased sensitivity and set an upper limit on the level of the B-mode component of the CMB but was not expected to be able to measure the B-mode. A new telescope will therefore have to be made with increased sensitivity over Planck. In addition it will be informed by the upper limit set by Planck for the B-mode component of the signal.

The type of telescope was then considered. It was determined that a space based rather than ground based telescope would be used. A space based telescope allows for reduction in the noise received compared to a ground based telescope, with fewer

sources from the surrounding environment, and freedom to measure a complete sky map. The telescope also needed to measure the radiation at large angular separation due to the statistical weight of the signal residing at these large angular separations. The telescope was also designed to measure a large range of frequencies split into separate frequency bands. For the CMB the main peak of the blackbody curve lies at 282.8 GHz. At this frequency there is strong noise from Galactic dust clouds and thus cannot be used. Different frequency bands with the least noise but close to the blackbody peak frequency have to be chosen. Previous ground and space based missions have informed us and thus two bands are chosen at 100 and 150 GHz for measurement of the CMB.

Noise is still present in these frequency bands from foreground sources. The WMAP mission measured frequency bands from 23-94 GHz and found that the foreground contamination of the signal could be separated into four distinct components. The first is caused by synchrotron radiation from electrons in the Galactic dust cloud. The second is caused by free-free emission from the diffuse ionised medium. The third is caused by thermal emission from dust heated by the interstellar radiation field. The fourth is caused by an anomalous signal correlated to the thermal dust emission most likely caused by rotational modes of excitation of small dust grains. (Bennett, Halpern and Hinshaw 2003)

In order to remove noise from the signal created by synchrotron radiation two frequency bands are measured at 70 and 45 GHz as the synchrotron noise is most dominant in these frequency bands. Noise is also present from thermal dust emission. The emission is strongest at higher frequencies. Therefore two higher frequency bands at 220 and 350 GHz are measured to allow removal of the galactic dust cloud foreground. (Benoit and Ade 2004) Examples of the sky maps taken by Planck at different frequencies can be seen in Figure 11.

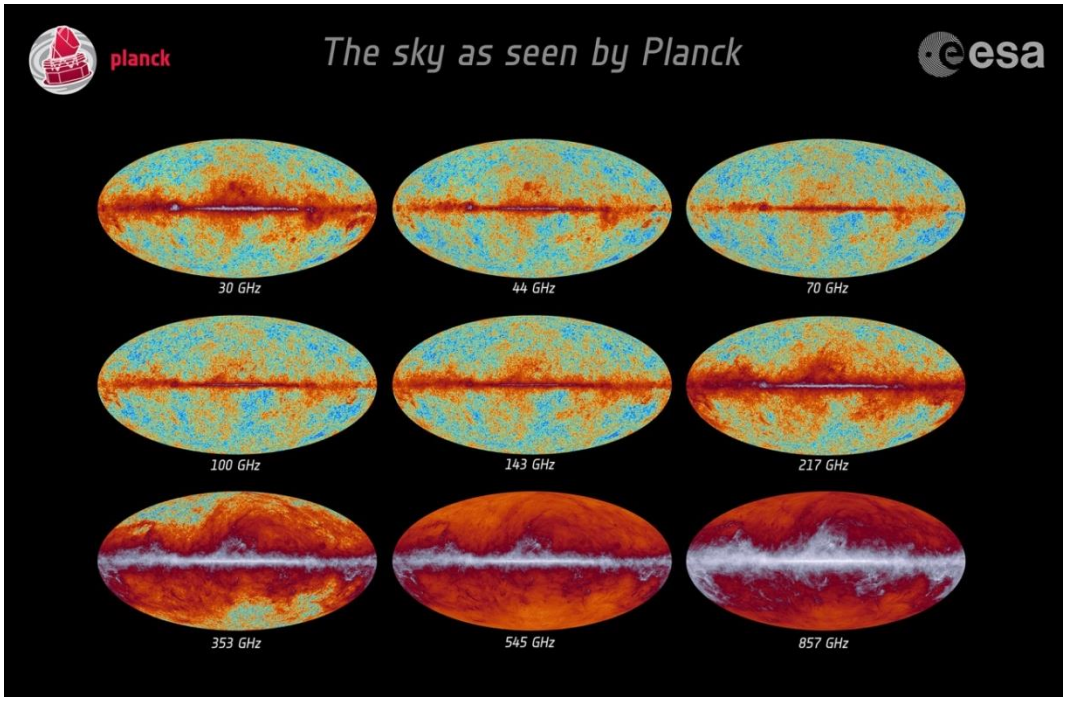


Figure 11: Sky maps from Planck mission for different frequency bands. Image source (ESA 2013).

The optical systems used in previous space based telescopes to measure the CMB have used reflective optical systems only. These systems involved a configuration of mirrors feeding an array of horns designed to measure different frequency bands. The use of one optical system for all frequencies leads to a compromise in the coupling to the receiver horns. The use of a refractive optical system would allow for better coupling to the horns, as the system would be sufficiently compact to allow separate optical systems for each set of horns measuring different frequency bands.

Refractive optics are not generally used in systems operating in the terahertz band due to the lack of precise knowledge of the performance of such refractive optical systems, although they were used as part of the QUaD telescope design. The precise knowledge of optical and mechanical properties of materials appropriate for use in such lenses is limited. The manufacturing procedure, its limitations and accuracy would also have to be verified as there is limited prior knowledge. A full telescope optical system can be comprised completely of reflective or refractive components, but it can also have a combination of both.

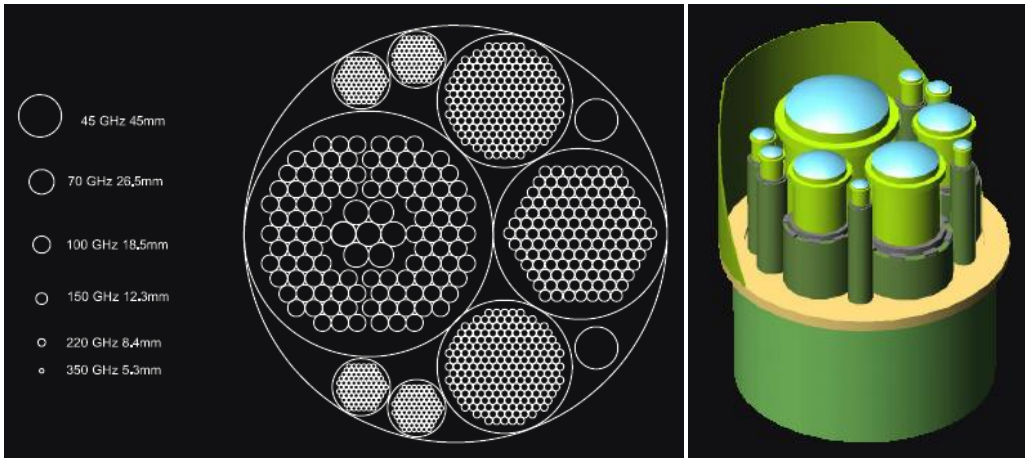


Figure 12: Telescope concept and receiver layout. Each set of receivers has a set of lenses specifically designed to suit the frequency band in which the receiver horns are operating. Image source B-Pol website (Team B-Pol 2007).

After considering all options an on-axis telescope with a purely refractive optical design was chosen as it met all the performance requirements for the mission and allowed for a compact medium sized satellite to be designed. The design consists of eight separate optical systems for each frequency band allowing for less compromise in the performance of the telescope at each frequency band. A significant amount of work needs to be done to develop the capability to manufacture the required lenses, before a telescope based on this design can be fully considered.

All previous space based missions to measure the CMB had used mirrors and thus the modelling techniques, manufacturing process and performance for the large lenses needs to be verified. To prove that these refractive optical components can be accurately modelled and manufactured, a set of prototype lenses will be produced. These prototypes are specifically designed to test the manufacturing and modelling techniques and are not designed for actual use in the proposed telescope. The main prototypes will be made to an appropriate scale for use in the testing systems. One prototype lens will be made to the full size proposed for the telescope in order to ensure the manufacturing process is capable of accurately creating the lens.

# Chapter 2: Prototype Lenses-Technology Development

## 2.1 Introduction

This section covers the initial work completed up to and including the manufacturing of the prototype lenses. This process involves four stages: (1) design of the lenses, (2) material analysis and the manufacturing process, (3) computational modelling and (4) prototype design. The design of the lens is covered in this chapter including formulas used for the design of the lens surface and the reasons for choosing the type of lens design. Cardiff University were responsible for designing the two types of prototype lenses, one for measurement in Cardiff University and one for Maynooth University.

Cardiff University performed material analysis of samples provided by different manufacturers in order to choose the best material for the lens design. This process involved accurate characterisation of the refractive index of the materials using multiple testing methods in order to ensure accuracy of the result. These testing methods are discussed in detail here. A description of the manufacturing process for both the lens and coating are also provided.

Tests were performed in order to determine the most efficient and reliable method to computationally model the lenses. These tests were performed by the TICRA company in Denmark. A description of the methods used for the computational modelling is covered including the chosen methods for final modelling of the lenses.

The lens design could only be finalised once the materials for the lens were selected. A description of the final lens designs will be discussed and a full list of the dimensions for the lenses provided.

## 2.2 Stage 1: Lens Design

The prototype lenses were designed with the measurement system with which they were to be tested in mind. The first lens design was a focusing lens to enable accurate

characterisation of the lens performance with the measurement system at Cardiff University, which uses an incoherent detector with fixed emitter and receiver. This system allows for measurement of the total power received after passing through the lens. This enabled assessment of the performance of the lens and the loss of power through reflection and internal losses. The lens was symmetric and double convex in order to focus the radiation from the emitter horn, placed at the focus on one side, to the receiver horn placed at the focus on the other side of the lens, as illustrated in Figure 13.

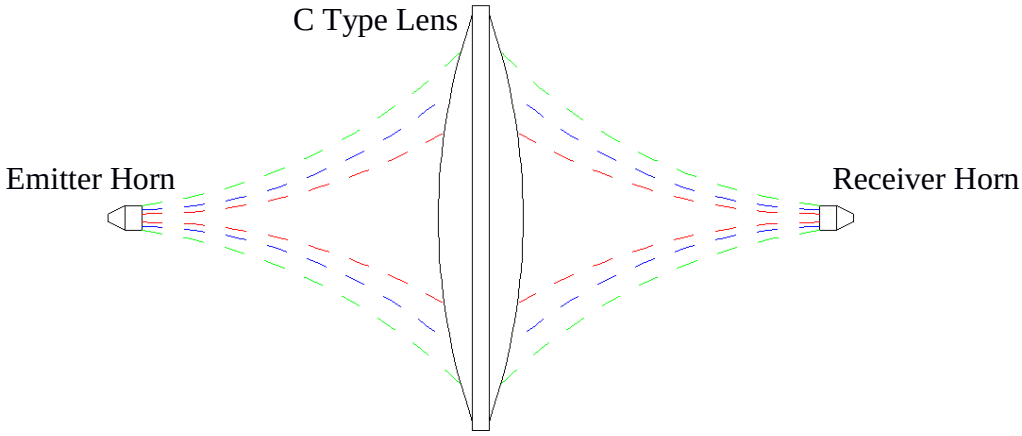


Figure 13: C type lens measurement setup. The emitter horn sends radiation through the prototype lens which refocuses the signal back to the receiver horn. (Not to scale)

The second lens is designed for use with the Maynooth University measurement system. This lens was designed to be a flat phase lens. As shown in Figure 14, as the beam of radiation travels from an emitter, the phase at the edge (point B) falls behind that of the centre of the beam (point A) due to the longer distance that it is required to travel. A flat phase lens alters the phase front of the beam so that at a particular distance after lens the phase front will have equal phase across the beam area, from the centre to the edge of the beam. Being a coherent detector the measurement system in Maynooth is capable of measuring both the power and phase of the radiation. It is able to measure the phase across a 2D plane using a scanning receiver probe and therefore determine the position were the phase front of the beam is flat. The distance from the lens to this position can then be compared to that expected by the lens design. To achieve this, the lens design was asymmetric and double convex.

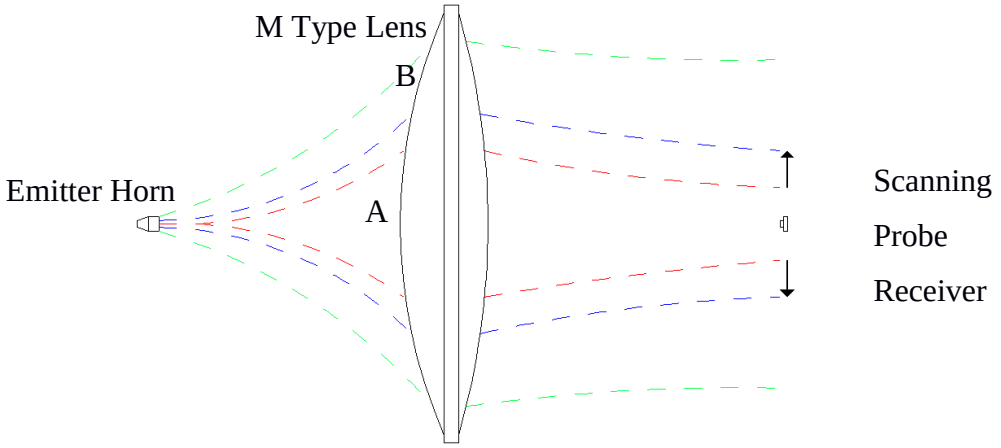


Figure 14: M type lens basic system setup. (Not to scale)

By using bi-hyperbolic lenses and matching the eccentricity to the refractive index of the lenses we can create a lens in which the focus of the hyperbolas matches the focus of the lens. This allows for very good beam predictions for comparison to the measurements and models. The lens surfaces were designed using the following hyperbolic equations:

Equation 1: Radius of curvature of the surface.

$$R = (n-1)f$$

Equation 2: Half-apex distance of surface.

$$a = \frac{R}{(e^2-1)}$$

Equation 3: Half-foci distance of surface.

$$c = ae$$

Equation 4: Half minor axis of surface.

$$b = \sqrt{c^2 - a^2}$$

In the above equations $R$ is the radius of curvature, $n$ is the refractive index, $f$ is the focal length, $a$ is the half-apex distance, $c$ is the half-foci distance, $b$ is the half minor axis and $e$ is the eccentricity. (Hargrave, et al. 2013)

Antireflection coatings are used in conjunction with lenses to reduce reflection from the interface surfaces of the lens. During transmission from one medium to another with differing refractive indexes part of the power will be reflected. In order to minimise this effect an antireflective coating is applied to the lens. This is essentially a coating with lower refractive index which reduces the change in refractive index from

one medium to another. The coating acts to match the impedance and create maximum transmission. The coatings performance is dependent on the wavelength of the incident light, as the coating will perform at maximum efficiency when the thickness equals a quarter of the wavelength of the incident light.

The antireflection coating is therefore designed to operate at a specific frequency with fall off in performance away from this central frequency. The performance also depends on the incident angle of the radiation to the surface of the lens and the polarisation angle of the radiation. For our work we assume the light to be incident perpendicular to the surface. This coating will be chosen to have a refractive index with a value equal to the square root of the refractive index of the material for the main body of the lens. In this case the polarisation of the radiation does not apply and the formula is reduced to what is seen in Equation 5.

Equation 5: The layer thickness formula for an antireflection coating with light incident normally to the surface. d is the thickness of the antireflection layer, $\lambda_0$ is the chosen wavelength in free space for perfect quarter wavelength matching layer and n is the refractive index of the bulk material.

$$d = \frac{\lambda_0}{4\sqrt{n}}$$

## 2.3 Stage 2: Analysis of Materials and Manufacturing Process

The next stage in the process is to determine the materials that will be used for the lens body and antireflection coating. It is important to find a material for the main body of the lens that has a refractive index which works in conjunction with the material used for the antireflection coating for maximum effect. Therefore materials would have to be tested to determine the refractive index of sample materials to determine the appropriate material for the lens body and antireflection coating. Previous work had been performed to determine the refractive index of materials at the frequencies we intended to use. In the book (Goldsmith 1998) a table of analysed materials is included from page 80-83. The table contains information on the refractive index measured for different materials including polyethylene.

The table has 13 different values for polyethylene showing the difference that can be caused due to analysis at different frequencies, from different manufacturers or of different batches of material from the same manufacturer. This is why a test batch of material from the manufacturer of the lens needs to be tested, in order to use the

measured refractive index for the material provided by the manufacturer for the lens design. The batch used to manufacture the lens was tested to obtain an accurate value for the refractive index. Testing two different batch samples from the same manufacturer also tests whether we can expect the refractive index to remain constant between batches. Consistent refractive index values will allow the lenses to be designed with the value with confidence that the lens will have the same refractive index and thus perform as expected.

Previous work has been done in the past testing and verifying the performance of refractive components in the THz frequency band. In (Goldsmith 1998) from Pg 71-97 the author describes lenses, their benefits, types and uses. Compared to lenses in the optical spectrum, lenses in the THz spectrum have many advantages. Due to the long wavelength the lens surface does not have to be polished to a high degree of smoothness, reducing the amount of care needed when manufacturing and using the lens. The lens can be manufactured from the material using a milling machine, which allows for the easy creation of aspheric lenses. Aspheric lenses allow for a lens that is significantly thinner at the extremities of the lens compared to its spherical equivalent. This reduces the weight in the lens a key consideration when designing a space based telescope.

For the purpose of creating prototype lenses, testing was performed by Cardiff University to assess the optical properties, specifically refractive index, of different materials for the lens design. The refractive index is a critical parameter that will affect the overall design of the lenses and determine the appropriate material to be used for the anti-reflective coating. It was therefore imperative that the refractive index be measured with the greatest accuracy possible for use in the computational modelling and design for the optical system. The refractive index was determined for the spectral range from 90-1200 GHz using a Fourier Transform Spectrometer (FTS) setup in a Martin-Pupplet configuration. Methods of both transmission spectroscopy and phase delay measurements were used in order to determine the refractive index of the materials.

Transmission spectroscopy compares the results from the system with and without the sample material in the path of the beam. Without the sample we will see full transmission through the system including any variations caused by the system. With the sample in place Fabry-Perot fringes appear caused by the standing waves created by presence of the sample. Comparing the two measurements we can eliminate the effects

caused by the system to give us the true Fabry-Perot interference pattern. This creates a sine wave effect seen in the total transmitted power measurement at different frequencies. Below is an example of the expected output after comparison between the reference and sample measurements.

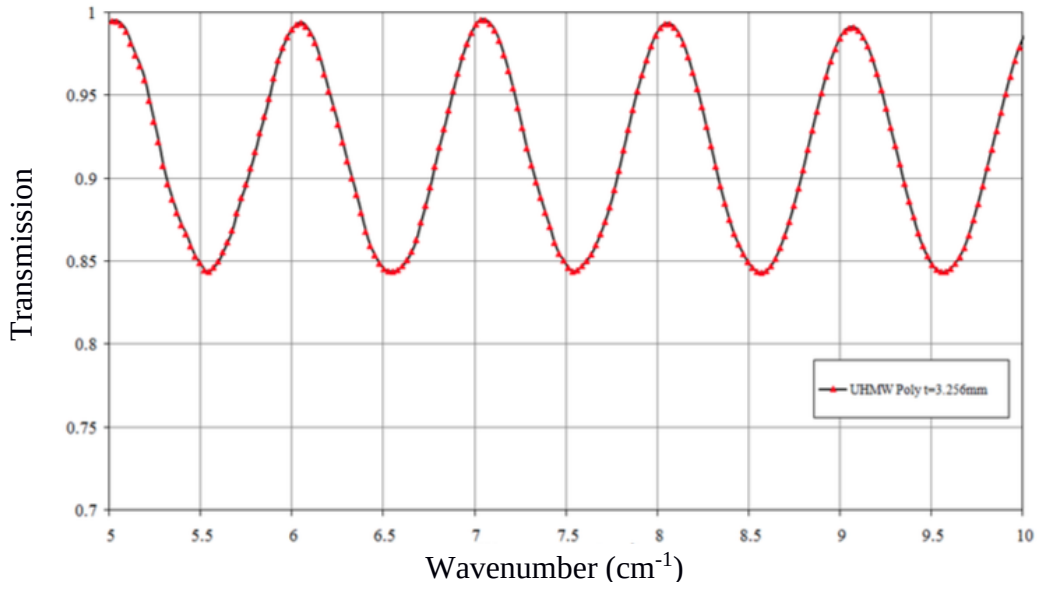


Figure 15: Results from sample measurement after normalisation with the background reference.

The phase delay measurements are based on the interference between the two beams in the spectrometer when the sample has been placed in one of the beam's path. This creates a phase delay from one beam that will then interact with the other beam to create destructive and constructive interference dependent on the wavelength of the light, thickness and refractive index of the sample material.

Different materials were tested to determine the refractive index including measurement of the same material from different manufacturers. Below is a table of the materials tested as part of this process and the refractive index values measured for them by Cardiff University. Two materials had to be chosen from those tested. The first was to be used for the main body of the lens. The second was to be used for the anti-reflective coating of the lens. (Hargrave, et al. 2013)

Table 1: List of material refractive indices from measurements performed by Cardiff University. Source (Hargrave, et al. 2013).

| Material | Refractive Index | Frequency Range |
|---|---|---|
| Polypropelene 1 | 1.5016±0.0005 | 90-1200 GHz |
| Polypropelene 2 | 1.5088±0.0001 | 90-1200 GHz |
| UHMW-PE | 1.5275±0.0008 | 90-1200 GHz |
| UHMW-PE (From C3 lens) | 1.51817±0.00006 | 90-1200 GHz |
| UHMW-PE (From annealed C3 lens) | 1.5174±0.0002 | 90-1200 GHz |
| Porous PTFE | 1.1541±0.0002 | 90-1200 GHz |

For the body of the lens a dielectric material called ultra high molecular weight-polyethylene (UHMW-PE) was used. The material sample tested was provided by a company called Ensinger Precision Engineering Ltd. and shown to have a refractive index of 1.5275±0.0008. This value of refractive index was used for the design of the lens but it became apparent that the actual value was different. One lens, called the C3 lens, was used to determine the actual refractive index by testing cuts of material from the lens. The refractive index was found to be 1.51817. There was also a change in refractive index after the lens was coated due to annealing of the lens material. A measurement of the sample after an annealing process but before coating was then performed in order to determine the refractive index of the lens after the annealing process. This was determined to be 1.5174. The coating material chosen was porous polytetrafluoroethylene (PTFE). The refractive index for this material over the frequency range was determined to be 1.1541±0.0002. The PTFE refractive index is close to the square root value of the UHMW-PE required for optimal function of the anti-reflective coating.

The lenses were manufactured by the machining company Ensinger Precision Engineering Ltd. using a computer numerical controlled machine to precisely shape the lens material. The surface of the lens will be shaped to match the hyperbolic surface calculated from the design equations. The refractive index from the test batch of 1.5275 was used for these designs. The actual refractive index value of 1.51817 was used in subsequent computational modelling.

The batch material should have undergone an annealing process before being used for the lens manufacture. This is done by heating the material to high temperatures in order to remove defects from the material. It was apparent after completion of coating the first prototype lens that the material had not been annealed. In order to take the

shrinking effect that occurs upon annealing into account for the future measurements as well as the change in refractive index, a separate annealing step is introduced between manufacture and coating. This meant placing the lens in a rig that allowed for the lens to warp as it was heated. The new refractive index obtained of 1.5174 was used in subsequent computational modelling.

The lens will be subsequently coated using a process developed in Cardiff University by Dr. Peter Hargrave and Dr. Giorgio Savini. The lens is placed in the coating jig. The coating material and glue layer is then fixed into an aluminium ring. A silicon rubber vacuum seal layer is then fixed into a separate ring. The rings of coating material followed by vacuum seal are then added to each side of the jig. The coating layer is then stretched down across the surface of the lens being stretched out to ensure even and flat coating across the surface of the lens. The coating is then pressed onto the surface of the lens by using a vacuum to extract the gas from inside the sealed area and allowing atmospheric pressure to apply the coating onto the surface of the lens. This enabled an even coating to be created in a repeatable process across the surface of the lens. The thickness of the coating used was 0.64 mm.

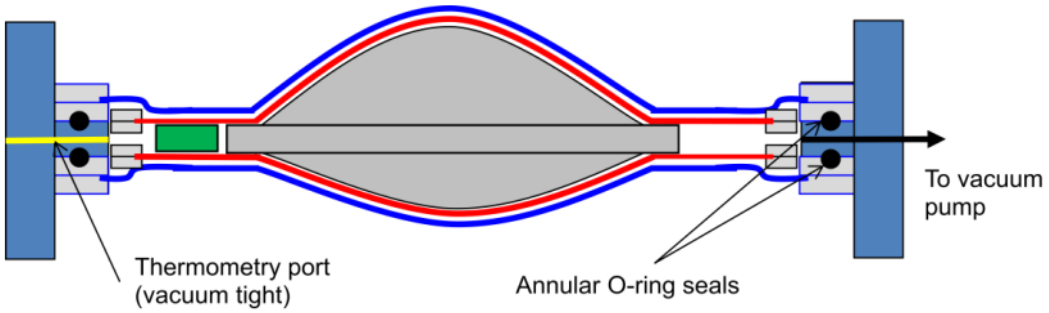


Figure 16: Coating process system used in Cardiff University to apply antireflection coating to the surface of the lens. The red layer is a combination of the coating material and a glue layer which is applied to the surface of the lens. The blue layer is a material to seal the system in order for the vacuum pump to create a confined vacuum. (Hargrave, et al. 2013)

## 2.4 Stage 3: Computational Modelling

Computational modelling is performed in order to predict the performance of our prototype lenses and to assess the accuracy of our models. The modelling was performed by the TICRA institute in Denmark for all the prototype lenses. Two different methods of modelling were compared; Physical Optics (PO) and Body of Revolution Method of Moments (BoR-MoM). The choice of modelling method to use

was based on the scenario being modelled and the accuracy and efficiency required. (TICRA 2005, Gibson 2008)

The physical optics method utilises Fresnel equations in order to calculate the interaction of an emitted field with the surface of a scatterer. This method is only applicable in high frequency systems but gives highly accurate and efficient results. The induced currents caused by the electric field on the surface of the scatterer are then calculated. From these currents the diffracted field can be created by explicitly calculating the integral of the fields present over the surface of the scatterer. This method has some approximations involved but allows for fast computational times.

The BoR-MoM is a combination of two methods that work for a symmetric system about an axis, body of revolution, and with discretisation of the scattering surfaces on which the induced electromagnetic field is calculated. The method of moments is used in order to create a set of integral equations for every discretised part of every scattering surface. This is similar to the PO method but whereas the PO method is done incrementally as the wave propagates through the system, in the MoM the fields on the surfaces of all the scatterers are determined and solved at the same time. Equations for the source electric and magnetic fields are determined. The surfaces are then discretised into sections with a set of functions derived to describe the interaction of the source field with each section of the surface.

Boundary conditions are then imposed in order to reduce the computational effort required to solve the system. The system is split into a set of sub domains and these are then described by a set of functions. The functions from each sub domain are then solved together in order to determine the field throughout the entire system. Boundary conditions must be imposed in order to create an efficient code to run. One boundary condition would limit the area in which the field's effect is calculated in order to limit the calculation time. This method has increased efficiency over field propagation through the entire volume of space. The MoM method has high accuracy and is only limited by the discretisation of the geometry being used. It does require a large amount of computational time for off-axis feeds.

In order to decrease the computational time for the method further, symmetry of the system can be used. Instead of calculating the field for the entire surface of the lens, the symmetry about the direction of propagation, due to the circular lens, can be used to apply the field calculated for one part of the lens to another. This is the BoR method.

For the purpose of determining if the PO method is sufficient for the modelling it was tested and compared against the BoR-MoM along with the Double PO method where an extra iteration of reflection is taken into account for the field. It was found that the methods are consistent for co-polar but differ for the cross-polar with PO being the most inaccurate method, see Figure 17. Due to these findings the PO method was used with the BoR-MoM method used to cross check for on-axis feed measurements and the Double PO method used as a cross check for off-axis feed measurements.

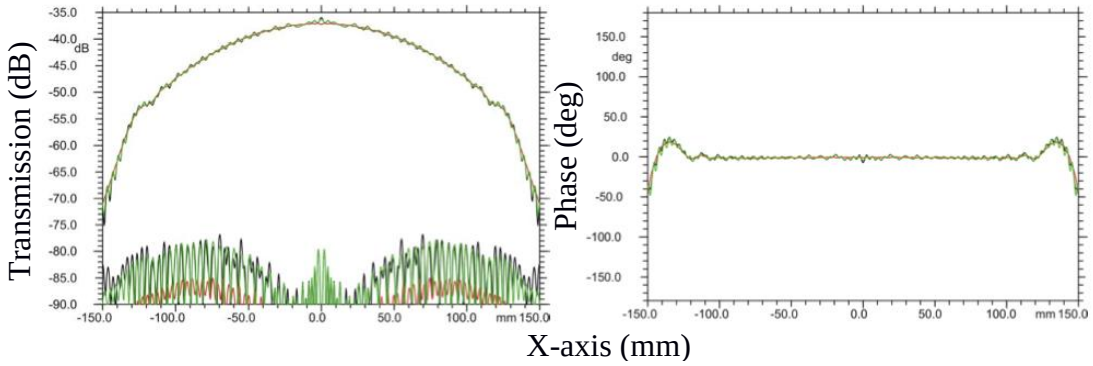


Figure 17: Comparison of modelling methods for the M type lens measurement system. The black line represents BoR-MoM method, the red line represents the PO method and the green line represents the Double PO method. Image source (Gradziel, et al. 2013).

The tests were then run with the anti-reflection coating included in the simulation. For the PO method the Fresnel estimation was replaced with refraction through a layered media. All methods were found to agree well except for the pattern at the centre where the BoR-MoM method is the only one to accurately predict the pattern of the cross-polar. This is believed to be due to edge effects caused by the coating layer.

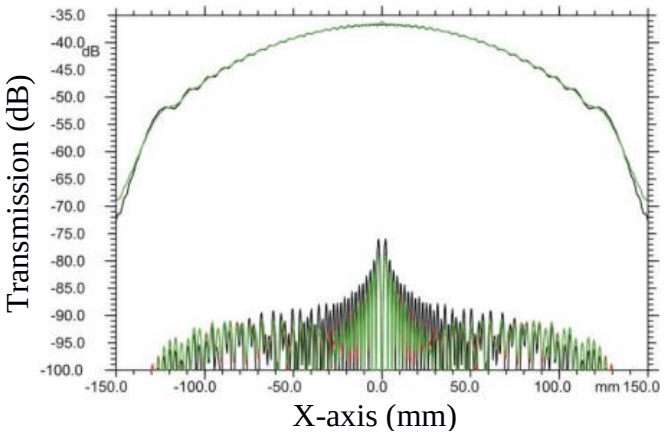


Figure 18: Comparison of the computational modelling methods for the M type lens measurement system including the anti-reflection coating layer. The black line represents BoR-MoM method, the red line represents the PO method and the green line represents the Double PO method.

## 2.5 Stage 4: Prototype Design

With the exact refractive index values for the materials to be used for the prototype lenses determined, the design of the lenses could be finalised for the measurement systems that were used to test the prototype lens performance. The measurement system in Cardiff University is an incoherent system with the purpose of measuring the total power received after the signal has passed through the device under test. The system consists of an emitter Gunn diode operating at 75 GHz with a frequency doubler, a 150 GHz Clover horn with back-to-back Winston feed horn to a cryostat with internal smooth-walled conical horn and a 4 K bolometer detector.

Due to the detector being incoherent a focusing lens was designed to couple the radiation from the emitter to the horn receiver for the total power measurement. This enables the loss through the lens due to reflection to be assessed and the performance of the anti-reflection coating to be verified. The lens is symmetrical with both sides having the same radius of curvature. In order to test consistency of the manufacturing process and to allow for unforeseen circumstances, three prototype focusing lenses were manufactured. The prototype lenses made with this design are called the C type lenses. The lens dimensions are shown in Figure 19.

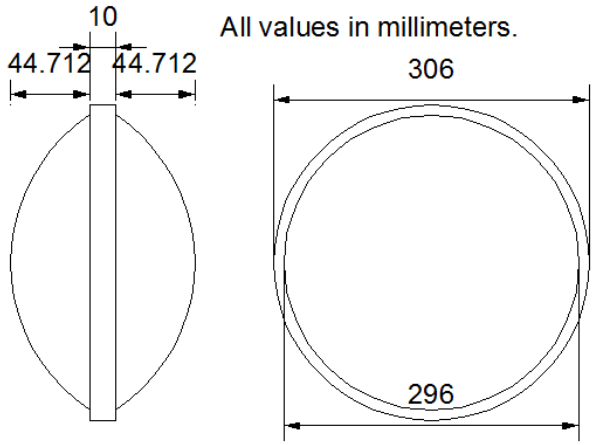


Figure 19: C type lens mechanical drawing. (Not to scale)

The design parameters for the lenses were calculated based on the refractive index of the test batch supplied by the manufacturing firm Ensigner Ltd. Table 2 provides the design parameter values used for manufacturing the C type lens.

Table 2: Table of C type lens parameters used for lens manufacture.

| Quantity | Value | Unit |
|---|---|---|
| Radius of Curvature | 198.8675 | [mm] |
| Conical Constant | -2.333256 | |
| Semi-diameter | 143 | [mm] |
| Half apex distance (a) | 149.159 | [mm] |
| Half minor axis distance (b) | 172.229 | [mm] |
| Half foci distance | 227.841 | [mm] |
| Focal distance (from lens surface to focus) | 377 | [mm] |
| Overall lens thickness at centre (t) | 99.424 | [mm] |

After manufacturing, the surface profile of the lenses was measured in order to assess the accuracy of the manufacturing procedure. The surface profile of the lens was measured to determine the curvature and the discrepancies in thickness from the design. These measurements were performed using the Mitutoyo coordinate measuring machine. The curvature of the lens along two central axes were measured, the *x* and *y* curvature. An average was then taken between these measurements. Table 3 below shows the recovered values for the manufactured lens.

Table 3: Table of C type lens parameters after manufacture. The radius of curvature, conical constant and thickness averages for surface of the lenses (S1 and S2) are shown.

| Lens | S1, R (mm) | S1, C | S1, T (mm) |
|---|---|---|---|
| C1 | 199.353±.030 | -2.355±.018 | 44.712±.081 |
| C2 | 199.428±.182 | -2.319±.009 | 44.810±.025 |
| C3 | 199.478±.054 | -2.346±.032 | 44.880±.194 |
| | S2, R (mm) | S2, C | S2, T (mm) |
| C1 | 199.255±.370 | -2.332±.002 | 44.805±.077 |
| C2 | 199.401±.038 | -2.342±.000 | 44.270±.039 |
| C3 | 199.336±.517 | -2.329±.023 | 44.766±.193 |

Maynooth University (MU) offered to measure the prototype lenses using a Vector Network Analyser system, fully described in chapter 3. The M type lens designed for MU was a flat phase lens rather than a focusing lens as the MU system has coherent radiation detection and a receiver probe that can be moved by a dual axis scanner to take measurements over a large area. Therefore both power and phase can be measured over a large area enabling verification of the optical performance of the lens.

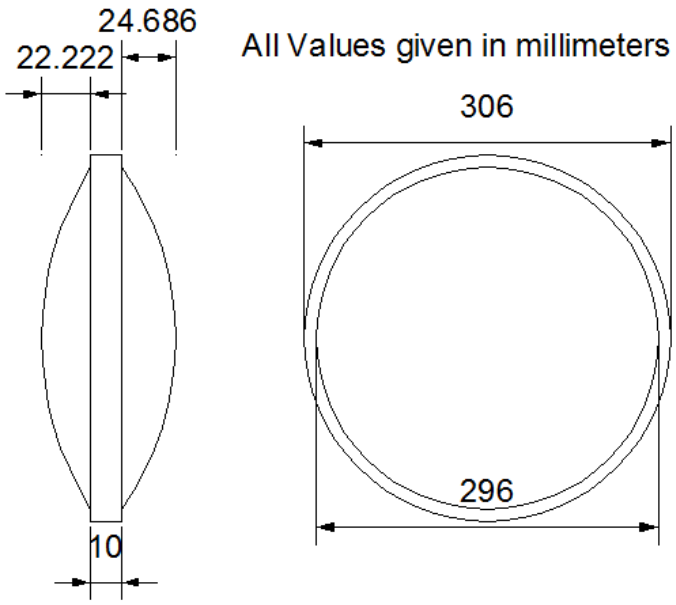


Figure 20: M type lens mechanical drawing. (Not to scale)

Table 4 provides the values used in the design of the M type lens for manufacture. These are based on the value of refractive index obtained from the test batch material.

Table 4: Table of M type lens parameters used for lens manufacture.

| Quantity | Value | Unit |
|---|---|---|
| Radius of curvature (R1) surface 1 (S1) | 397.735 | [mm] |
| Radius of curvature (R2) surface 2 (S2) | -418.344 | [mm] |
| Conical constant (k1) (S1) | -2.333256 | |
| Conical constant (k2) (S2) | -4.758720 | |
| Focal distance (F) | 377 | [mm] |
| Semi diameter | 143 | [mm] |
| Overall lens thickness at centre (t) | 56.985 | [mm] |

The profile of the lens surface was assessed like the C type lens. Table 5 below shows the measured values for the radius of curvature, conical constant and thickness for each side of the three prototype M type lenses that were manufactured.

Table 5: Table of M type lens parameters from each of the three lenses after manufacture.

| Lens | S1, R (mm) | S1, C | S1, T (mm) |
|---|---|---|---|
| M1 | 400.485±.415 | -2.141±.002 | 24.663±.022 |
| M2 | 397.852±.100 | -2.388±.020 | 24.653±.026 |
| M3 | 397.455±.601 | -2.400±.031 | 24.674±.055 |
| | S2, R (mm) | S2, C | S2, T (mm) |
| M1 | 425.793±1.175 | -4.885±.033 | 21.880±.037 |
| M2 | 421.721±.330 | -4.839±.011 | 22.083±.022 |
| M3 | 422.760±1.520 | -4.862±.015 | 22.017±.071 |

The thickness deviations across the surface of each lens were measured for both sides, across two axes perpendicular to each other across the centre. One side was the top and the other the bottom side due to the orientation during the manufacturing process. Figure 21 below show the combined deviation from the expected profile of each side of the M type lenses and Figure 22 shows the deviation for the C type lenses.

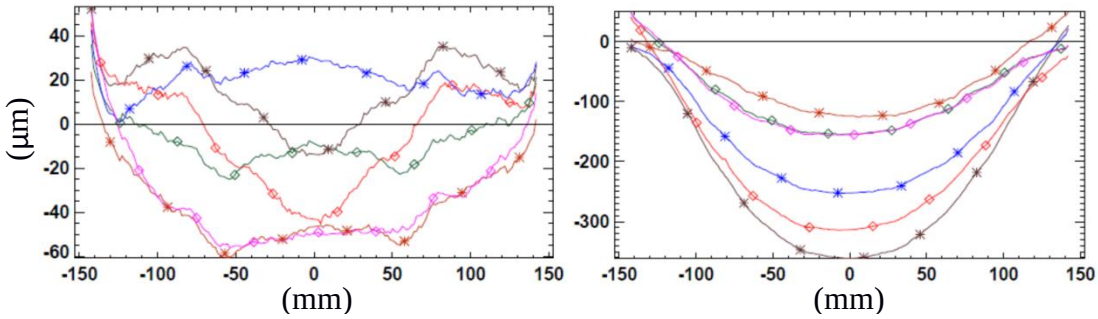


Figure 21: On the left are the deviations for the M type lenses in micro meters from the expected values for the bottom side of the lenses. The *y* axis shows the deviation values and the *x* axis is the position across the surface of the lens. On the right deviations for the top side of the M type lenses.

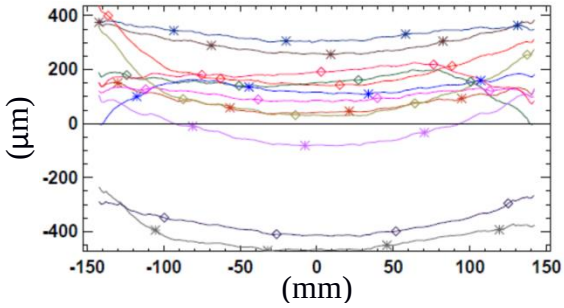


Figure 22: Deviations in surface position for both the top and bottom surfaces of the three C type lenses. *Y* axis denotes the deviation in micro meters and the *x* axis shows the position across the surface of the lenses.

From these measurements the minimum, maximum, root mean squared, median and root mean squared median values were determined for each lens. This shows variation in the manufacturing process between each lens but the maximum variation remains small with largest on the M1 lens at 571 µm.

Table 6: Errors in position across the surface of the lenses.

| Lens | $\Delta_{max}$ (µm) | $\Delta_{min}$ (µm) | $\Delta_{rms}$ (µm) | $\Delta_{med}$ (µm) | $\Delta_{medrms}$ (µm) |
|---|---|---|---|---|---|
| C1 | 521.2 | 293.7 | 376.6 | 352.1 | 71.1 |
| C2 | 344.6 | 172.8 | 280.5 | 284.4 | 55.2 |
| C3 | 443.2 | 221.7 | 310.0 | 288.1 | 69.8 |
| M1 | 363.9 | 2.0 | 241.2 | 229.0 | 130.9 |
| M2 | 171.9 | 2.0 | 119.4 | 119.9 | 71.4 |
| M3 | 217.1 | 1.0 | 153.1 | 156.5 | 84.1 |

# Chapter 3: Measurement System

## 3.1 Introduction

This chapter contains a full description of the measurement system used to characterise the performance of the prototype lenses in Maynooth University (MU). This will include all components used in order to mount and align components. All the software utilised in order to complete the measurements will also be presented. This includes custom programs written to automate the measurement process. The operating principle of the Vector Network Analyser (VNA) that is used to produce the input stimulus and detect the resultant response will be given, along with the calibration procedure that is specific to it for the system. The chapter concludes with a detailed description of the system alignment procedure, which is key for ensuring high quality experimental data, both in terms of the captured VNA data and the knowledge of residual offsets in the system.

## 3.2 Measurement System

In a basic measurement system there is an emitter to produce the testing signal and a receiver in order to measure the signal after passing through the system. The device under test (DUT) is an object inserted between the emitter and receiver that impacts the test signal. The receiver is used to capture and characterise the reflected/transmitted radiation from the system.

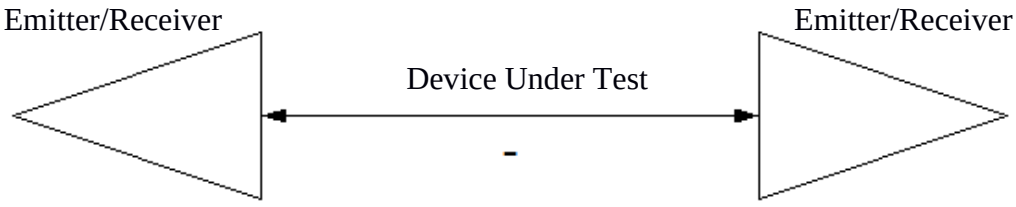


Figure 23: Schematic of basic testing system.

### 3.2.1 Vector Network Analyser (VNA)

The emitter and receiver used in the testing system are controlled by a computerised controller that generates the testing input stimulus and analyses the response from the system. This device is a Rhode and Schwarz ZVA-24 Vector

Network Analyser (VNA). A VNA allows both the magnitude and the phase of a signal to be measured by comparing the emitted and received signals. The system is a four port system used as a two port in order to emit and receive a signal on separate ports. The VNA used in the laboratory operates in the frequency range from 10 MHz to 24 GHz. A higher frequency range is required for the testing system. To achieve this, the operating range of the VNA is extended into the W-band of the electromagnetic spectrum (75-110 GHz) through the use of specialized Rhode and Schwarz coherent frequency converter heads (type ZVA-ZV110).

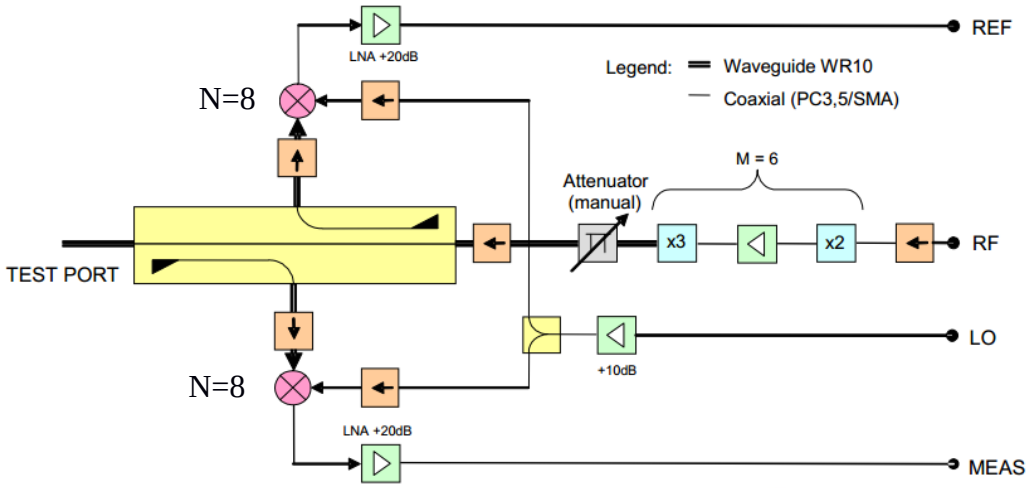


Figure 24: Internal electronics configuration for the VNA converter head.

In order to use the converter heads four connections are required from the VNA. Two inputs with a local oscillator (LO) signal in and a radio frequency (RF) input signal. The RF signal is the source signal to be emitted by the converter head. The RF signal is put through a multiplier network to increase the frequency to six times the original value. There are two outputs from the head back to the VNA, a reference out (REF) and a measurement out (MEAS). The LO input is used in the head in order to reduce the frequency of the measured signal and reference signals down to a lower frequency in order to be analysed by the VNA. These provide the VNA with a reference signal and the measured signal to compare to each other. To ensure an accurate result the system must nonetheless be calibrated before measurements can be made. By performing a calibration before measurement the expected magnitude to receive from the signal, for a specific frequency, is known, thus the VNA can accurately measure the loss in signal through the system. This means the magnitude that is measured is a comparison between the expected maximum and received signals.

The phase change can also be measured so the point in the phase cycle can be determined. The calibration also allows the system to measure the magnitude and phase received through reflection by the head that emitted the signal. These ports can act as either emitters or receivers. As a result the magnitude and phase can be measured in transmission and reflection.

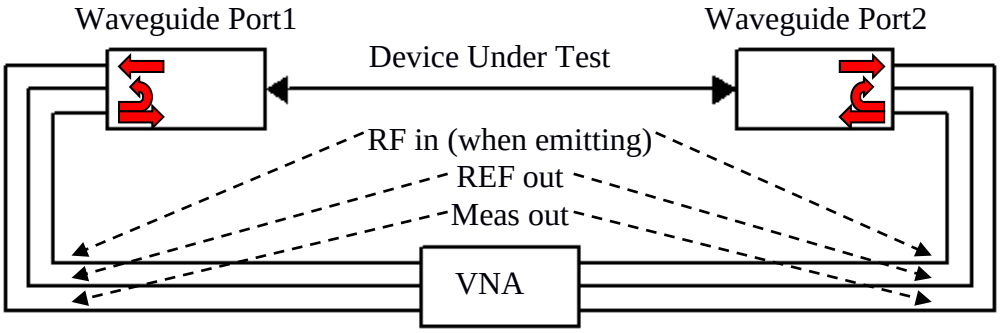


Figure 25: Schematic of the emitter and receiver connected to the Vector Network Analyser (VNA).

### 3.2.2 Feed horn

In order to inject the stimulus signal into a free space setup an antenna is needed. A basic antenna is simply a metal rod through which an alternating current at the frequency of the required radiation is applied. A more technical arrangement is required in order to have a collimated test signal rather than an omnidirectional signal. For this purpose the emitter uses a horn to create a well collimated beam across the operational frequency band. The feed horn is a corrugated horn optimised for 94 GHz manufactured by Thomas Keating Ltd., fed from the WR-10 waveguide port of one of the frequency converted heads of the VNA (port 2). The WR-10 waveguide is a rectangular aperture, 2.54 by 1.27 mm, which allows only the fundamental mode $TE_{10}$ to propagate for the frequency range.

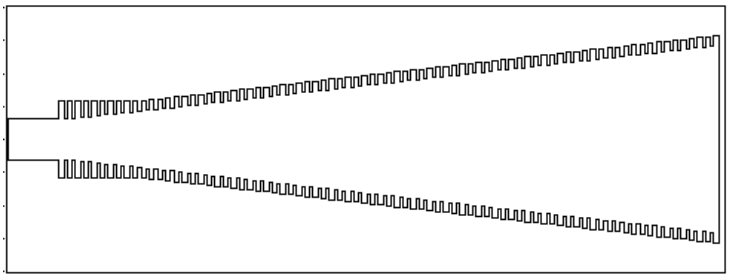

Figure 26: Cross section of the horn profile for the corrugated horn.

The operation of the horn across all of W band (75-110 GHz) is single-moded. The on-axis polarization of the horn beam in the far field is in the *y* direction (electric field).

The design geometry of the horn was used in the subsequent analysis through a mode-matched model of the performance of the corrugated structure of the horn.

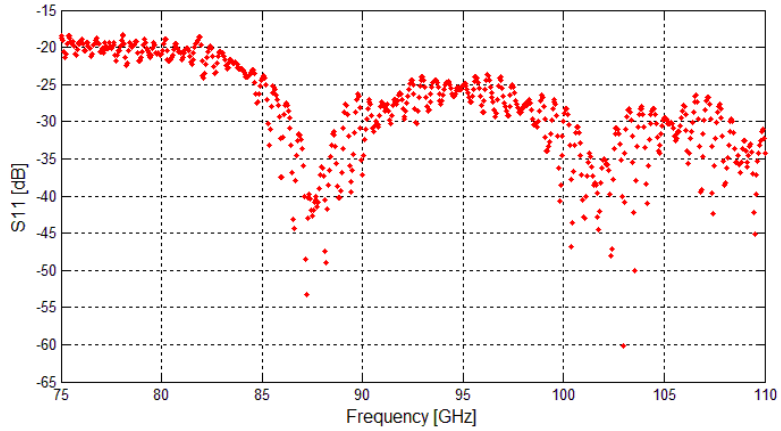


Figure 27: Plot of the S11 power received by the horn through internal reflection. Shows good overall performance of the horn, particularly at higher frequencies.

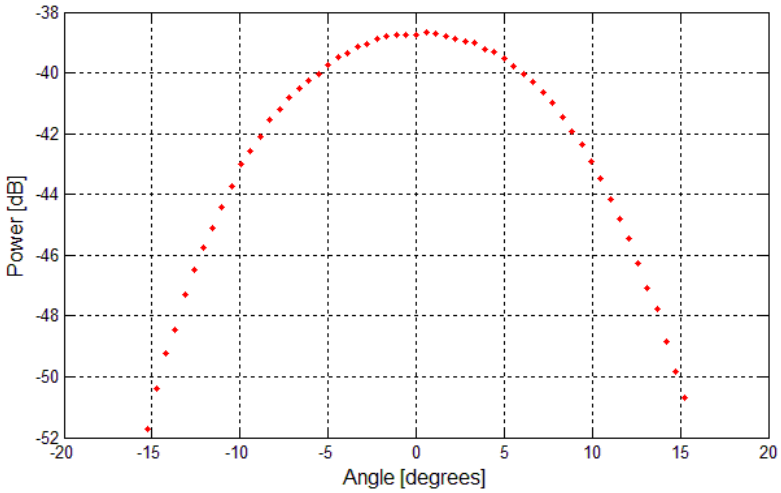


Figure 28: Far field power for the Thomas Keating feed horn.

### 3.2.3 Receiver probe

To couple the stimulus signal at the receiver a truncated WR-10 waveguide with 1 mm wall thickness was used as a receiver probe. The length of the probe including the standard WR-10 flange was 12.5 mm. This was long enough, in combination with the 40.0 mm length of the WR-10 test port adaptor between the probe and the reflectometer of the VNA, to ensure that only the fundamental $TE_{10}$ mode contributed to the detected signal at the frequencies that were used. When the receiver probe aperture is aligned with the feed horn waveguide aperture the measurement is known as co-polar. That is the measurement to obtain maximum coupling between the emitter and receiver.

A small patch of radio frequency (RF) absorbing material (approximately 5 cm by 5 cm) was mounted directly on the probe, flush with its front face. This helped to suppress most of the reflection from the flange of the probe and prevent standing waves in the system.

Picture 3: The photo on the left is the receiver probe attached to the waveguide feed. The photo on the right is the absorber that is mounted to the front of the probe.

Both the receiver probe and the emitter horn are input into the system after calibration and therefore have to be included as devices under test in the computational simulations to account for their effect on the system.

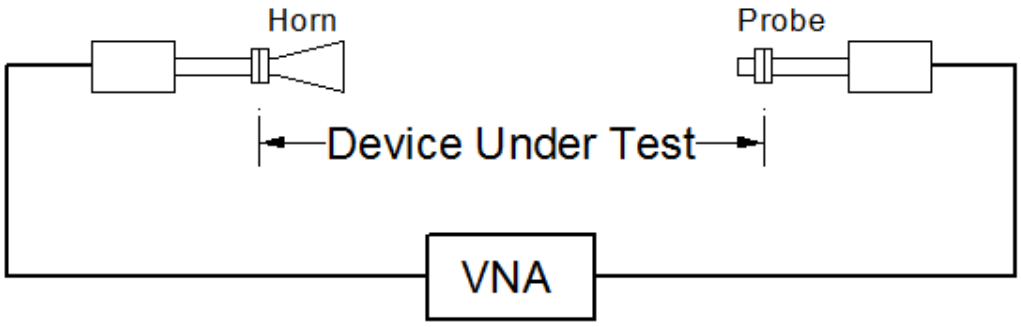


Figure 29: Schematic with the horn attached to the emitter port and the receiver probe attached to the receiver port. Both now become part of the system under test and must be included in subsequent simulations of the system.

For cross polar measurements a twist is attached to the receiver head. This turns the receiver probe at 90 degrees to the feed horn waveguide and should result in the opposite effect to the co-polar measurement which is to say no coupling between the emitter and receiver. Separate calibration is performed for the cross-polar measurement. The 32 mm length twist is attached to the receiver head before the calibration is performed. This means the twist is included in the calibration and thus does not need to be taken into account during the simulation.

Picture 4: Photo of the twist which is used during cross polar measurements placed between the waveguide feed and the receiver probe.

### 3.2.4 Device under test

The purpose of the system that has been described is to enable accurate characterisation of the components placed between the emitter and receiver, as the devices under test (DUT). In our setup the main DUT is the lens but as was stated previously the emitter horn and receiver probe have to be included as part of the DUT in any subsequent simulations. Adjustment of the angle of the lens with respect to the phase front of the injected stimulus signal is required. The device must therefore be mounted on a rotation stage to allow rotation of the lens. This enables the alignment of the angle of the lens to the phase front of the incident beam and is also used during measurement to enable measurement of the lens with differing incident angles of incidence with respect to the surface normal of the lens. In order to ensure proper alignment of the lens with the system it must also be mounted in such a way as to allow the vertical height of the lens and lateral position to be adjusted, relative to the emitter horn which has a fixed height and lateral position on the translation stage.

### 3.2.5 Lens mounting

During the measurements the lenses were mounted on a custom semi-circular aluminium holder 10 mm in thickness, designed specifically for the lenses. The lenses were fixed to it using regularly spaced small bolts in the bottom part of the flat lip of lenses. The front face of the lens holder facing the feed horn was covered with absorbing material to suppress specular reflection of the illuminating beam, see Picture 5.

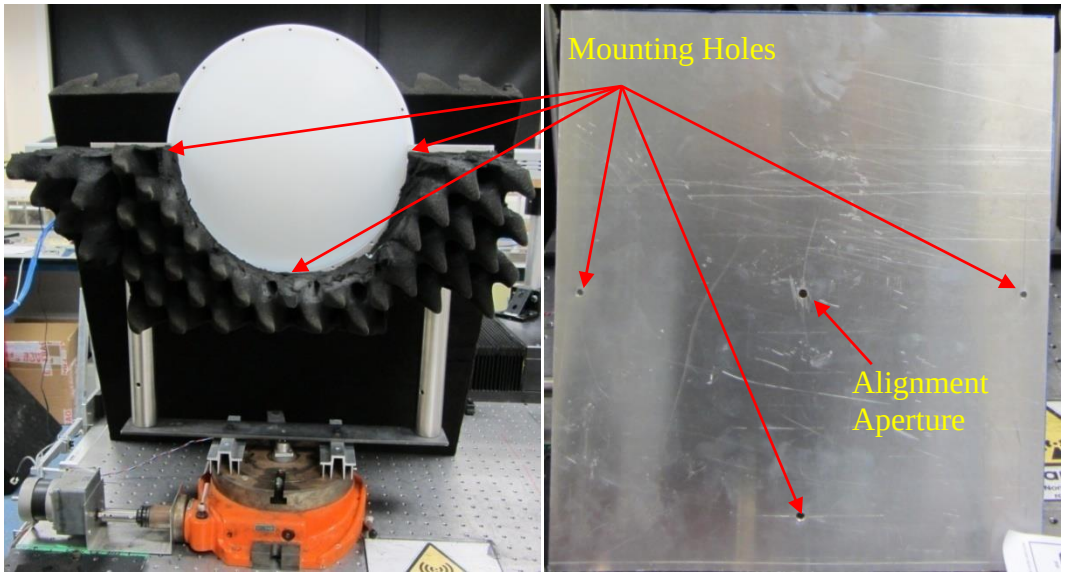


Picture 5: On the left is the rotation stage with the lens mounted on its holder. The holder is held on the two steel bars that are attached to an iron bar fixed to the rotation stage. On the right is the aluminium aperture sheet used for alignment of the rotation stage.

This custom holder was mounted on two vertical 1 1/2 inch posts fixed to a custom heavy duty rotary stage. The rotation axis was offset with respect to the centre of the lens to keep the centre of mass of the lens plus support assembly close to the rotation axis. The lens support allowed manual adjustment of the vertical position of the lens with respect to the base of the rotary stage (along the posts) and limited lateral displacement of the aluminium holder with respect to the posts. The angular position of the rotary stage was computer controlled. During alignment of the rotation stage the lens is replaced with an aluminium sheet with a small on-axis aperture, shown on the right in Picture 5.

### 3.2.6 Custom programs

Several programs were used and written in order to control the measurement system and analyse the results. The software package used to write the measurement control program for the MU measurement system is called LabVIEW. LabVIEW is a graphical programming environment focusing on control of machines for industrial use. The software can be used to perform general programming with all the normal built in functionality such as for and while loops but also includes inbuilt programmes called subVI's specifically designed to control exterior motion controllers.

For the measurement system a program was written in order to operate the motion axes through a motion controller. The 4-axis National Instruments NI PCI-7334 motion

controller is a central communication point in order to issue commands and receive responses between the computer and motors which control the motion stages. The motion controller is operated through the Ghost 2 program. This allows control of a four axis system and measurement through communication with the VNA. This allows for automated measurements with the VNA over a number of frequencies. The range and step size for each axis can be specified independently. The bandwidth and calibration file used by the VNA is specified by the user to enable easy change from co-polar to cross-polar measurements. The tests to be performed on the DUT during the scan are also chosen. At the end of the measurement the results are saved to a measurement file for later analysis.

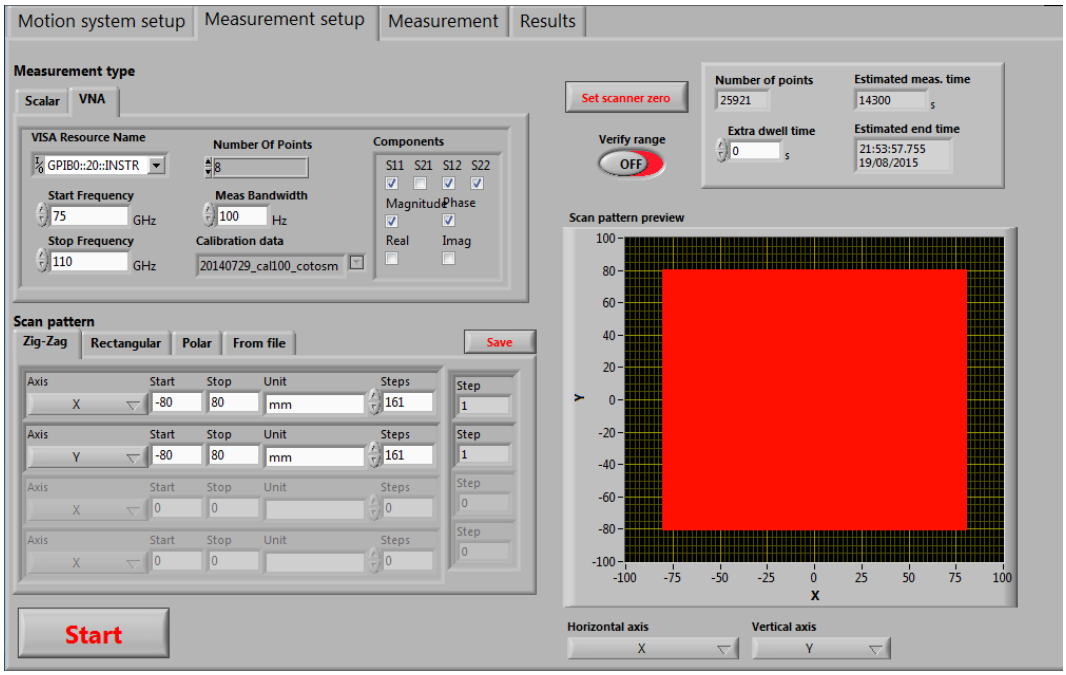


Figure 30: This is the main setup view for measurements in the Ghost 2 program. A start and stop frequency are set along with a number of points to take between these two values for our range of frequencies. The measurement bandwidth is set and calibration file chosen. The S parameters for the measurement are selected. Finally the scan pattern, number of axes and the range and step size for each axis are set.

The axes of the controller were assigned as follows:

- axes 1 and 2: transverse displacement of the receiver probe in the XY plane perpendicular to the optical axis of the system (linear 2D scanner with a full range in excess of +- 150 mm in both directions; )
- axis 3: on-axis displacement of the horn feed with respect of the rest of the optical system (lens and receiver). This is facilitated through mounting of

head 2 on a linear translational stage (Picture 6), with its axis aligned with the direction of the horn beam (*z* displacement of the horn; Figure 32).

- axis 4: rotation of the lens (Picture 5; shown not in-situ)

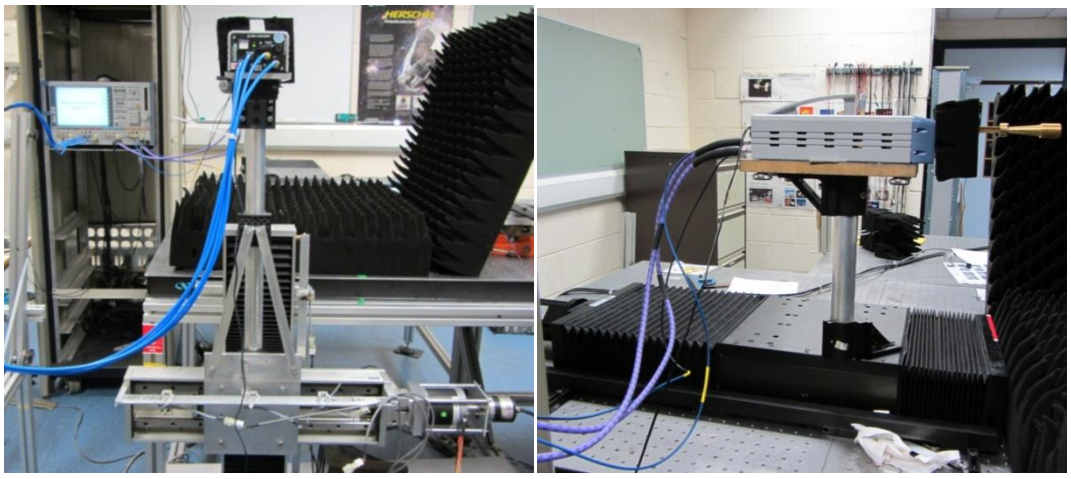

Picture 6: The picture on the left shows the 2D scanner for movement of the receiver probe along the *x* and *y* axes. The picture on the right shows the *z* translational table for movement of the feed horn.

### 3.2.7 Motion control system

During measurements the receiver head of the Vector Network Analyser (VNA) is scanned over the XY plane and/or in a zigzag pattern, with the *X* axis being the minor axis (fastest changing). The axis priority, from fastest to slowest changing, was *X*, *Y*, *Z* (horn displacement), $\alpha$ (lens rotation). The VNA measurements are taken with a stationary head (not on-the-fly) and are electronically synchronized with the motion control system. The speed of the *X* motion and the rigidity of the head mount were such that no extra delay was needed before the measurement, to avoid systematic head lag effects. The effective range in the XY plane with respect to the axis of the system was ±150 mm, in 5 mm steps, in the *Y* axis, and ±140 mm, in 5 mm steps, in the *X* axis.

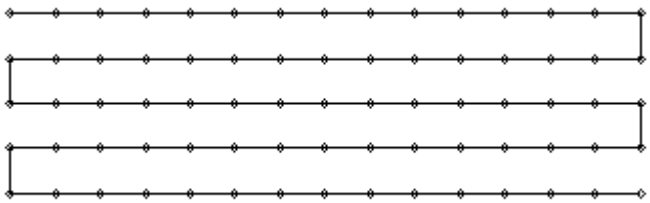

Figure 31: Shows the zigzag pattern of movement for the scan plane. The head travels along the x-axis before stepping down to the next level of the y-axis and scanning back along the x-axis.

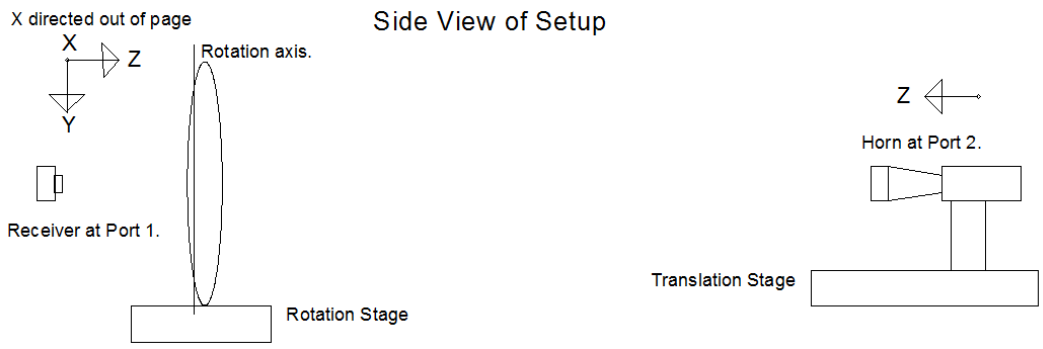


Figure 32: Side view of system setup.

### 3.2.8 Measurement parameters

Depending on the measurements being performed, different S parameters were measured. S parameters are the list of measurements that can be made depending on the port taken to be the emitter and the port taken to be the receiver. Below is the summary of the overall interpretation of all measurable S parameters.

- $S_{22}$ represents the reflection measured at the input of feed horn (waveguide port 2).
- $S_{12}$ is the transmission from the feed horn input (waveguide port 2) to the waveguide probe output (waveguide port 1). 0 dB would represent perfect coupling between the two ports.
- $S_{21}$ is the transmission from the waveguide probe input when used as a transmitter (waveguide port 1) to the waveguide output of feed horn used as a receiver antenna (waveguide port 2). 0 dB would represent perfect and complete coupling.
- $S_{11}$ represents the reflection measured at the waveguide probe (waveguide port 1).

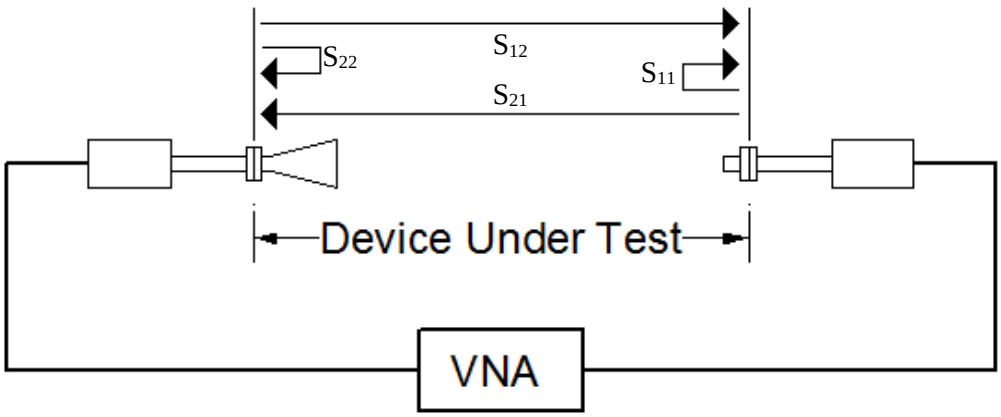


Figure 33: Diagram of the S parameters of the measurement system.

The parameter that is of most interest during measurements is the $S_{12}$ as this is the transmission from the feed horn to the receiver probe.

### 3.2.9 Calibration

The first step in setting up the measurement system is to turn on the VNA and the two connected heads. These are turned on and left for three hours to ensure that the system is stable. The system is then calibrated explicitly for each frequency from 75-110 GHz in 100 MHz steps, the standard frequency range and step size used for calibration. During subsequent measurements only 8 of these frequencies were used, from 75-110 GHz in steps of 5 GHz.


Picture 7: Picture of calibration kit equipment. From left to right there is the offset, match and short shown in the picture.

The system is calibrated through the standard two port TOSM (Through, Offset, Short, Match) calibration procedure using a commercial WR-10 calibration kit. This calibration is done and stored separately for the two polarisations, co-polar and cross-polar, to account for the twist that is introduced for the orthogonal polarization scan. In

each case the VNA and the heads are calibrated to include the waveguide port adaptors and the twist (if present). The through measurement compares the emitted signal from one head to the signal received by the other head. For the orthogonal measurements a 90° twist is added to the front of the receiver. This results in the rectangular WR-10 aperture of the receiver head being offset compared to the emitting horn head WR-10 aperture. In order to match these rectangular apertures for the through measurement, the receiver head is rotated 90°.

The short measurement compares the signal emitted from one head to that reflected back to itself with the short attached. The receiver probe and the horn are not included in the system calibration and become part of the measured device under test (DUT).

For port 1, which controls the receiver head, a higher RF and LO signal power level than usual (+3 dB) is applied due to longer cables being used, which have higher attenuation compared to the short cables used at port 2 for the transmission head. This improves the stability of the calibration above 100 GHz.

VNA receiver bandwidth of 100 Hz is used for normal (co-polar) measurements and the calibration is done at the same bandwidth. The calibration and the measurements for the orthogonal polarization (cross-polar) are done with a narrower bandwidth of 10 Hz, which lowers the noise floor but increases the measurement time.

## 3.3 Alignment

The alignment and calibration procedure that was employed for these measurements aims to either minimize or establish the various offsets and tilts with respect of the axis of the free space beam from the horn. The absolute alignment of all components was not attempted here, because of the nature of the system that was being investigated. The phrase “geometrically aligned” below means that reasonable effort was put into ensuring that the residual tilts or offset were small. Each step in the alignment process will be covered in detail below. The system is aligned for the single frequency of 100 GHz.

### 3.3.1 Initial alignment

The mounting table, on which the translation stage and lens are placed, was levelled in order to give a reference surface. The scanner, on which the receiver probe is mounted, is attached to the side of this table. The scanner is levelled to match the

mounting table surface. This creates a good alignment between the system components and the scanner and allows for future finite adjustment at a later stage. The converter head, which is attached to port 1 of the VNA, is mounted on the scanner. It is then geometrically aligned to right angles with respect to the scan plane of the scanner. The receiver probe is attached to the WR-10 waveguide.

The translation stage is fixed in place and geometrically aligned with the edge of the table. The head attached to port 2 on the VNA is mounted on top of the translation stage. The emitter horn is attached to the WR-10 waveguide. It is then geometrically aligned with the translation stage.

The system offsets remaining after initial alignment are corrected using sequences of measurements of the Thomas Keating feed horn. The horn produces a nearly fundamental Gaussian beam with which we can utilise its properties to align the system as will be explained in the following sections.

### 3.3.2 Gaussian beam mode theory

The majority of work in optics, with wavelengths close to the visible part of the spectrum, use geometric optics. This is the use of ray tracing from one point to another to find the path of each ray from each source. Diffraction is the spreading of a beam of light as it travels from one point to another. Diffraction is dependent on the size of the wavelength of the radiation and thus becomes more dominant for longer wavelengths that have proportions closer to the size of the optical system they are propagating through. For this purpose we think of the propagation of a beam.

This beam describes the distribution of power with a maximum at the centre and the power falling off away from the beam centre. A Gaussian shape is used to describe this power distribution. This mathematical description for the distribution of radiation in the measurement systems correlates well with the feed horn beam pattern and describes the diffraction of the radiation as it travels through the system.

The basic system for measurement purposes consists of a source and receiver for the radiation. Gaussian beam propagation considers the source to be a finite area rather than a point source as for geometrical optics. In this system a fundamental Gaussian beam would describe the propagation of the radiation with sufficient accuracy. The beam travels in a defined direction but does not have the infinite extent that a plane wave would. The effective extent is finite and varies during the propagation of the

wave. We can derive a paraxial wave equation for the propagation of the Gaussian beam using the Helmholtz equation.

$$(\Delta^2 + k^2)\varphi = 0$$

We now take the electric field equation and reduce it to a time independent form:

$$E(x, y, z) = u(x, y, z)e^{-ikz}$$

Substituting this into the Cartesian coordinate form of the Helmholtz equation gives:

$$\frac{\partial^2 u}{\partial x^2} + \frac{\partial^2 u}{\partial y^2} + \frac{\partial^2 u}{\partial z^2} - 2jk\frac{\partial u}{\partial z} = 0$$

If we assume variation of the amplitude *u* is small along the direction of propagation and the axial variation is small compared to the variation perpendicular to the direction of propagation then the third term in the equation can be removed and we are left with the paraxial wave equation. (Goldsmith 1998)

$$\frac{\partial^2 u}{\partial x^2} + \frac{\partial^2 u}{\partial y^2} - 2jk\frac{\partial u}{\partial z} = 0$$

This form of the paraxial wave equation can be solved with a set of solutions called the Hermite-Gaussian modes. These describe the shape of the beam distribution. The primary solution is the standard Gaussian beam profile. There are a set of common properties of the beam which are useful in its description. The $W_0$ parameter is the beam waist at the focus point. The beam waist is equal to the radius of the beam where the power has fallen to $1/e^2$ of the on axis value. The *z* value is the distance travelled from the focus position. *R* is the radius of curvature of the phase front of the beam which is dependent on the distance the beam has travelled. The *W* value is the waist at a point a distance *z* from the focus. (Goldsmith 1998)

If the system is not a pure Gaussian system or there are distortion effects present then higher order modes are required to accurately describe the system. For Hermite-Gaussian modes these take the form of axially symmetric distortions. These are distortions in the *x* or *y* axis of the beam perpendicular to the direction of propagation. These solutions are therefore useful in systems with symmetric axial distortion effects.

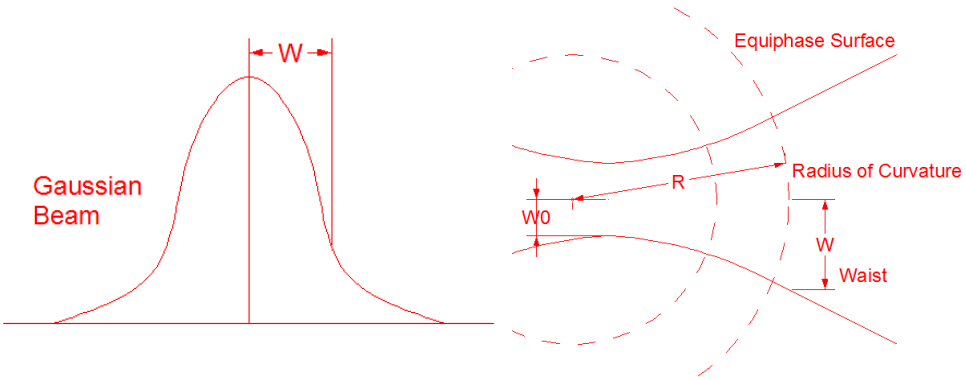


Figure 34: On the right is a cut through a fundamental Gaussian beam. The left is an image describing some of the key properties of a Gaussian beam.

The paraxial wave equation can also be solved in cylindrical coordinates. In this case an alternative set of base solutions to the equation can be derived. These sets of solutions are called the Laguerre-Gaussian modes. The first order mode solution is still the standard Gaussian beam profile but for higher modes the distortions are radially symmetric about the direction of propagation. (Goldsmith 1998).

### 3.3.3 Gaussian Fitter program

In order to assist in the alignment of the system a LabVIEW program called the 'Gaussian Fitter' was written by Dr. Marcin Gradziel to fit a fundamental Gaussian to measurements of the Thomas Keating feed horn. This allows alignment of the system when using the Thomas-Keating feed horn, due to the horn producing a nearly fundamental Gaussian beam. The program fits the best Gaussian to our data measured for the beam from the horn and the parameters for the centre of the beam and the angular offsets of the beam to the detection plane can be adjusted for in the measurement system. The measurement can then be repeated and results analysed until these offsets are minimised. These alignment steps will be described in detail in the section 3.3.5.

The program analyses the input measurement data and makes an initial guess as to the best-fit Gaussian parameters. These parameters include $W$ the waist of the beam at the detection plane, $R$ the radius of curvature of the phase front of the beam, $W_0$ the waist at the focus of the beam and $Z$ the distance from the $W_0$ position to the detection plane. For alignment the parameters of interest are, the $x$ centre, $y$ centre, $\alpha$ and $\beta$. $x$ centre and $y$ centre correspond to the coordinates of the centre of the fitted Gaussian beam. Angle $\alpha$ is the angle of rotation of the beam about the $x$-axis, where $\alpha$ is positive

when rotating clockwise around the positive end of the axis. Angle $\beta$ is the rotation of the beam at the scan plane about the $y$-axis, where $\beta$ is positive for clockwise rotation about the positive end of the axis.

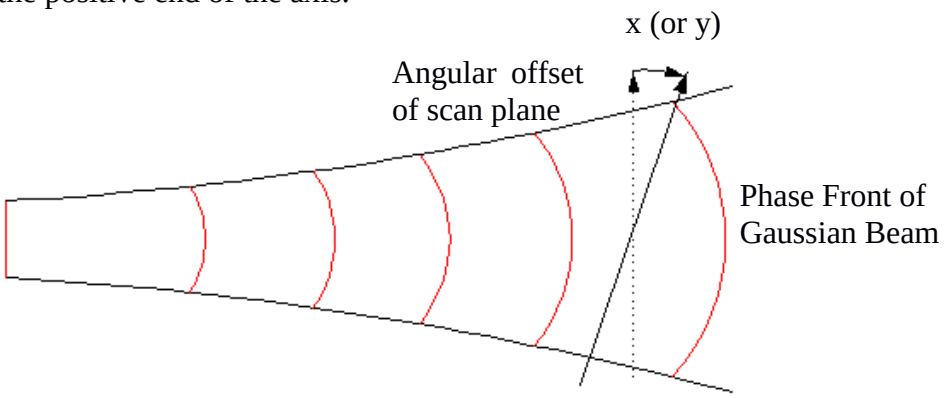


Figure 35: Schematic of beam with measurement plane rotated with respect to the incoming beam. This angular offset will result in a positive change in angle with the positive and negative ends of the axis orientated as shown in the diagram for either the $x$ or $y$ axis, corresponding to the $\beta$ or $\alpha$ angle respectively.

After the initial guess is made the program varies the parameters to obtain the best fit and reduce the residuals between the measured data and the fitted fundamental Gaussian. The program adjusts for the angular offsets by changing the angle of the fitted cut plane through the fundamental Gaussian. The program aims to minimise the phase residuals and obtain the most symmetric phase residuals possible.

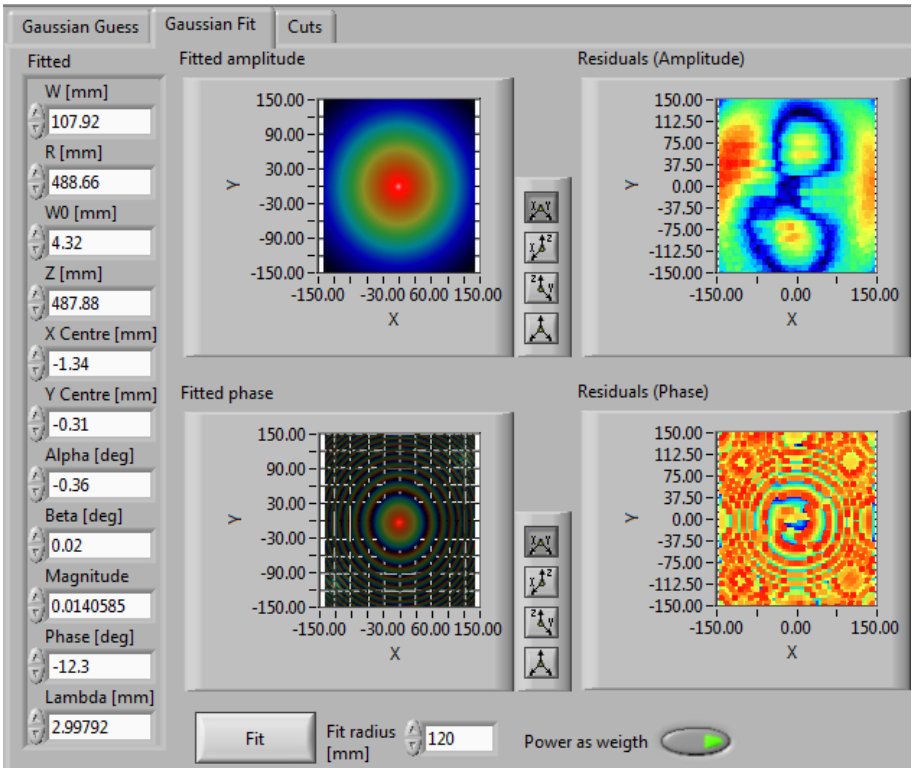


Figure 36: Front panel image of the Gaussian Fitter program.

### 3.3.4 Feed pattern analysis, translation stage and horn alignment

After the components are mounted, further alignment is performed to align the translation stage to the scanner plane and the horn to the translation stage. This is done using a sequence of measurements of the beam from the emitter horn for different distances from the horn to the scan plane. The measurements are performed using the Ghost 2 program. The results from each measurement are analysed using the Gaussian fitter program discussed in section 3.3.3. The results from the Gaussian fit (values of $x$ centre, $y$ centre, $\alpha$ and $\beta$) are then used to determine the offsets in the system.

The two offsets to be adjusted for are the orientations of the horn relative to the motion axis of the translation stage and of the translation stage axis relative to the scan plane. The horn must be aligned with the translation stage before the translation stage can be aligned with the scan plane. If the horn is not aligned with the translation stage axis there will be a drift in the centre position of the Gaussian beam on the translation stage. This means the beam centre $x$ and $y$ position will drift across the scan plane as the horn is moved towards or away from the scan plane. This drift distance can be used along with the distance the translation stage has moved in order to determine the angle between the emitter horn and the translation stage axis. A measured correction to the horn orientation can then be performed to reduce this angle.

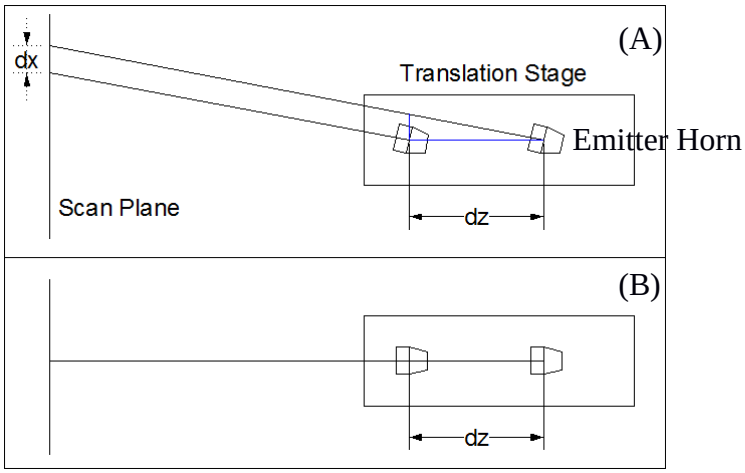


Figure 37: (A) If the horn is not parallel with the axis of motion of the z-axis (on the linear translation stage), the centre position of the Gaussian will drift across the scanning plane for changes in horn position, dz. (B) If the horn is aligned parallel to the axis of motion of the linear translation stage, there will be no drift across the scanning plane.

A series of measurements of the beam are made with the horn at three different distances from the scanning plane. The Gaussian fitter program then fits the 100 GHz frequency component of the beam measurement at each *z* position to obtain best fit values of *x*, *y* centre and $\alpha$, $\beta$ angles. These are used along with the known distance moved along the translation stage and the distance of drift in the *x* and *y* directions on the scan plane to calculate the angular correction needed to align the emitter horn. To correct for an offset in the *x*-axis the horn is rotated about the pillar on which it is mounted. To determine the amount by which the horn should be rotated the principle of equivalent triangles is used.

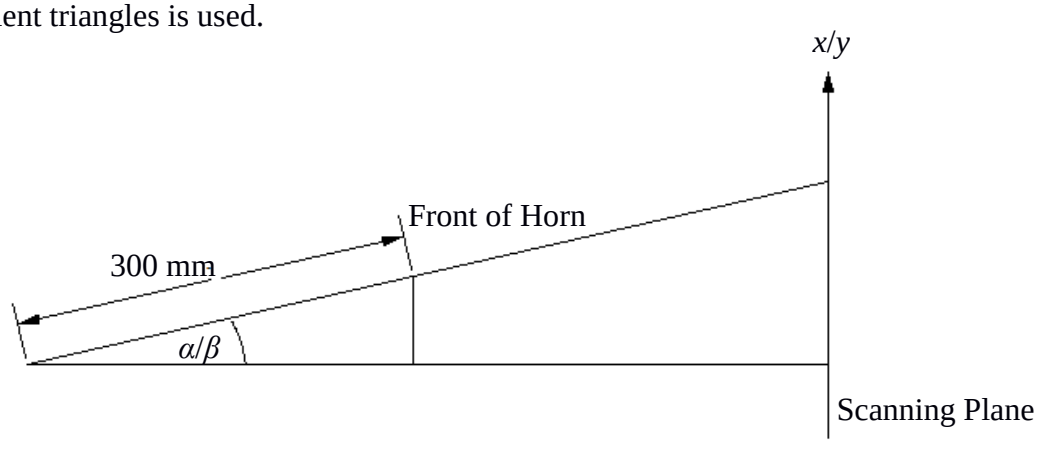


Figure 38: Schematic of equivalent triangles in system

A triangle with adjacent side equal to the distance from the front of the horn to the axis of rotation is used with the resulting distance on the opposite side the amount the front of the horn must be displaced to correct for the misalignment. The distance from

the front of the horn and the axis of rotation is 300 mm, this value is multiplied by the tan of $\beta$ angle calculated to find the distance for the horn to be moved. The *y*-axis offset was corrected by placing shims under the back or front of the head in order to tilt the head to correct for angle $\alpha$ provided by the program Gaussian Fitter.

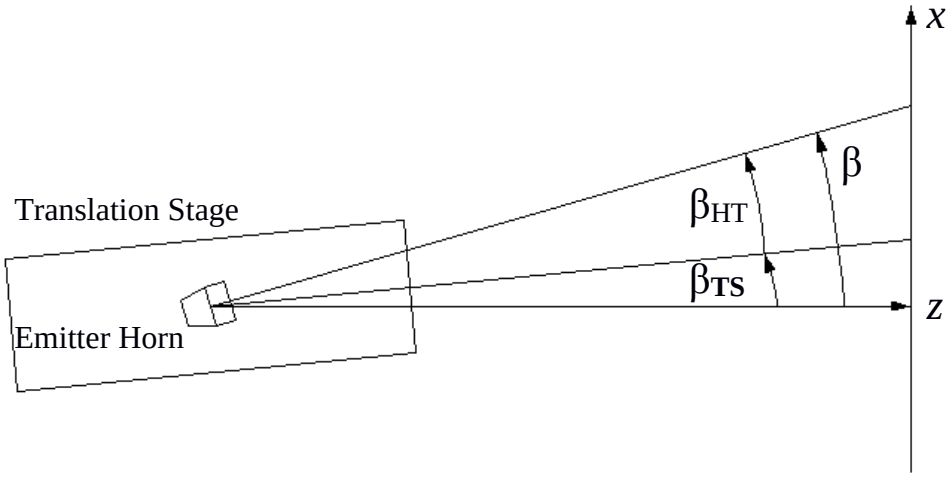


Figure 39: Overhead diagram showing the angular offsets in the measurement system. The angle $\beta$ is the total angular correction required. Angle $\beta_{HT}$ is the contribution from the horn offset to the axis of the translation stage. Angle $\beta_{TS}$ is the angular offset between the translation stage and the scan plane.

Table 7 provides angles of $\beta_{HT}$ and $\alpha_{HT}$, the angles of the horn with respect to the translation stage axis in both *x* and *y* axes. Angle $\beta_{HT}$ corresponds to a rotation about the *y*-axis and angle $\alpha_{HT}$ to rotation around the *x*-axis, which can be adjusted by placing shims underneath the head. The distances, x and y, by which the horn must be moved to align the head are shown in yellow. These are calculated by multiplying the 300 mm distance between the front of the horn to its axis of rotation by the tan of the angles $\beta_{HT}$ and $\alpha_{HT}$.

Table 7: Shows an example of the horn displacement calculation to align the horn to the translation stage and the translation stage to scan plane. If the horn is aligned to the translation stage there should be no change in position of the X and Y values for different positions on the translation stage. If the translation stage is also perfectly aligned to the scan plane angles $\alpha$ and $\beta$ should be zero.

| Z (mm) | $\alpha$ (deg) | $\beta$ (deg) | X (mm) | Y (mm) |
|---|---|---|---|---|
| 0 | 0.01 | -0.02 | 3.84 | 22.87 |
| -100 | 0.01 | -0.01 | 3.6 | 22.58 |
| -200 | 0.02 | -0.01 | 3.35 | 22.3 |

| | 20140721_Alignment1 | | | |
|---|---|---|---|---|
| $\beta_{HT}$ | 0.14 | | 300 mm | 0.74 mm |
| $\alpha_{HT}$ | 0.16 | | 300 mm | 0.86 mm |
| | | | | |
| $\beta_{TS}$ | -0.15 | | 600 mm | -1.6 mm |
| $\alpha_{TS}$ | -0.15 | | 600 mm | -1.6 mm |

The remaining angular offsets, $\beta_{TS}$ and $\alpha_{TS}$, are used to align the translation stage to the scan plane. The $\alpha$ angle for the *y*-axis offset could not be corrected for as there is no accurate method to raise the front or back of the stage. Earlier it was noted that both table and scanner were levelled which leads to this offset being minimal. The *x*-axis offset angle can be corrected for by rotating the translation stage around either the front or back corner to correct for the angular offset. The distance from the front to the back of the translation stage is 600 mm and this value is used to determine the amount to move the translation stage shown in blue in the table.

After the angular offsets have been corrected for the scan plane is centred with respect to the centre of the emitted beam. This is done in the Ghost 2 control program, which is a custom LabVIEW program written to control the motion axes of the system in order to automate the measurement process. The program allows the user to set the zero point for each axis. The user can change the *x* and *y* position to the position of the centre of the Gaussian beam and set this as the new centre, (0,0), position. With the centre of the beam aligned with the centre of the scan plane the lens holder can be aligned.

### 3.3.5 Rotation stage alignment

The lens is mounted in a custom mount that is designed to hold the lens in place using mounting holes in the rim of the lens. The holder is mounted on a rotation stage by the use of two steel poles and an iron bar. The holder needs to be centred with

respect to the emitted beam, which is set to the origin of the scan plane. A metal sheet with a circular aperture is used to represent where the centre of the lens will be placed during measurement. A scan of the beam through the aperture without the lens, is made to locate the centre of the aperture. The position of the holder is adjusted in the *x*, *y* and *z* axes to align the beam centre with the centre of the aperture.

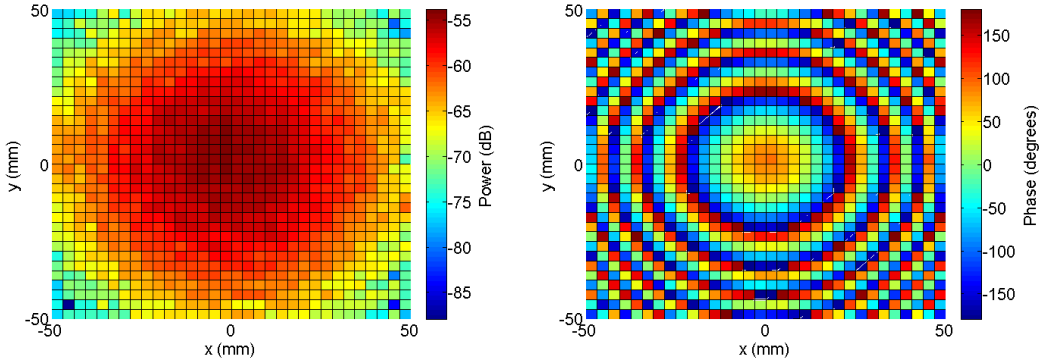


Figure 40: Result of a scan of the aperture plate after successful alignment of the centre of the plate with respect to the emitted beam at 100 GHz.

The lens mount needs to be aligned perpendicular with respect to the emitted beam, which is done using the metal sheet again. The sheet is mounted on the holder and the rotation stage turned through angles from -5° to 5° and the $S_{11}$ and $S_{22}$ parameters measured at each angle. The $S_{11}$ and $S_{22}$ parameters are the measurements of the receiver probe and feed horn respectively from the reflection off the metal sheet. The measured beam patterns of the $S_{11}$ and $S_{22}$ parameters should be symmetric about 0°.

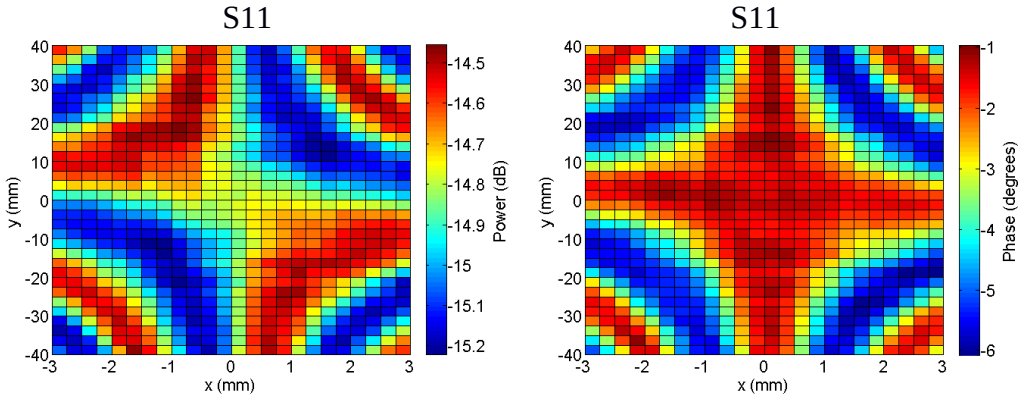


Figure 41: S11 data of an alignment scan after alignment of the rotation stage.

## 3.4 Determining System Offsets

After the system has been aligned the residual offsets in the system have to be determined. This is for inclusion in the computational simulations which require

accurate setup to match the measurement system and accurately model the system. The first offsets determined are for the horn with respect to the scan plane. To do this a scan of the horn is performed with the horn positioned at the translation stage location determined to give a flat phase at the scan plane when the lens is inserted. After the scan is performed the Gaussian fitter program is used to determine the $x$ and $y$ centre of the beam and the $\alpha$ and $\beta$ angles of the beam with respect to the scan plane.

### 3.4.1 Vision Assistant

LabVIEW includes an image analysis tool called Vision Assistant. That can be used to determine the position of objects within an image. This software is used to determine the distances and positions of objects in our system. A camera is set in a fixed position from the equipment to be measured. A calibration grid consisting of a 2D grid of regularly spaced dots is used for calibration. The calibration grid is inserted into the system where an object will be measured. A photograph is taken of the calibration grid to calibrate to the objects and to focus the camera at the distance of the object to be measured. The calibration grid is removed and the camera auto focus turned off so that it remains in focus when the object is included.

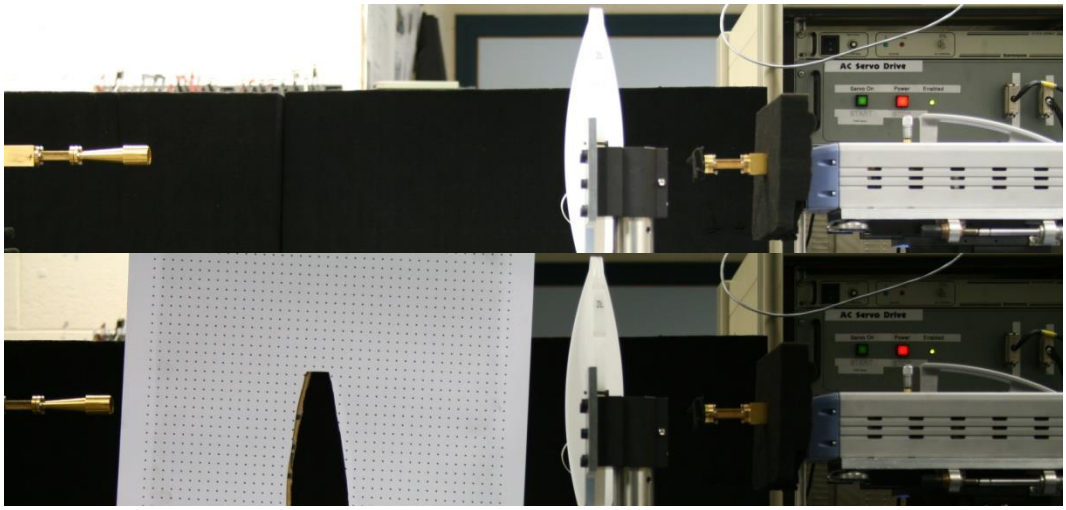


Figure 42: Image of the measurement setup. Top: The distance from the feed horn to the front of the lens needs to be measured. Bottom: A calibration grid is inserted between the horn and the lens in the plane of the point at the front of the horn and the centre of the lens.

The software analyses the calibration picture and, given the distances between the dots on the grid provided by the user, can determine the distances in the image. To identify the dots on the grid parameters in the program are changed for the contrast and saturation in the image so that the program can identify all the grid points and disregard

other artefacts such as dirt on the grid. The program then determines the location of each point on the dotted grid and calculates the distance between each dot. The program can correct for slight tilt in the image and calculate the error in positions given by the program. Once this calibration is complete the program can calculate absolute position and distances of all points in subsequent images even if the grid did not cover the area of these objects by extrapolating the grid over the entire image.

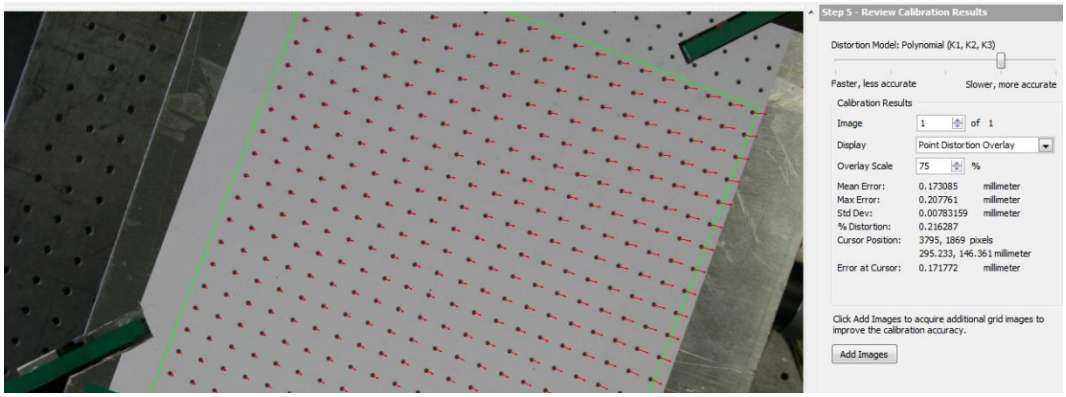


Figure 43: Vision Assistant program screenshot depicting the calibration image with red arrows to indicate the errors within the image at each point on the grid. The arrows are scaled up in order to display the errors which are small, with a mean error of 0.17 mm. The error increases for the points away from the reference centre for the grid.

### 3.4.2 Distances and offsets

Photographs are taken of the system from a side view. This allows the distance between the horn, lens and receiver to be measured.

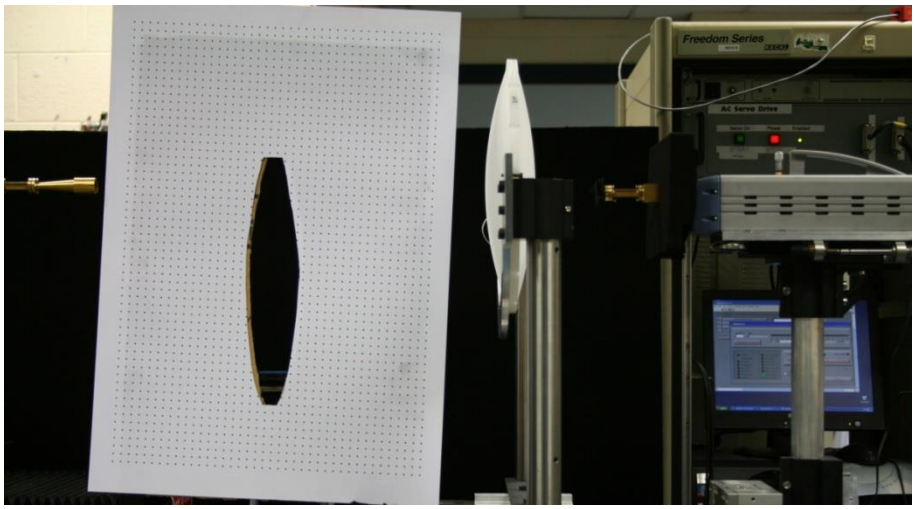


Picture 8: Photograph of the system with the calibration grid in place in order to measure the distance between the horn and the face of the lens.

Vision Assistant was also used to determine the offset of the axis of rotation of the rotation stage with respect to the centre of the lens. This was achieved by taking a series of pictures of the rotation stage from above with the rotation stage at different angles. A reference photo is taken first. The grid is then removed and the rotation stage rotated by 60° in 5° steps. In each photograph the four corners of the rectangular section on each side of the metal lens holder were included.

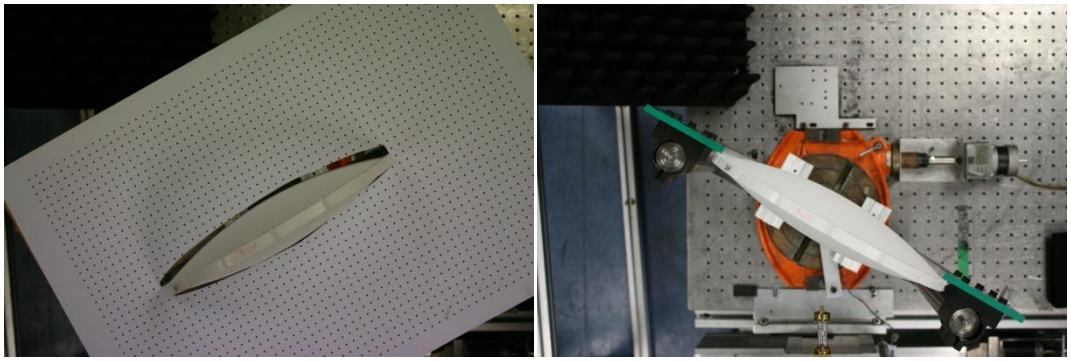

Picture 9: Rotation stage reference photograph and position measurement photo with and without the calibration grid. The reference photograph is used to calibrate object positions on the measurement photographs. The four corners of the two areas marked with the green tape are tracked over a sequence of images to find the rotation centre.

The image containing the reference grid was analysed using the Vision Assistant tool in LabVIEW. After this grid is used to calibrate the image, it is subsequently used when picking out points on the other images, which are set at different angles. 8 points were chosen at the four corners of the lens holder, shown in green in Picture 9. A LabVIEW program was written to analyse these points using the different angles to determine the rotation centre. This was then related to two points which depicted a line from one corner to the other of the lens holder.

Using all eight points and angles from 0 to 60 degrees in steps of 5 degrees it was possible to determine an offset from the edge of the holder on which the lens is mounted to the centre of the rotation point of 23 ± 1.2 mm. If the lens rim, which is taken to be 10 mm thick, is pressed against the holder edge, a distance of 18 ± 1.2 mm from the lens centre to the rotation point (on the feed horn side of the lens) centre is calculated.

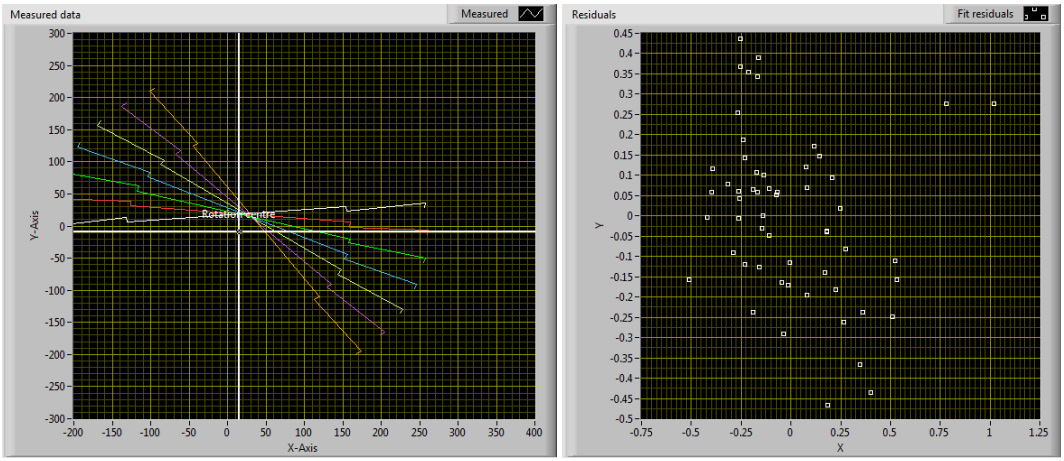


Figure 44: Screenshot of the front panel for the rotation analysis program. The rotation centre found by the program is superimposed on the image of the tracked points shown on the left. The right image shows the residuals left after the analysis is run for the location of the points.

# Chapter 4: Experimental Results

## 4.1 Introduction

This section describes the measurements made of each lens. The lenses were measured following a set of predetermined measurement parameters based on the requirements and limits of our testing system. The scans of the lens beam pattern were performed across a 2D plane using the scanner covering the entire area of the lens. The position of the emitter horn relative to the lens was varied to assess the performance away from the designed position. The lens was rotated on the rotation stage to analyse the performance of the lens with off axis input beams.

Before measurements were made of the M type lenses the distance from each lens where the phase front is constant was experimentally determined. The lenses were designed to have a flat phase front at a certain distance between the lenses and feed horn and measurements are made to verify this distance. For the C type lens a similar procedure was followed to determine correct distance from the horn to the surface of the lens to ensure the scanning plane is in focus.

## 4.2 Lens Flat Phase Position

The M type lenses were designed to produce a beam with a flat phase front at the focal plane located at the scan plane. As the incident beam propagates the phase front becomes curved with the edges of the beam falling behind the phase in the centre. The higher refractive index material changes the speed with which the transmitted beam propagates and the greater thickness at the centre of the lens the beam has the centre phase brought back behind the phase of the edges. The transmitted beam then propagates until the phase front becomes even. This is the point we want to determine and set as the position for our scan plane. The lens is placed in the lens holder and positioned a set distance from the scan plane. A series of measurements are then performed to determine the flat phase front position. The scanner takes scans along the *x*-axis while the distance from the emitter horn to the lens is changed. The resultant phase is then assessed and the flat phase front position determined. This position is then used as the distance from the horn to the lens for all subsequent measurements.

We can see in Figure 45 data from analysis of the flat phase of the M1 lens. On the right of the figure is the phase which we use to determine the point of flattest phase. The *z*-axis in the diagram is the position of the translation stage from its zero position. A negative increase moves the emitter horn away from the face of the lens. The *x*-axis in the diagram is the position of the receiver on the *x*-axis of the scanner. The phase can be seen to change from rapid change from -80 to 80 mm on the *x*-axis at *z*=0 and no change at *z*=-165, where *z*=-165 mm is the flat phase position.

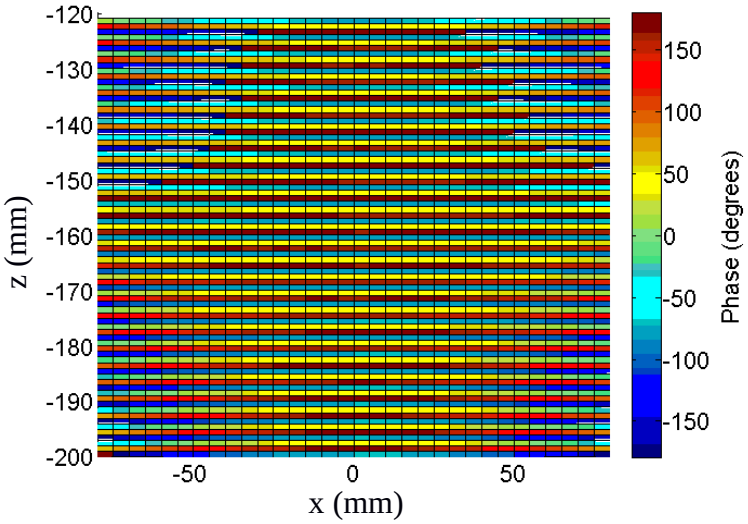


Figure 45: Data on finding the flat phase point for the M1 lens. We view the phase of the lens, on the right in this figure, and find the point of flattest phase. The phase changes for different *z* positions, where *z* is the distance from emitter horn to the lens, with flattest phase at z = -165 mm.

## 4.3 Lens Measurements

With the system setup and the distances between components and residual offsets of the system determined, the measurements of the lenses could be performed. Originally there were two measurements planned for each lens, one without the anti-reflection coating and one with the anti-reflection coating. This was changed after the measurement of the M1 lens due to the change during the coating process. The lens warped due to the heating involved in the coating process changing both the shape and refractive index as the material had not been annealed during manufacture. Due to this a third step was introduced to the M2 lens measurement in which the lens would be measured after manufacture then put through an annealing process measured again and then coated before a final measurement. After completion of the M type lenses it was

decided that the C type lenses originally made for testing in Cardiff University would be measured at Maynooth University. The measurements completed are listed below:

- M1 uncoated (unannealed)
- M1 coated (annealed)
- M2 uncoated (unannealed)
- M2 uncoated (annealed)
- M2 coated (annealed)
- C1 uncoated (annealed)
- C1 coated (annealed)

Measurements were not performed in this order and changes were necessary due to issues encountered during the measurement process, which will be discussed below. The measurements will be discussed in chronological order.

During each phases of measurements the following scans were performed:

- A full range scan to measure the beam pattern over the entire area of the lens
- A high resolution scan of the centre of the lens beam
- A feed horn measurement performed after the previous measurements were completed to ensure and verify that alignment had been maintained

The measurements were performed by taking a scan of the *x* and *y* axes of the scan plane, the translation stage in different positions and the rotation stage changing the angle of the lens with respect to the axis of propagation. The full range scan measurements of the lens were made using the following system parameters:

- *X*-axis position was changed from -140 to 140 mm in 5 mm step size (57 steps)
- *Y*-axis position was changed from -150 to 150 mm in 5 mm step size (61 steps)
- *Z*-axis position was changed differently for each lens as will be discussed
- $\alpha$ angle was changed from 0° to 15° in 5° step size (4 steps)

The high resolution measurements were performed with the following system parameters:

- *X*-axis position was changed from -40 to 40 mm in 1 mm step size (41 steps)
- *Y*-axis position was changed from -40 to 40 mm in 1 mm step size (41 steps)

This high resolution measurement was performed at only one *z* position and with no rotation of the lens.

The feed measurement of the horn was performed using the full range scan parameters used for the lens measurement (with the exception of $\alpha$, as the lens is not included in the setup.)

In the images shown through this section both H and E plane cuts will be shown. The H-plane is the plane perpendicular to the direction of the electric field and the direction of propagation of the beam. The E-plane is the same plane as the electric field direction. For our measurements cuts along the *x*-axis are H-plane cuts and along the *y*-axis are E-plane cuts.

### 4.3.1 M1 uncoated

The M1 uncoated measurement was the first measurement performed. For each measurement we will provide a table of the distances in the system, a table for the calculated offsets of the system and, due to the quantity of information gathered, a series of images of the most important results will be shown.

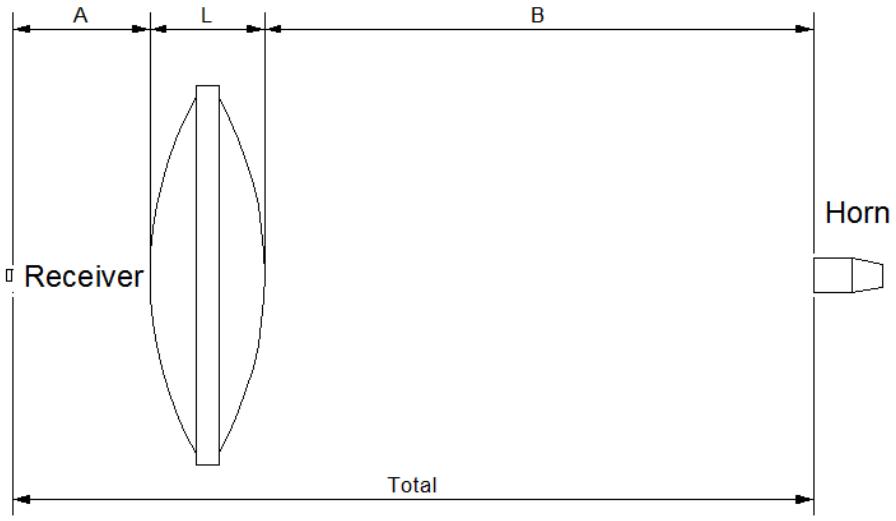


Figure 46: Description of system distances.

The distances shown in Table 8 are visually described in Figure 46.

Table 8: System distance parameters for M1 uncoated lens.

| **Parameter** | **Quantity** | **Unit** |
|---|---|---|
| Distance from horn to lens face (B) | 385.4±0.4 | mm |
| Distance from receiver to lens face (A) | 71±0.4 | mm |
| Distance from centre of lens to rotation point (C) | 18.0±1.2 | mm |
| Length of receiver waveguide | 12.5±0.1 | mm |
| Length of cross-polar twist | 32.0±0.1 | mm |

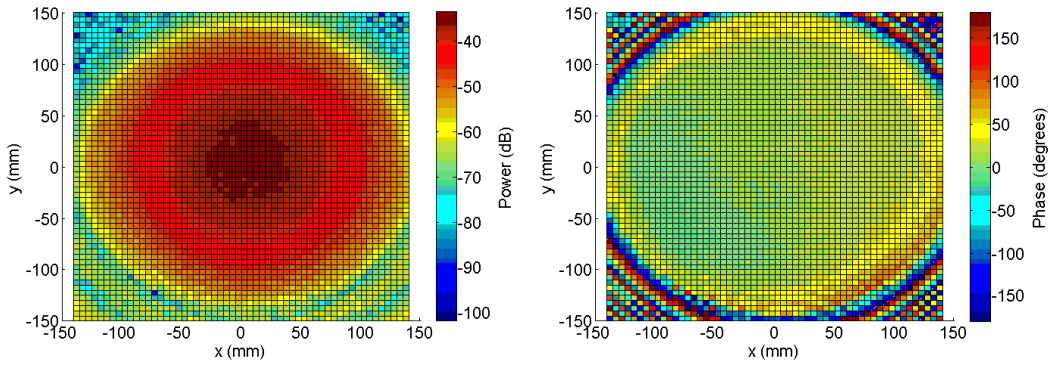


Figure 47: Full range scan with the lens at 0° angle and at 100 GHz. Shown in this figure and all the following figures of this type are: Power on dB scale, Phase in degrees. Power is absolute, as measured on the VNA receiver head port (with respect to the power transmitted out of the VNA transmitter head port); the feed horn and receiver probe are not de-embedded (de-convolved).

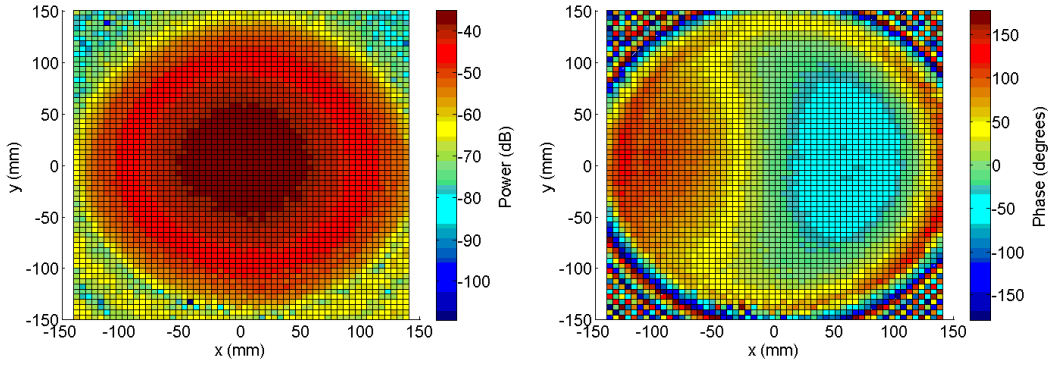


Figure 48: Full range scan with the lens at 10° angle and at 100 GHz.

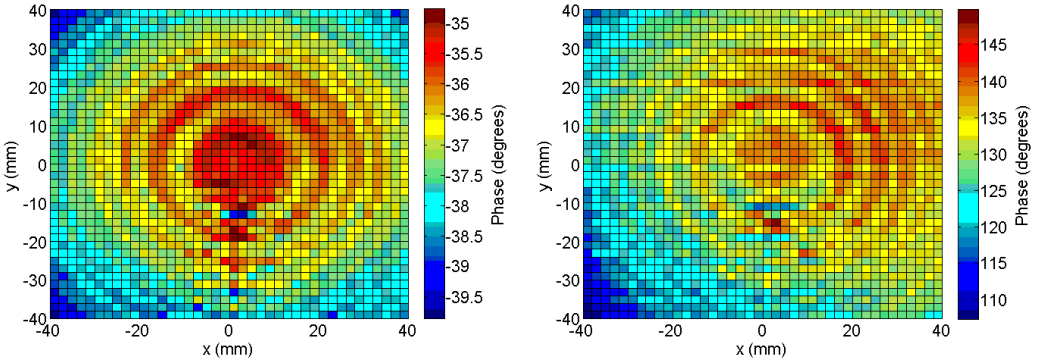


Figure 49: High resolution centre scan with the lens at 0° angle and at 100 GHz. Standing wave patterns between the probe and the lens, and internal to the lens, are clearly visible. Circular patterns are caused by internal reflections in the lens. The localised hotspot can be attributed to the coupling between the receiver probe and the support pillar of the receiver head via lens surface reflections.

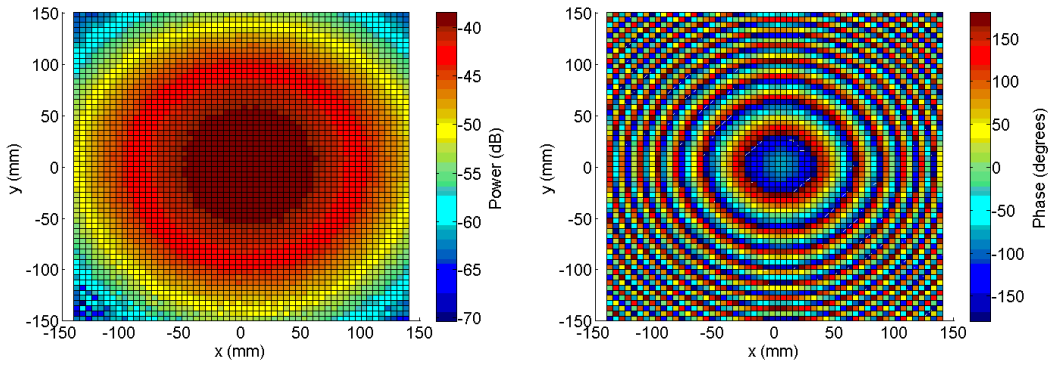


Figure 50: Feed horn pattern with lens removed, at 100 GHz.

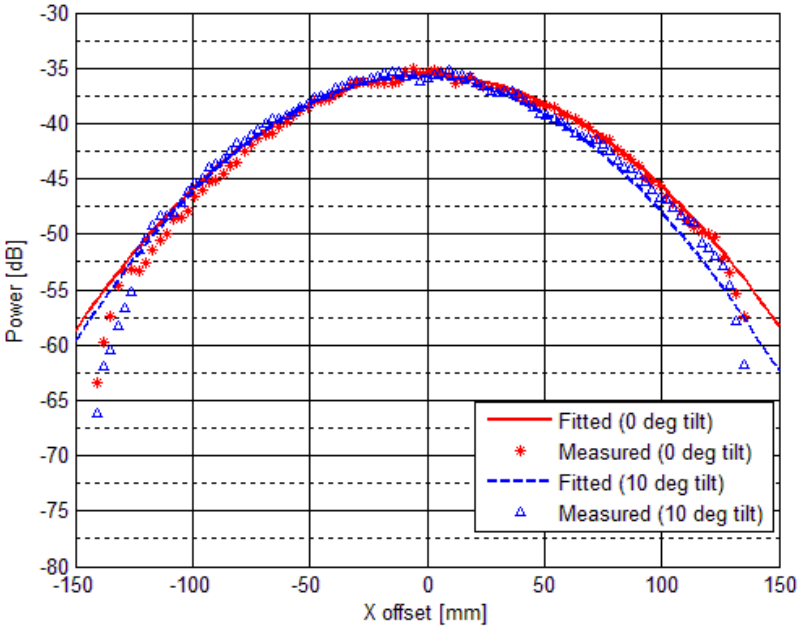


Figure 51: H-plane cut of power through the measured field pattern at 0° and 10° lens tilt. The fitted curves are fundamental Gaussian fits from the Gaussian Fitter program.

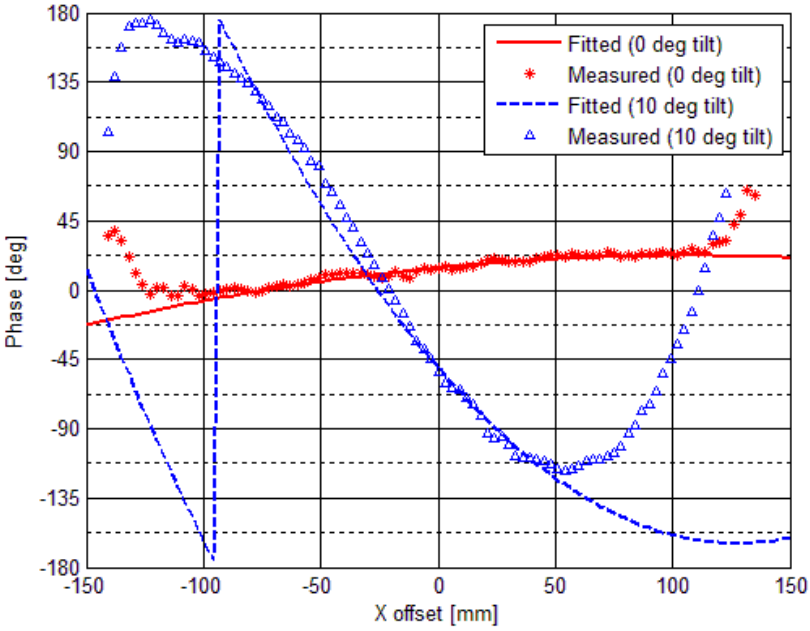


Figure 52: H-plane cuts through the measured field pattern with the lens at 0° and 10° tilt. The fitted curves are fundamental Gaussian fits from the Gaussian Fitter program.

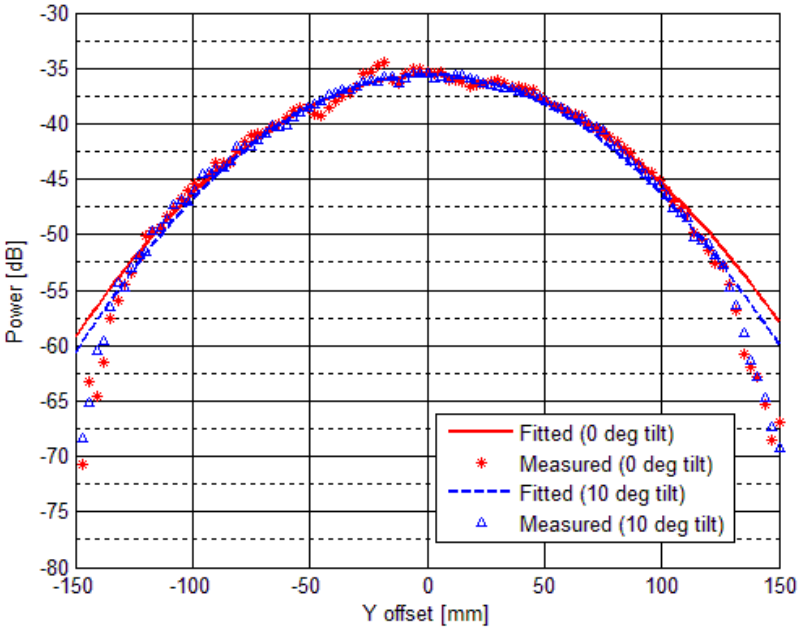


Figure 53: E-plane cuts of the power through the measured field pattern with the lens at 0° and 10° tilt. The fitted curves are fundamental Gaussian fits from the Gaussian Fitter program.

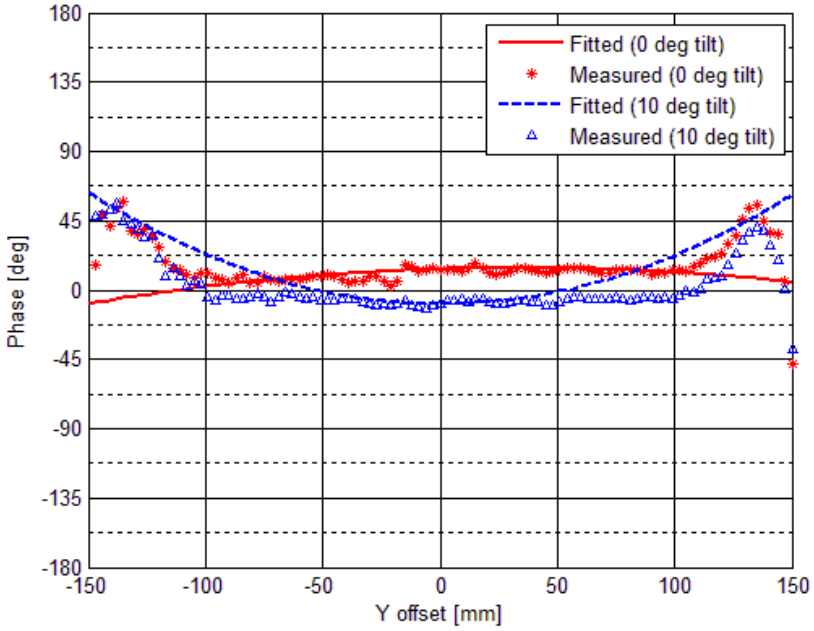


Figure 54: E-plane cuts of the phase through the measured field pattern with the lens at 0° and 10° tilt. The fitted curves are fundamental Gaussian fits from the Gaussian Fitter program. The curvature for the fitted phase at 10° is opposite as the program attempts to minimise the residuals over the entire beam pattern.

### 4.3.2 Refractive index discrepancy

After the measurement of the M1 uncoated lens was performed the results were sent to both Cardiff University and the TICRA institute in Denmark. TICRA created a model of the entire measurement system to match the 2D data measured by the measurements. A discrepancy was found between the model and measurement. The refractive index in the model was changed to try to match it to the measurement data. It was found that a lower value for the refractive index of 1.5188 resulted in good agreement between the model and measurement. This value was significantly different from the value of 1.5275 calculated from the test sample and used for the design of the lens. The extra C3 lens that was made during the manufacturing process as a backup was destroyed in order to take a sample to measure its refractive index. The refractive index of that sample was 1.51817±0.00006, a value close to the value of 1.5188 used by TICRA to match the model to the measurement data.

This was the first success of the measurements performed with respect to providing insight into the design and manufacturing processing of refractive optical elements for

use at terahertz frequencies. The accuracy and calculated offsets enabled accurate modelling to identify a discrepancy in the refractive index of the material.

### 4.3.3 M2 uncoated (unannealed)

The M1 lens was sent back to Cardiff University for it to undergo coating. Meanwhile the M2 uncoated (unannealed) lens was sent to MU for measurement. Below are the system distances as outlined for the M1 lens and a set of results for this lens.

Table 9: System distance parameters for the M2 uncoated (unannealed) lens.

| **Parameter** | **Quantity** | **Unit** |
|---|---|---|
| Distance from horn to lens face (B) | 385±0.4 | mm |
| Distance from receiver to lens face (A) | 71±0.4 | mm |
| Distance from centre of lens to rotation point (C) | 18.0±1.2 | mm |
| Length of receiver waveguide | 12.5±0.1 | mm |

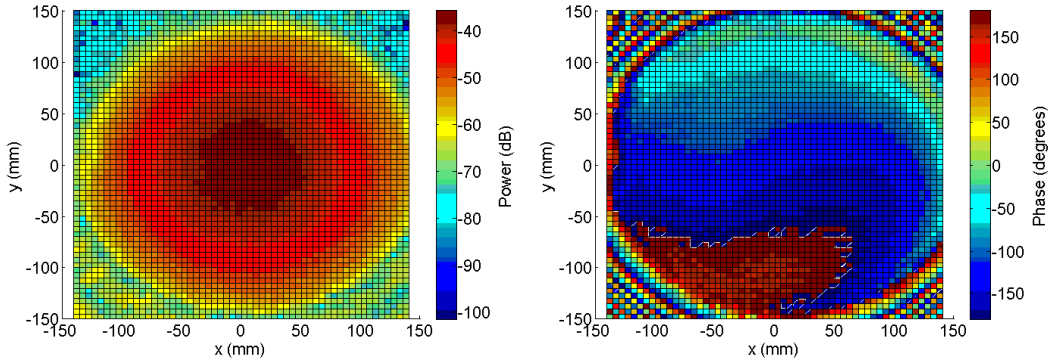


Figure 55: Full range scan with the lens at 0° angle at 100 GHz.

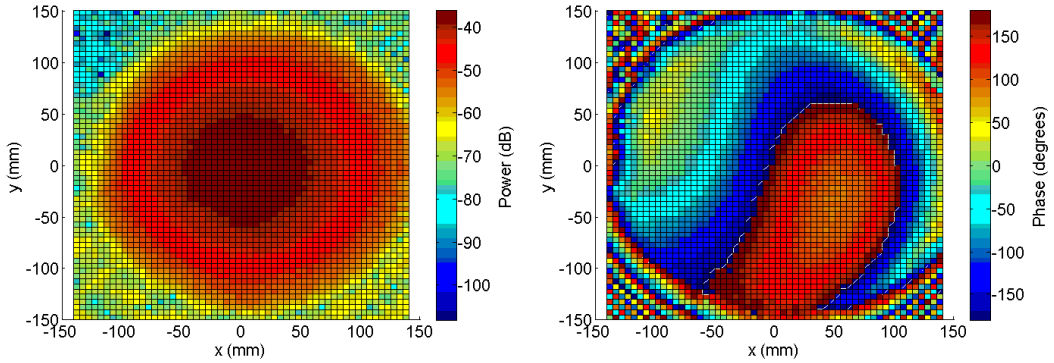


Figure 56: Full range scan with the lens at 10° angle and at 100 GHz.

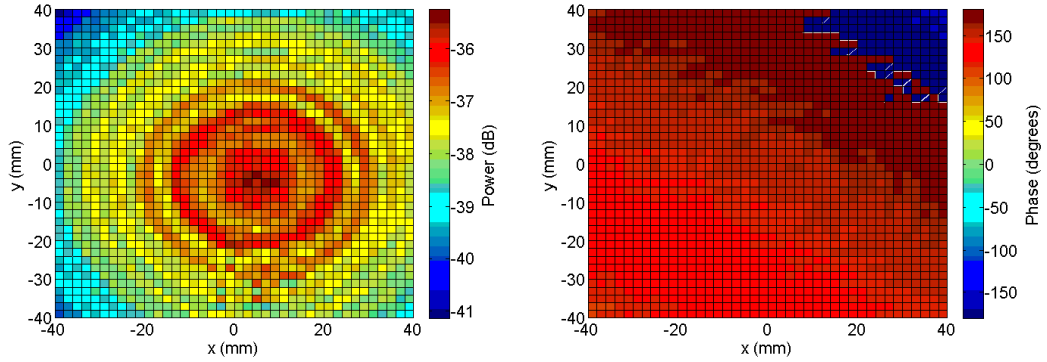


Figure 57: High resolution centre scan with the lens at 0° angle and at 100 GHz. Standing wave pattern between the probe and the lens, and internal to the lens, is clearly seen.

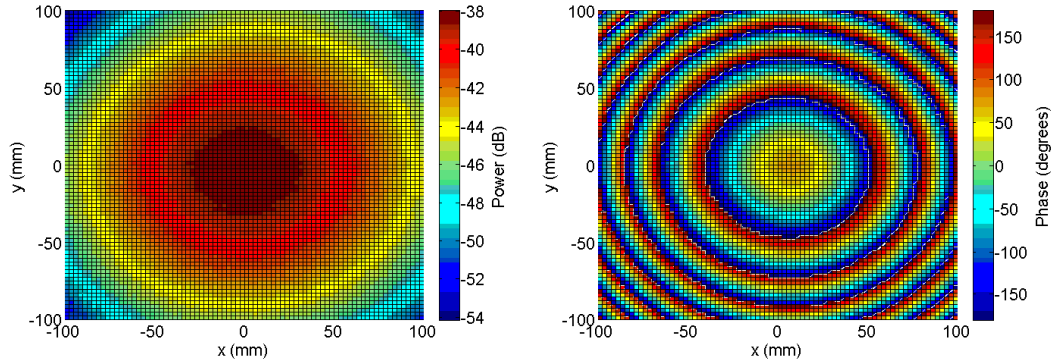


Figure 58: Feed horn pattern with lens removed, at 100 GHz.

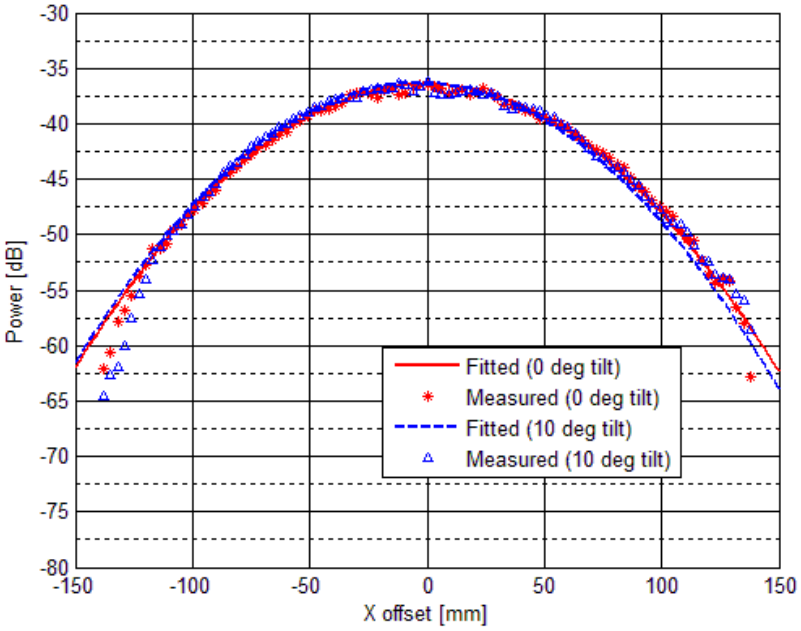


Figure 59: H-plane cut of power through the measured field pattern with lens at 0° and 10° tilt.

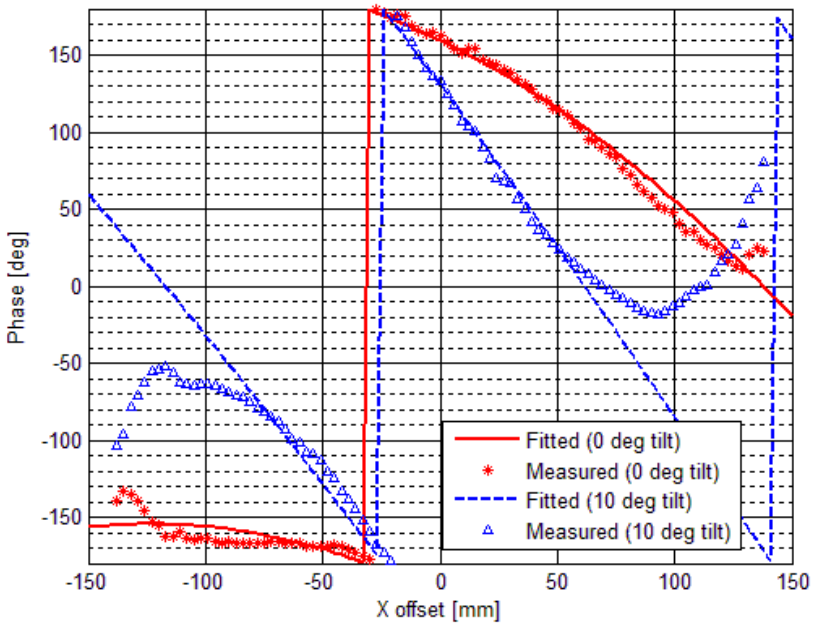


Figure 60: H-plane cut of phase through the measured field pattern with lens at 0° versus 10° tilt. The 10 degree tilt shows deviation between the measurement and fit due to the impact of the lens holder on the beam.

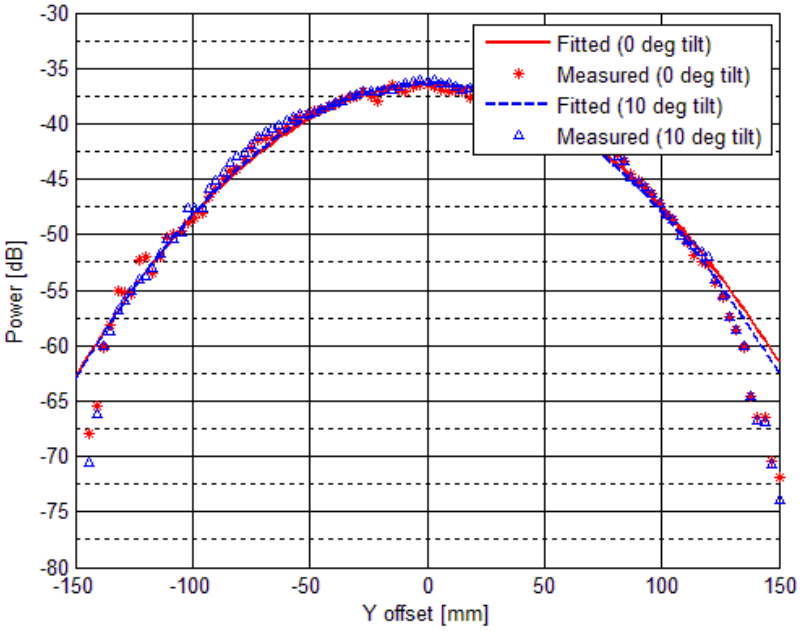


Figure 61: E-plane cut of power through the measured field pattern with lens at 0 degrees and 10 degrees tilt.

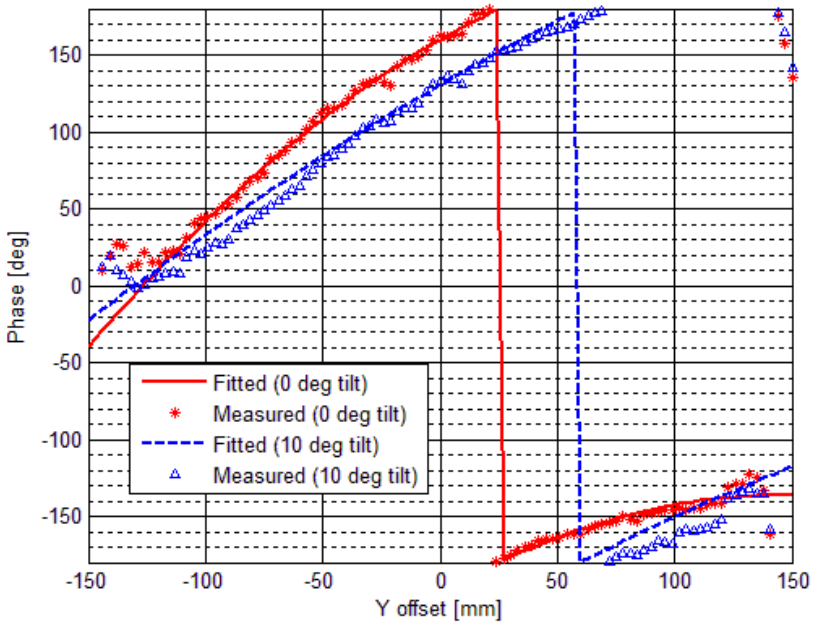


Figure 62: E-plane cut of phase through the measured field pattern with the lens at 0 degrees tilt versus 10 degrees tilt.

### 4.3.4 Annealing issue with M1 lens

During the coating process the lens undergoes an effective annealing process due to the heating of the lens. The M1 lens shrunk in size during this process. This effect should not have occurred as the material should have been annealed during the

manufacturing process. In order to assess the effect of this process on the lens it was decided to introduce an extra step to the measurement process for the M2 lens. The lens would be annealed and re-measured before the coating was applied in order to assess the effect of the annealing. The annealing changed the refractive index to a value of 1.5141±0.0002.

### 4.3.5 M1 coated (annealed)

The M1 coated lens was the next measurement performed. Due to the shrinking of the lens during the coating process the mounting screw holes had to be enlarged to allow mounting to the holder. This created a degree of uncertainty in the positioning of the lens in the holder. Best efforts were made to place the lens centrally but offsets along both the *x* and *y* axes were possible and would be assessed during the modelling process.

Table 10: System distances for M1 coated.

| **Parameter** | **Quantity** | **Unit** |
|---|---|---|
| Distance from horn to lens face (B) | 371.4±0.4 | mm |
| Distance from receiver to lens face (A) | 71±0.4 | mm |
| Distance from centre of lens to rotation point (C) | 18.0±1.2 | mm |
| Length of receiver waveguide | 12.5±0.1 | mm |

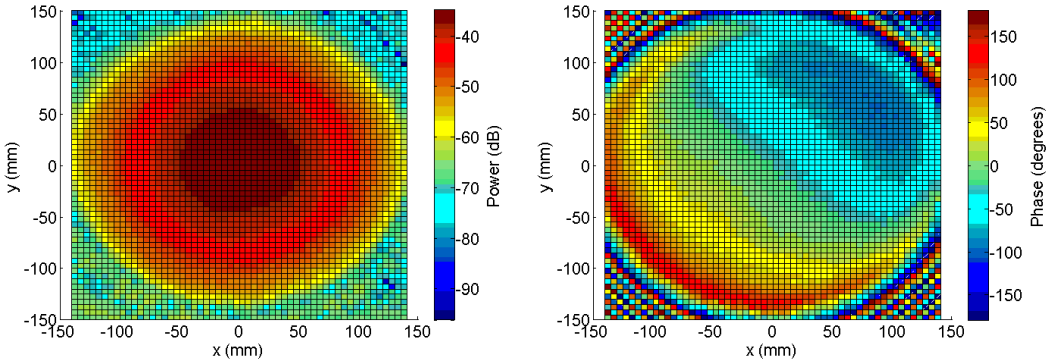


Figure 63: Full range scan with the lens at 0 degrees angle and at 100 GHz.

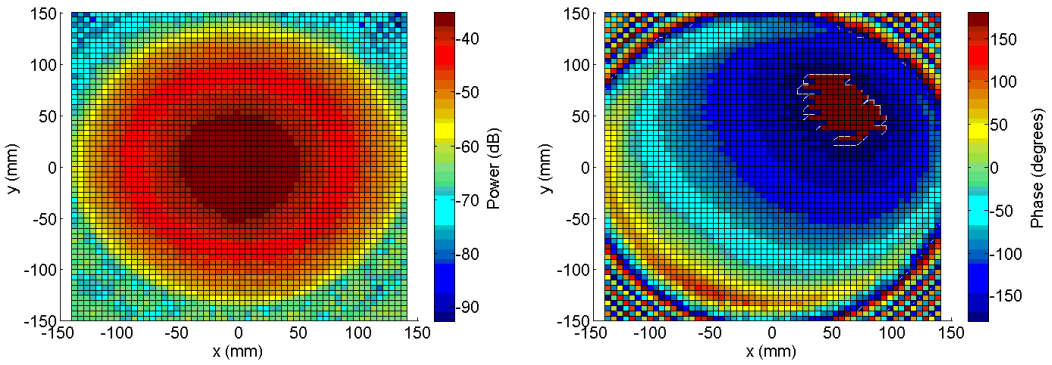


Figure 64: Full range scan with the lens at 10 degrees angle and at 100 GHz.

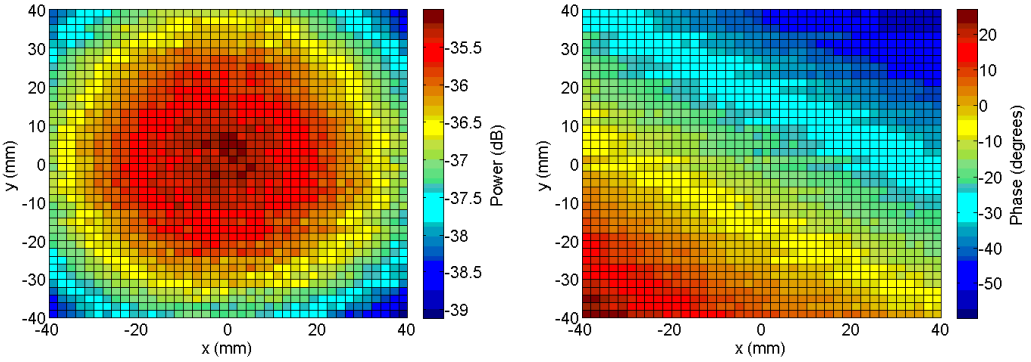


Figure 65: High resolution centre scan with the lens at 0 degrees angle and at 100 GHz. Standing wave pattern due to multiple reflections between the probe and the lens, and internal to the lens, is not visible.

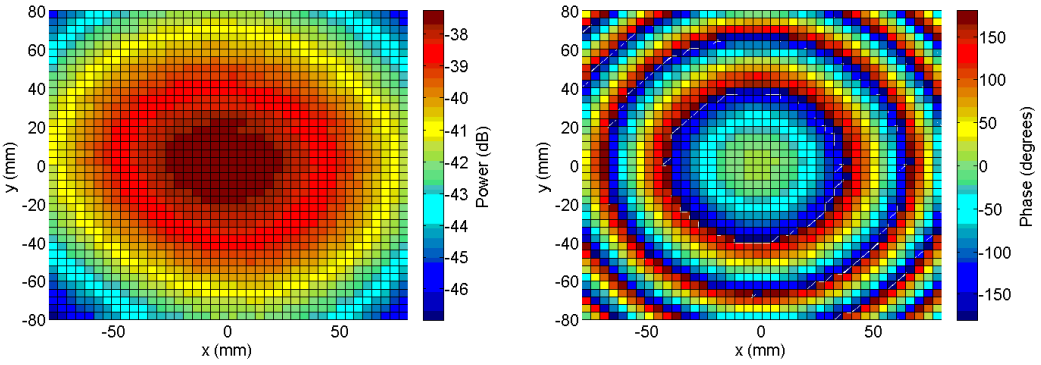


Figure 66: Feed horn pattern with the lens removed, at 100 GHz.

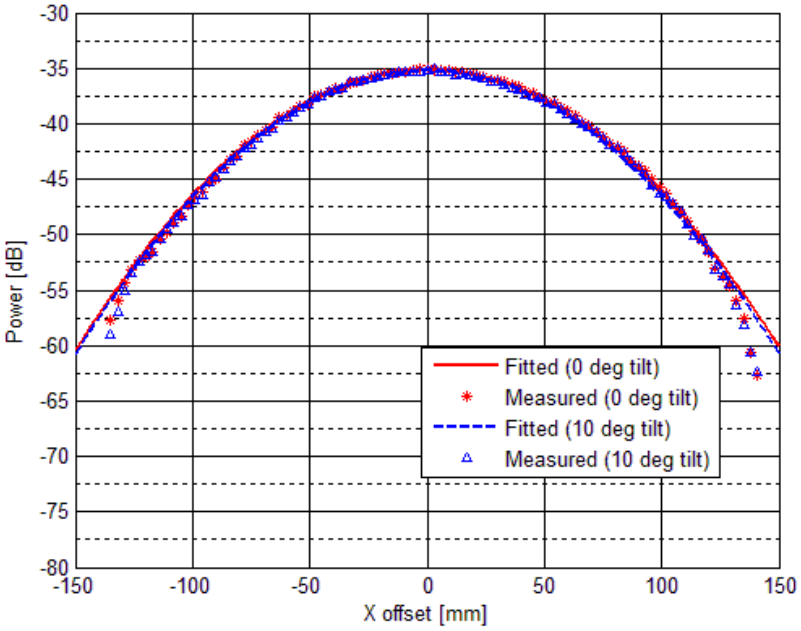


Figure 67: H-plane cut of power through the measured field pattern with lens at 0 degrees and 10 degrees tilt.

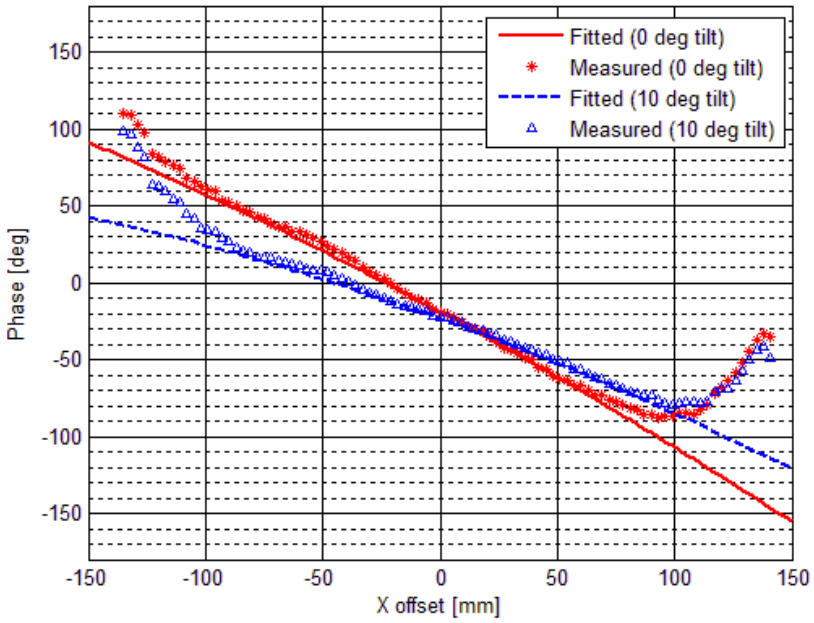


Figure 68: H-plane cut of phase through the measured field pattern with the lens at 0 degrees tilt versus 10 degrees tilt.

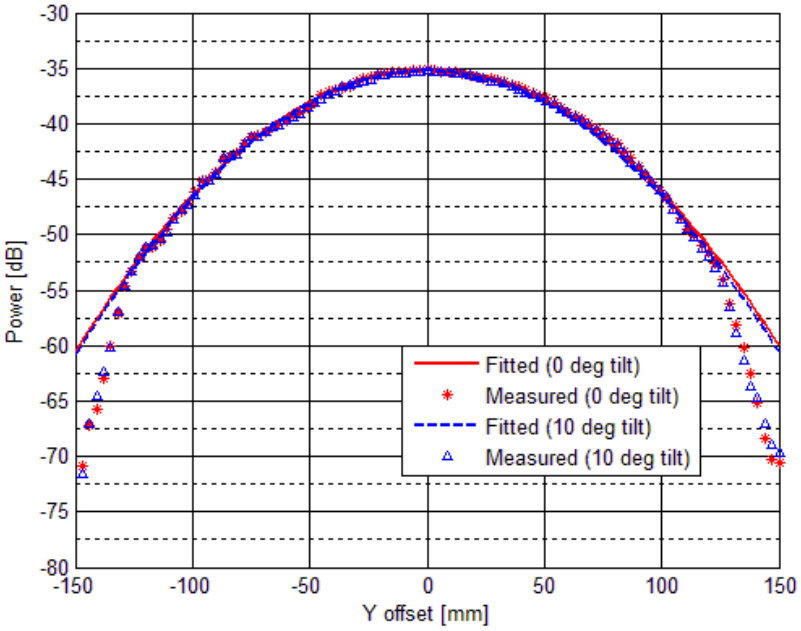


Figure 69: E-plane cut of power through the measured field pattern with lens at 0 degrees and 10 degrees tilt.

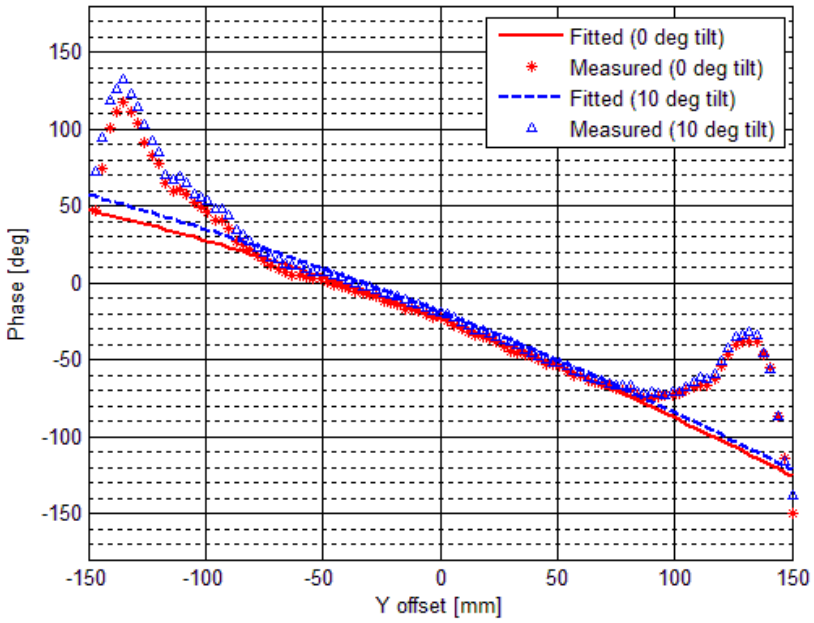


Figure 70: E-plane cut of phase through the measured field pattern with the lens at 0 degrees tilt versus 10 degrees tilt.

### 4.3.6 Analysis of standing wave effects

From the measurement of the M1 uncoated lens we observed standing wave effects in the high resolution scan behind the centre of the lens. With the M1 Coated

measurement completed we could compare the two measurements to each other and assess the effectiveness of the anti-reflective coating.

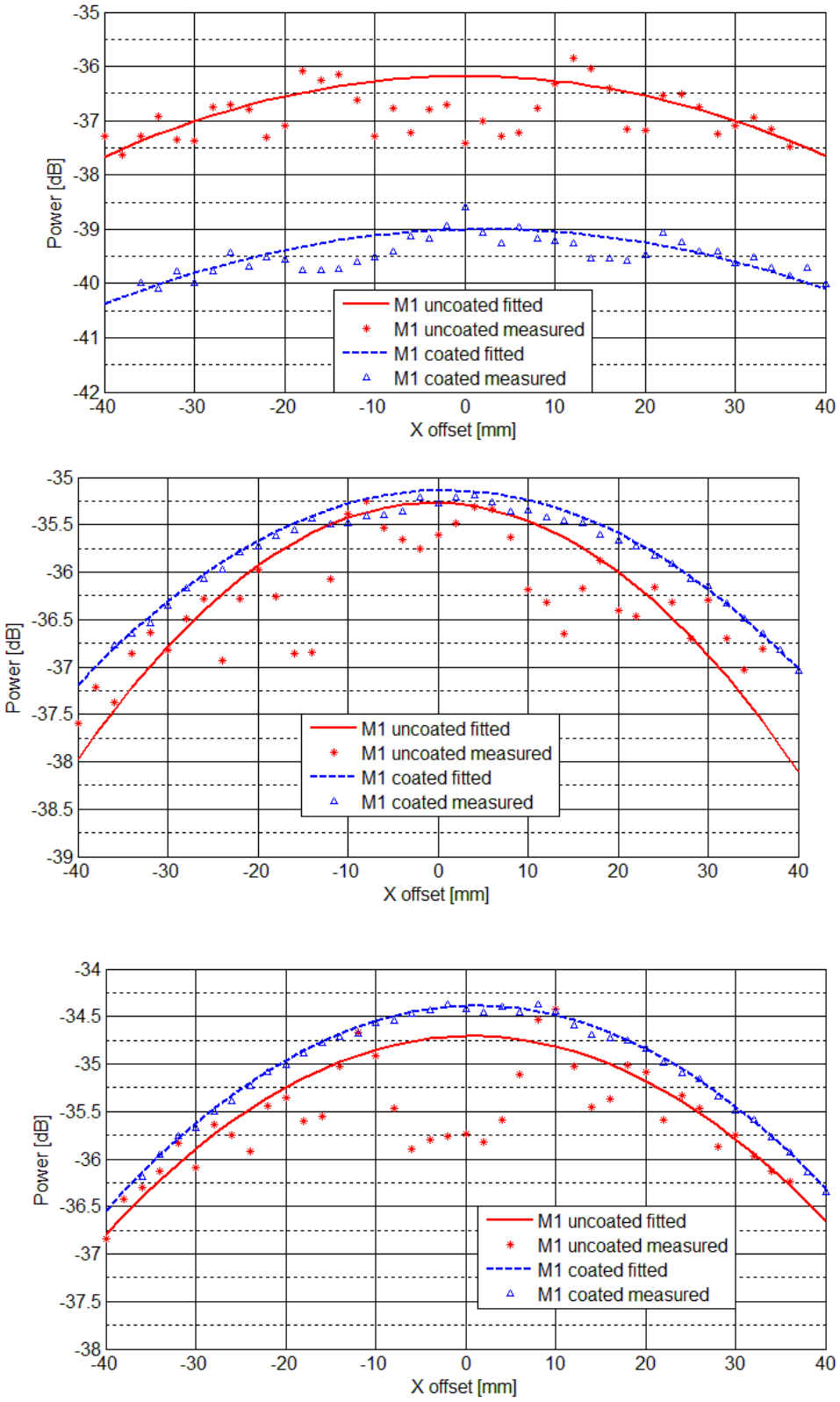


Figure 71: H-plane power at 75 (top), 100 (middle) and 110 GHz (bottom).

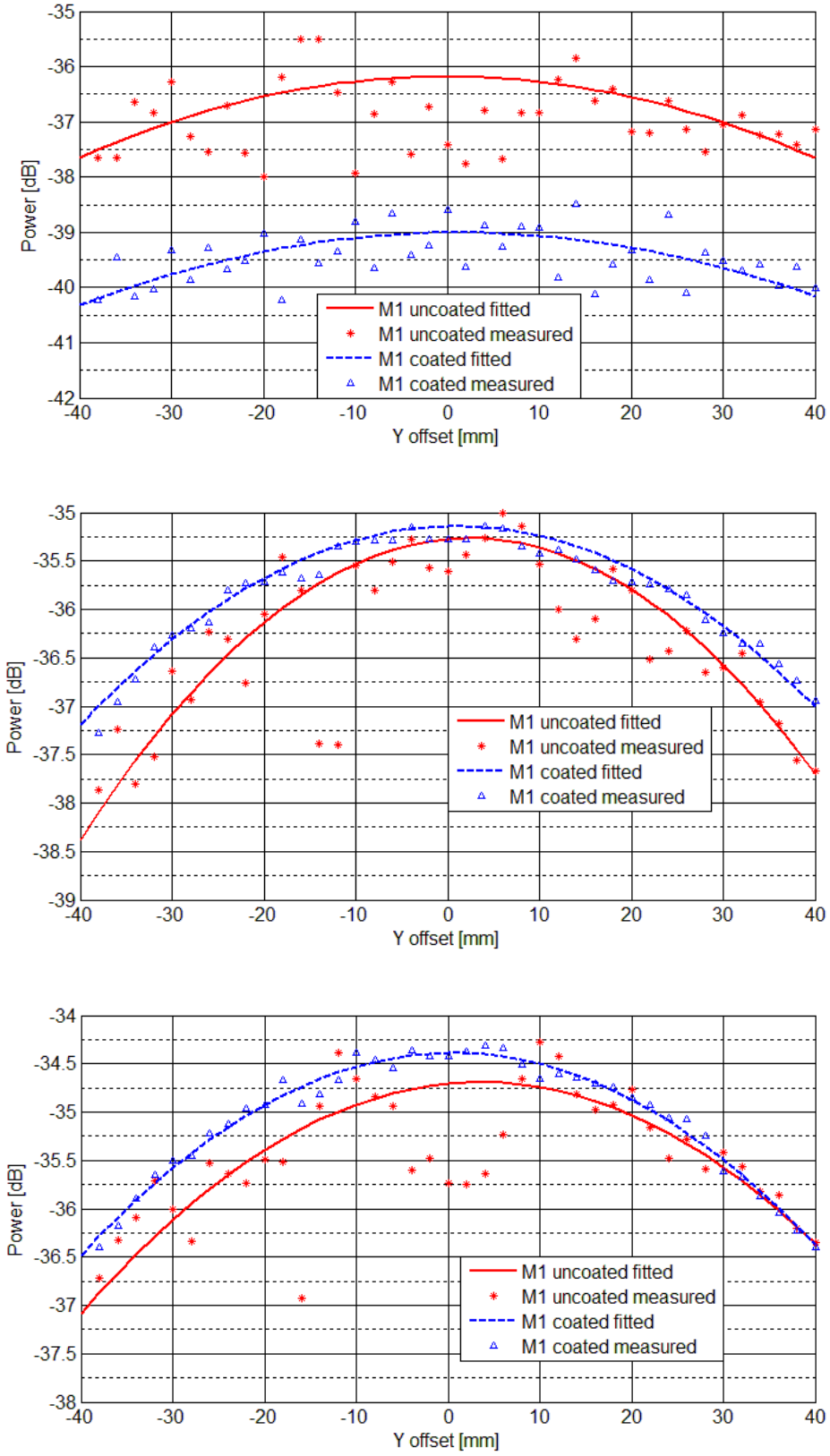


Figure 72: E-plane power at 75, 100 and 110 GHz, respectively.

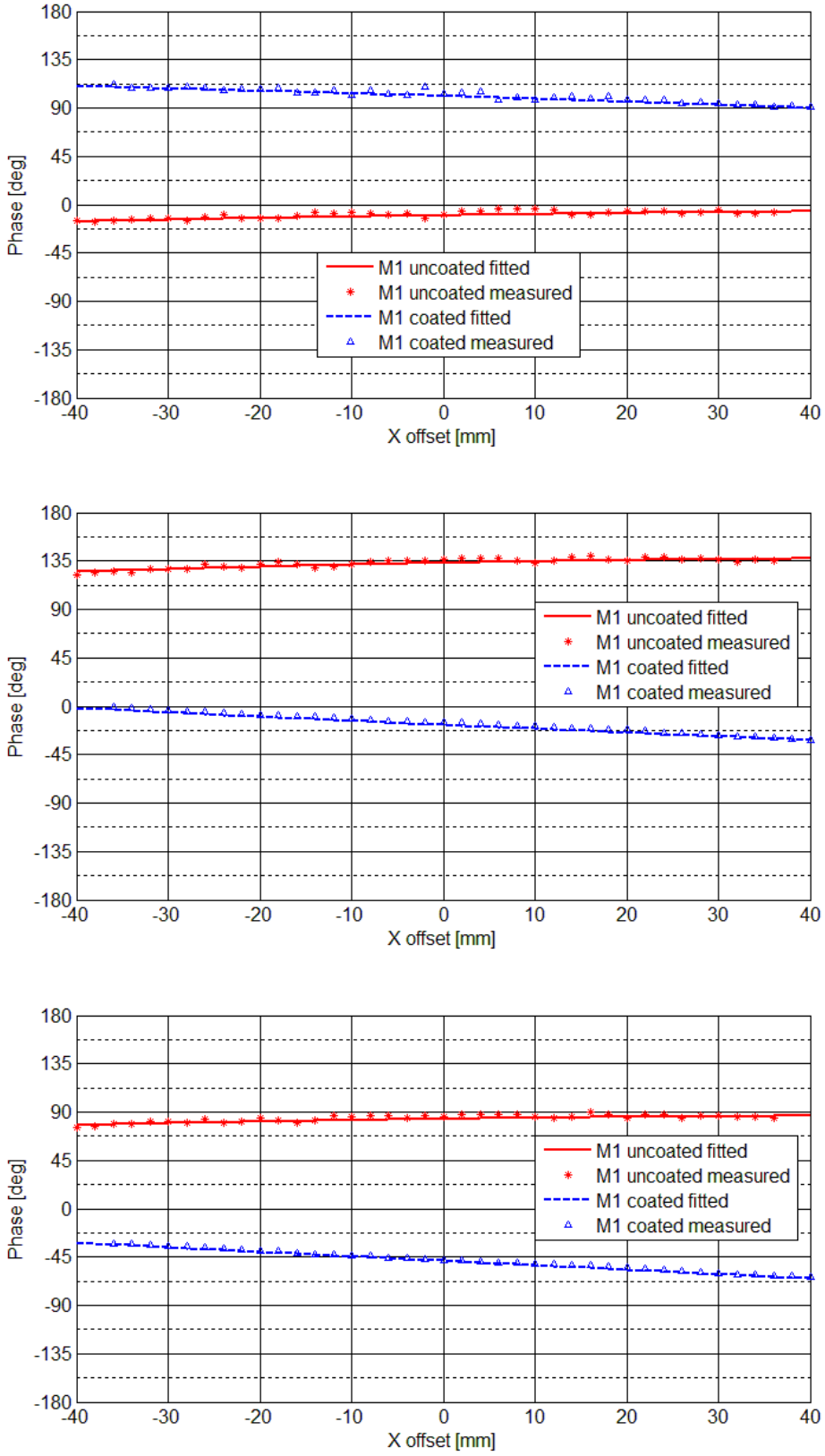


Figure 73: H-plane phase at 75, 100 and 110 GHz, respectively.

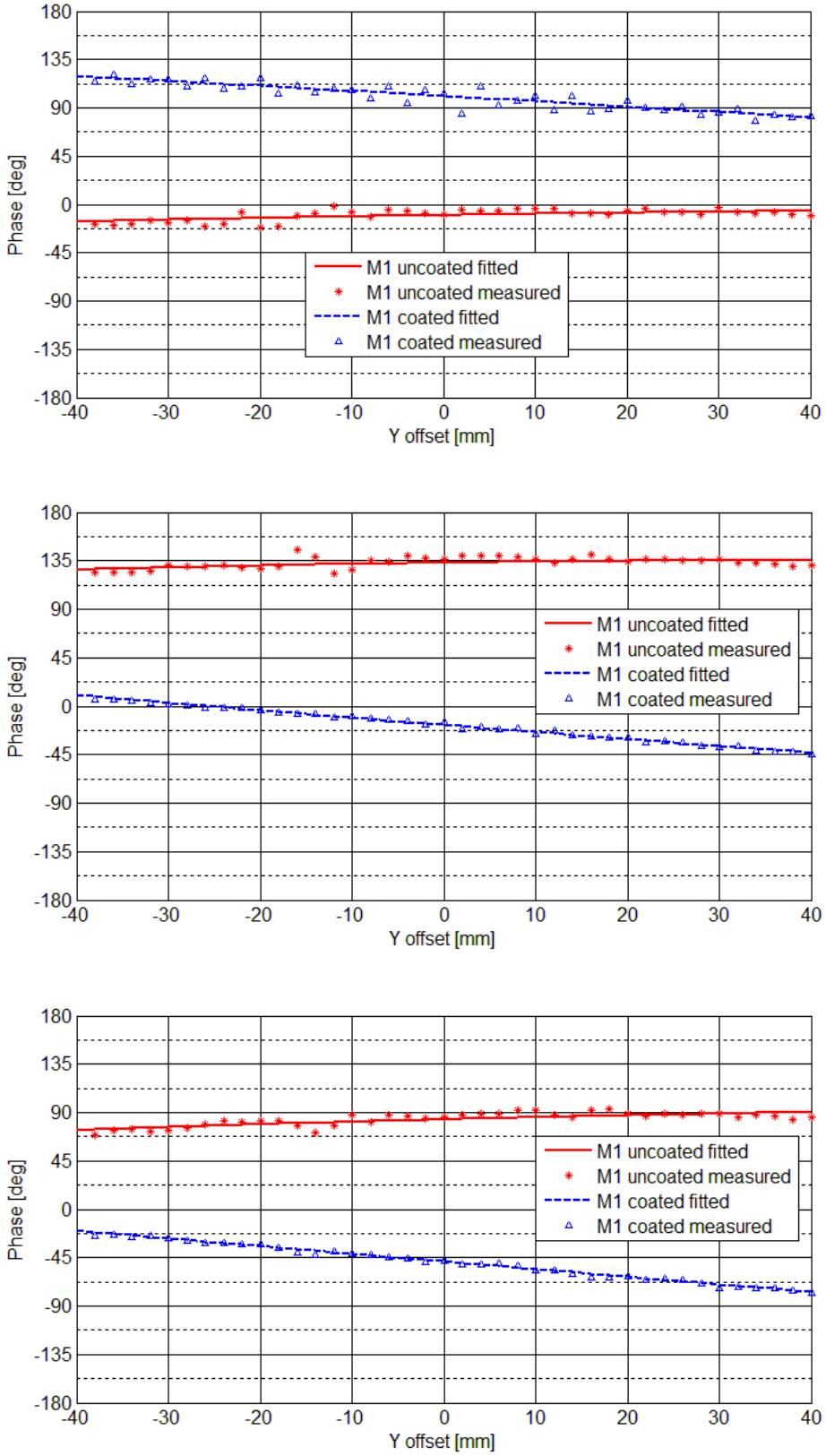


Figure 74: E-plane phase at 75, 100 and 110 GHz, respectively.

It is clear from the data that the anti-reflection coating performs very well at the design frequency of 100 GHz, but its effectiveness decreases as the frequency deviates

from 100 GHz. At 110 GHz there is still a significant reduction in the level of standing waves caused by reflections from the surfaces of the lens. At the other extreme of the W-band (75 GHz) the reduction is much less significant.

### 4.3.7 M2 uncoated (annealed)

The M2 lens was sent from CU to MU after the annealing process but before the coating was applied to assess the change due to the annealing. The lens had shrunk similarly to the M1 lens. Due to this change in the lens the refractive index retesting of the extra C3 lens that was being performed was also performed on a sample of the lens that was annealed to see if the process affected the refractive index value. The value of the refractive index was found to be 1.5141. This will be used in the subsequent MODAL simulations for the lens, as described section 5.2.

| **Parameter** | **Quantity** | **Unit** |
|---|---|---|
| Distance from horn to lens face (B) | 364.4±0.4 | mm |
| Distance from receiver to lens face (A) | 71±0.4 | mm |
| Distance from centre of lens to rotation point (C) | 18.0±1.2 | mm |
| Length of receiver waveguide | 12.5±0.1 | mm |

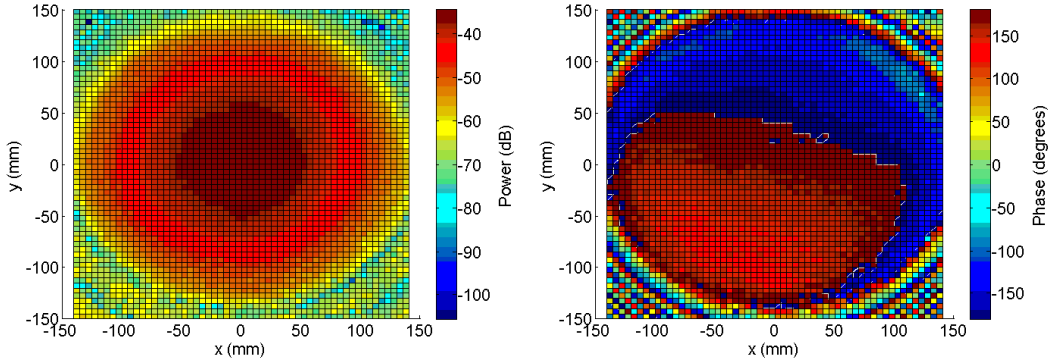


Figure 75: Full range scan with lens at 0° angle at 100 GHz.

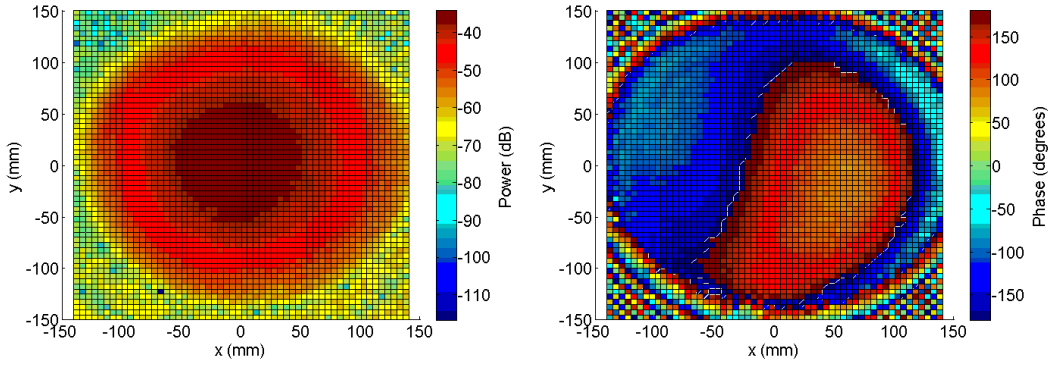


Figure 76: Full range scan with the lens at 10° angle at 100 GHz.

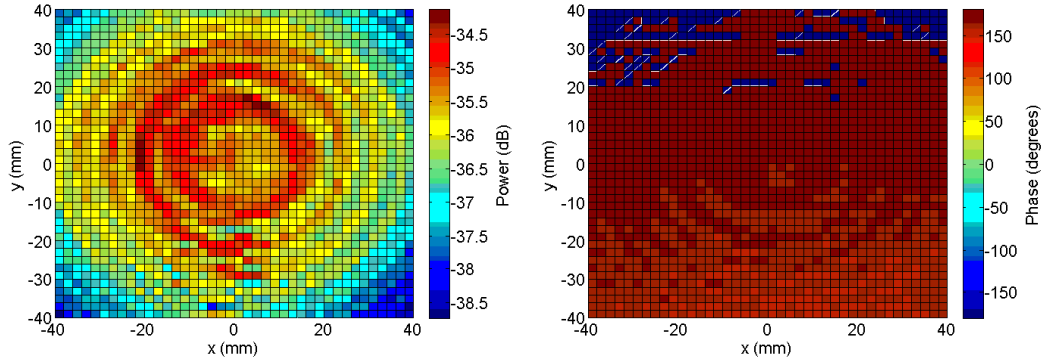


Figure 77: High resolution centre scan with the lens at 0° angle at 100 GHz. Standing wave pattern between the probe and the lens, and internal to the lens, is clearly seen.

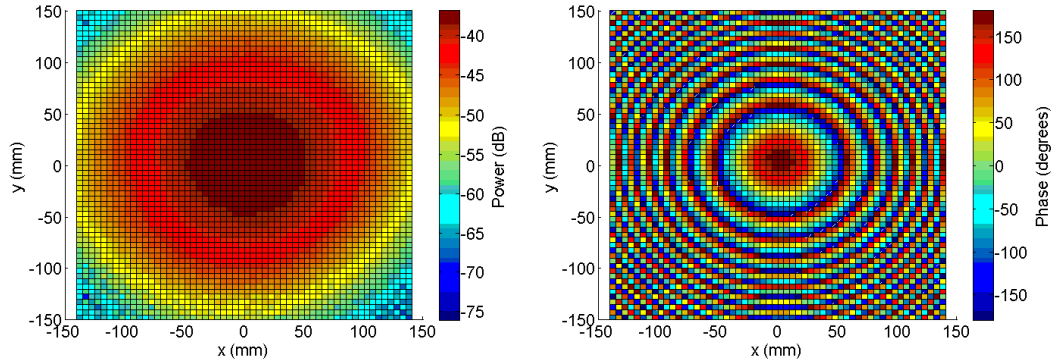


Figure 78: Feed horn pattern with the lens removed, at 100 GHz.

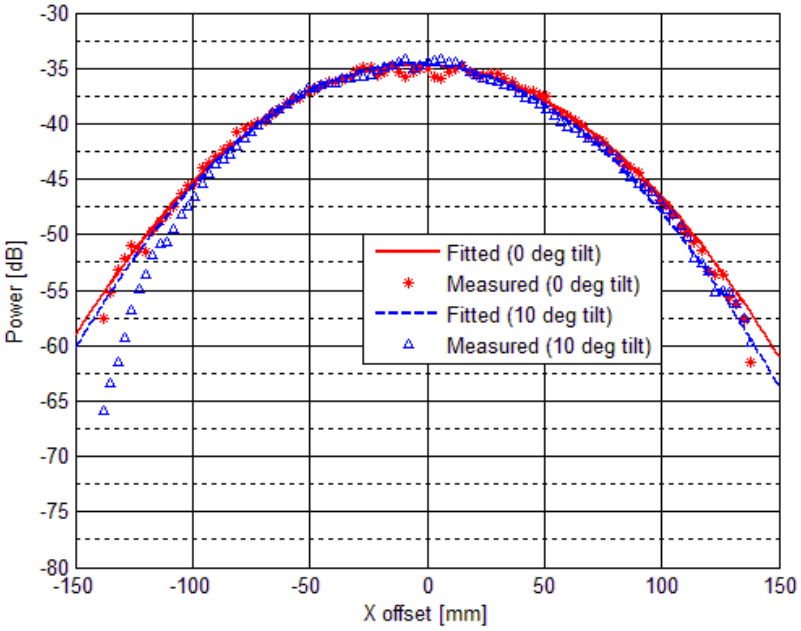


Figure 79: H-plane cut of power through the measured field pattern with the lens at 0° tilt versus 10° tilt.

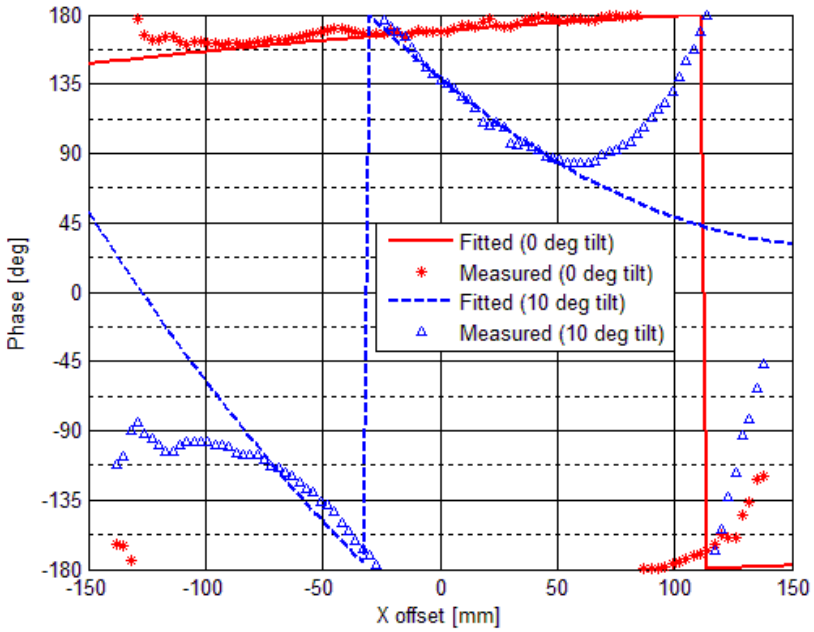


Figure 80: H-plane cut of phase through the measured field pattern with the lens at 0° tilt versus 10° tilt.

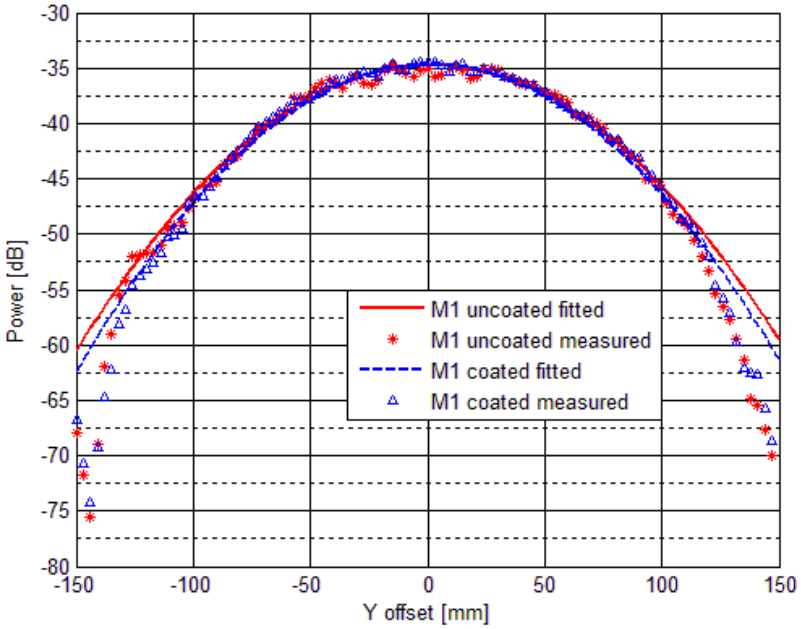


Figure 81: E-plane cut of power through the measured field pattern with the lens at 0° versus 10° tilt.

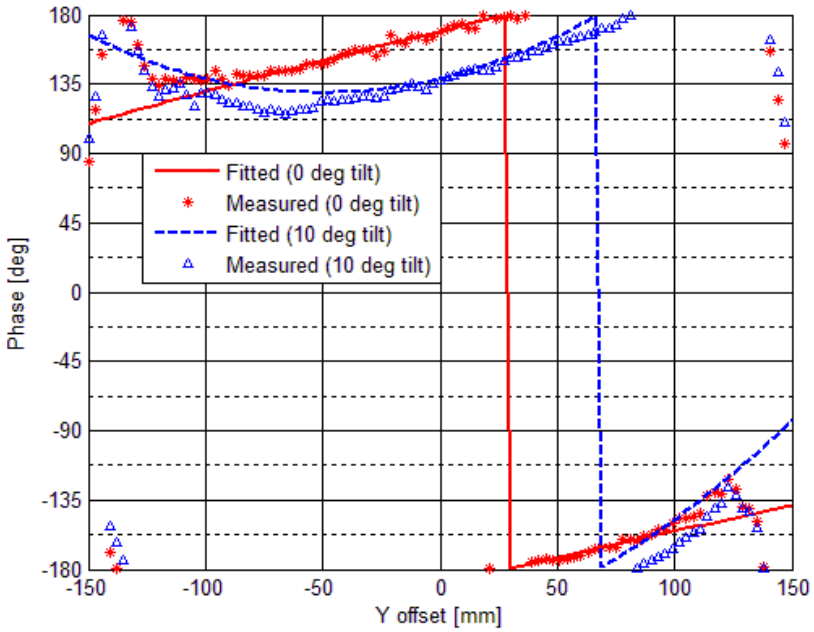


Figure 82: E-plane cut of phase through the measured field pattern with the lens at 0° versus 10° tilt.

### 4.3.8 M2 coated (annealed)

The M2 lens was then sent back to Cardiff University to be coated and then re-measured at Maynooth.

Table 11: Distance Parameters for the M2 coated lens.

| Parameter | Quantity | Unit |
|---|---|---|
| Distance from horn to lens face (B) | 360±0.4 | mm |
| Distance from receiver to lens face (A) | 71±0.4 | mm |
| Distance from centre of lens to rotation point (C) | 18.0±1.2 | mm |
| Length of receiver waveguide | 12.5±0.1 | mm |

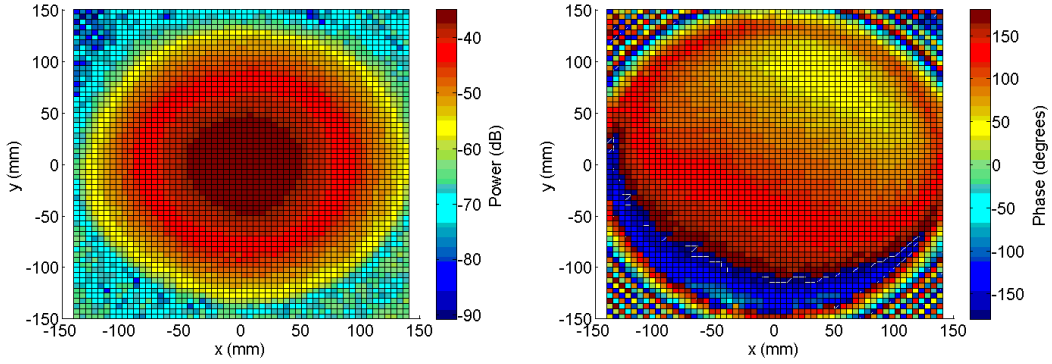


Figure 83: Full range scan with the lens at 0° angle at 100 GHz.

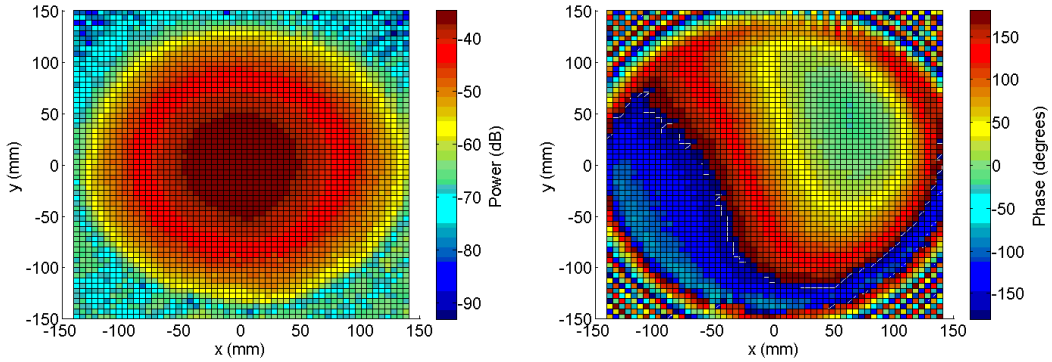


Figure 84: Full range scan with lens at 10° angle at 100 GHz.

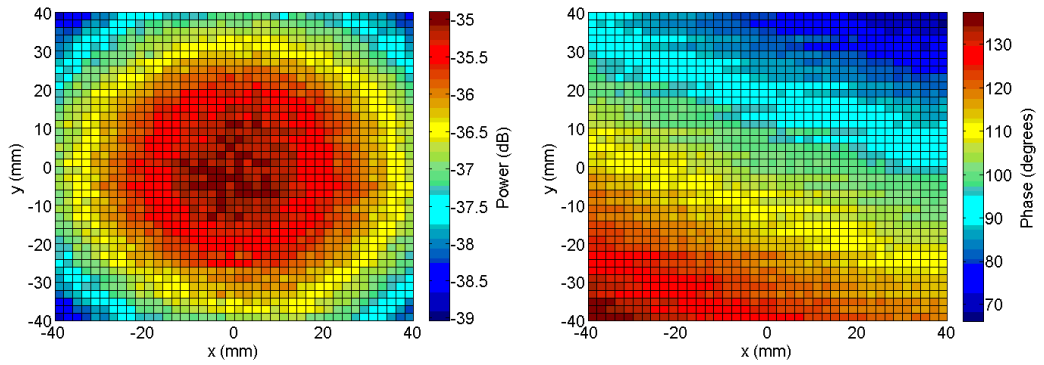


Figure 85: High resolution centre scan with the lens at 0° angle at 100 GHz. Standing wave pattern between the probe and the lens, and internal to the lens, is clearly seen.

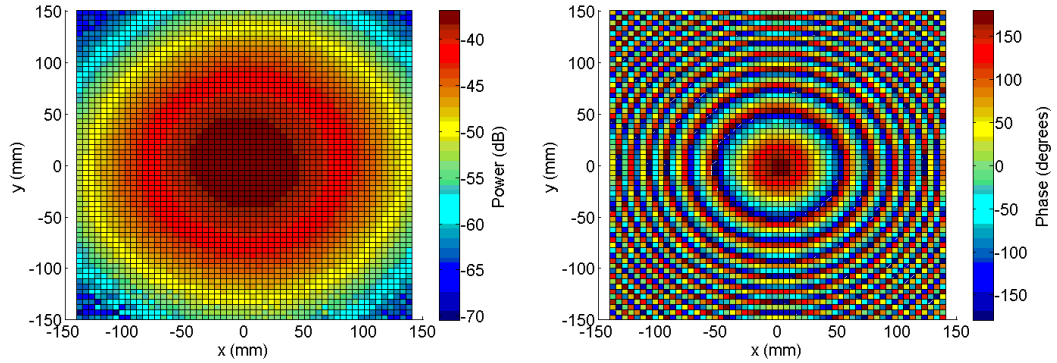


Figure 86: Feed horn pattern with lens removed, at 100 GHz.

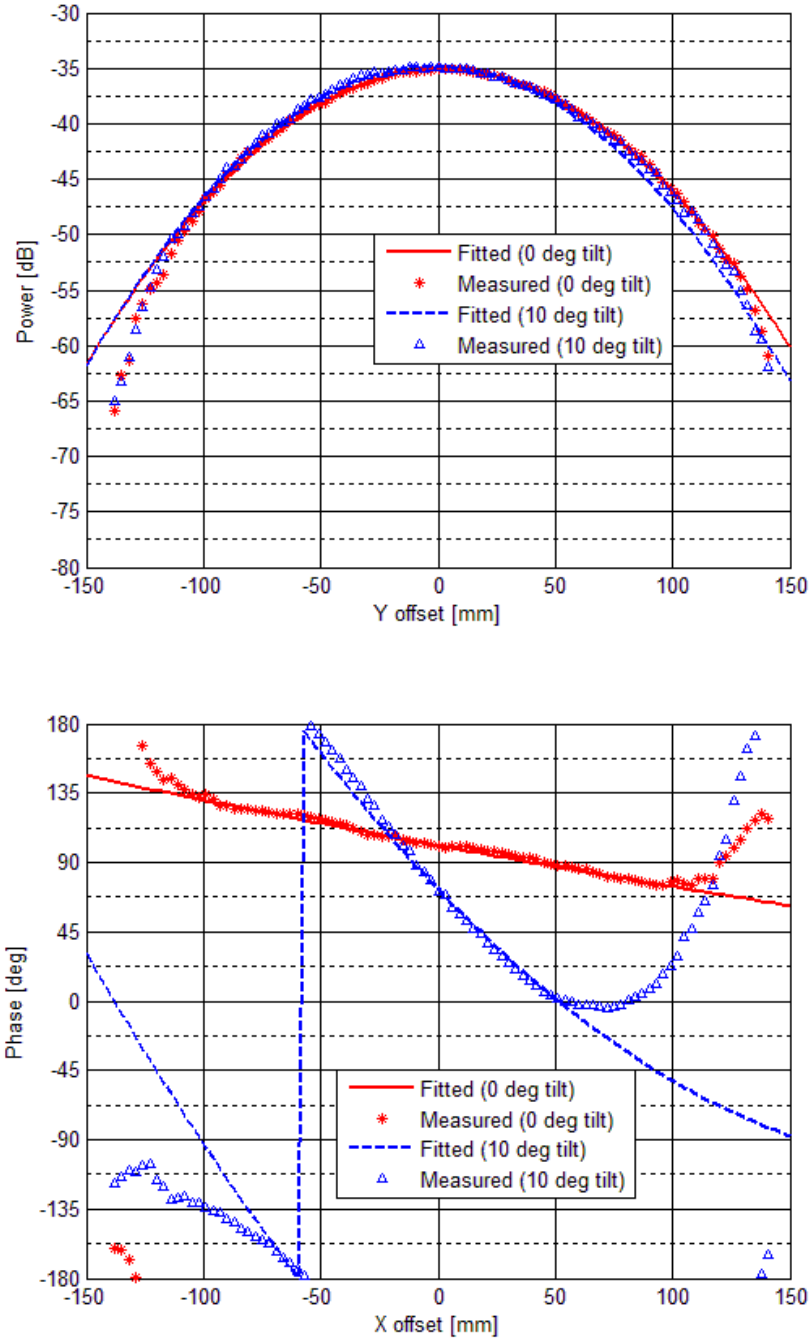


Figure 87: H-plane cuts through the measured field pattern with the lens at 0° versus 10° tilt.

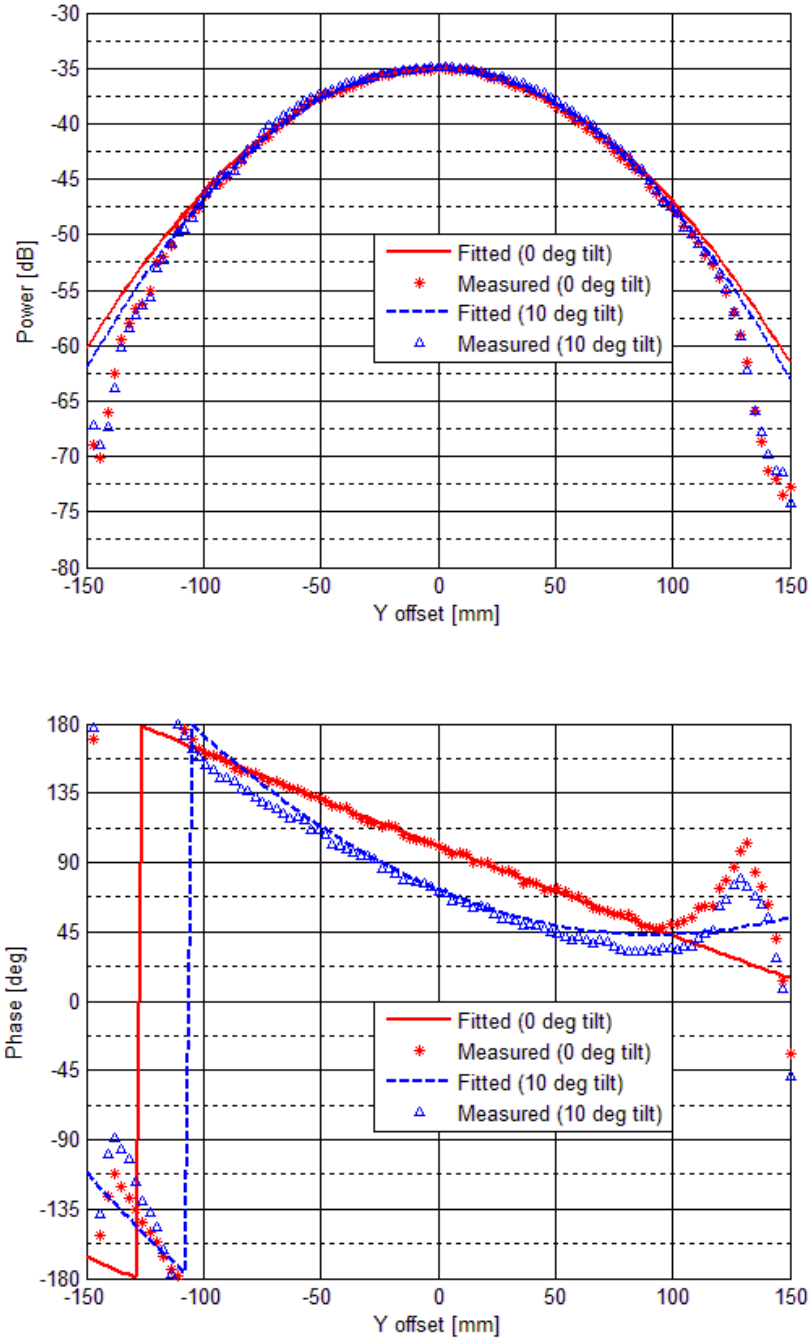


Figure 88: E-plane cuts through the measured field pattern with the lens at 0° versus 10° tilt.

### 4.3.9 Change to lens profiles during annealing

During the coating process for the M1 type lens it was found that the shape of the lens had changed. This was due to the annealing effect during coating and was not expected to effect the lens as the material was supposed to have been annealed during the manufacturing process. After measuring the surface profile of the lens subsequently, it was found that the overall thickness and curvature of the lenses had been altered. The

results can be seen in Table 12 showing significant change to the curvature and thickness of the lens resulting in a significant change in performance of the lenses in terms of the location of flat phase for the lenses.

Table 12: Shown are the radius of curvature refractive index and thicknesses for each lens, in each state of the testing process.

| M1 | R2 (mm) | k2 | R1 (mm) | k1 | Index | Thickness (mm) |
|---|---|---|---|---|---|---|
| As manufactured | 425.793 | -4.885 | 400.485 | -2.141 | 1.5188 | |
| Post annealing/coating | 414.099 | -3.79516 | 384.407 | -1.77069 | 1.5141 | |
| | | | | | | |
| M2 | R2 (mm) | k2 | R1 (mm) | k1 | Index | Thickness (mm) |
| As manufactured | 422.765 | -4.65103 | 397.132 | -2.40293 | 1.5188 | 56.687 |
| Post annealing | 407.001 | -4.47206 | 376.399 | -2.15936 | 1.5141 | 58.066 |
| Post coating | 403.676 | -3.50984 | 376.583 | -1.96631 | 1.5141 | 59.883 |
| | | | | | | |
| C1 | R2 (mm) | k2 | R1 (mm) | k1 | Index | Thickness (mm) |
| As manufactured | 198.915 | -2.28853 | 198.333 | -2.37523 | 1.5188 | 99.777 |
| Post annealing | 191.561 | -2.28853 | 189.444 | -2.30739 | 1.5141 | 101.909 |
| Post coating | 191.7 | -2.1109 | 189.742 | -2.1702 | 1.5141 | 103.149 |

### 4.3.10 Introduction to C Type lens measurements

After the success of the M lens measurements we were given the task of measuring the C type lenses. They had already been tested by Cardiff University and taken to the coating stage. The purpose was to confirm the focus point for the lens which they had determined and to image the width of the beam and the phase profile.

The alignment steps remained the same as for the M type lens. The main difference was in the determination of the focus point for the lens. In this measurement the focus point of the lens was determined by taking cut scans along the *x*-axis of the lens with the emitter horn at different distances to the lens, see Figure 89. The power was then assessed at each point and the point at which the waist of the beam was the narrowest was taken as the focus point for the lens. Due to the lens being a focusing lens and symmetric, the distance between the lens and receiver probe was increased to be close to the designed focus position of the lens.

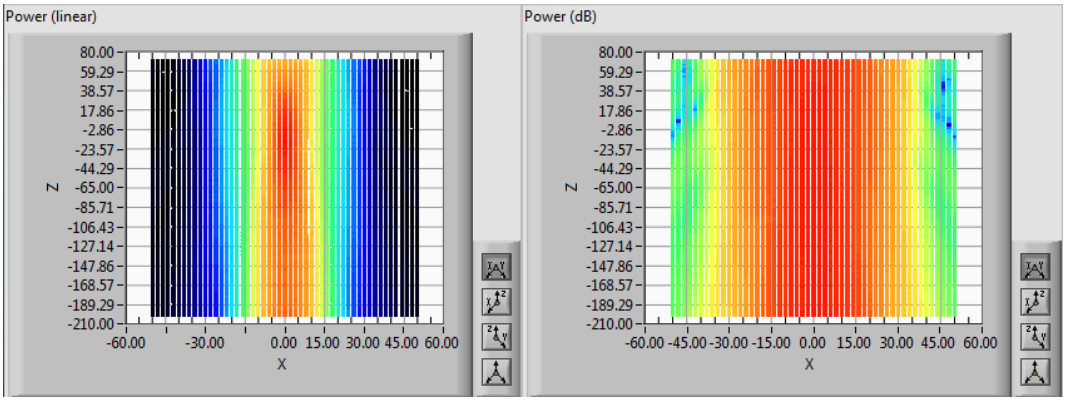


Figure 89: Data from test to determine focus of C type lens. On the left we can see the data for the linearly power scaled from the C type lens. On the right is the lens power in dB. At z = -23.57 mm power is highest maximum and overall power distribution the tightest. This is the best focus position for the lens.

### 4.3.11 C1 uncoated (annealed)

It is important to note that the C lenses suffered from the same distortion during the coating process as that for the M type lens. Therefore, although they were designed with the same mounting screw hole spacing as the M type lens there was still significant movement in the mount due to the shrinking of the lens during coating.

| **Parameter** | **Quantity** | **Unit** |
|---|---|---|
| Distance from horn to lens face (B) | 350±0.4 | mm |
| Distance from receiver to lens face (A) | 369.4±0.4 | mm |
| Distance from centre of lens to rotation point (C) | 18.0±1.2 | mm |
| Length of receiver waveguide | 12.5±0.1 | mm |

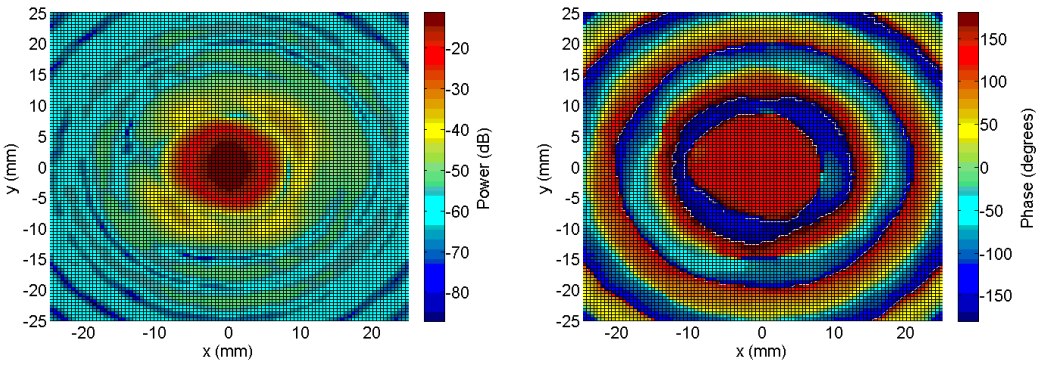


Figure 90: Full range scan of C1 uncoated lens at 0° angle at 100 GHz.

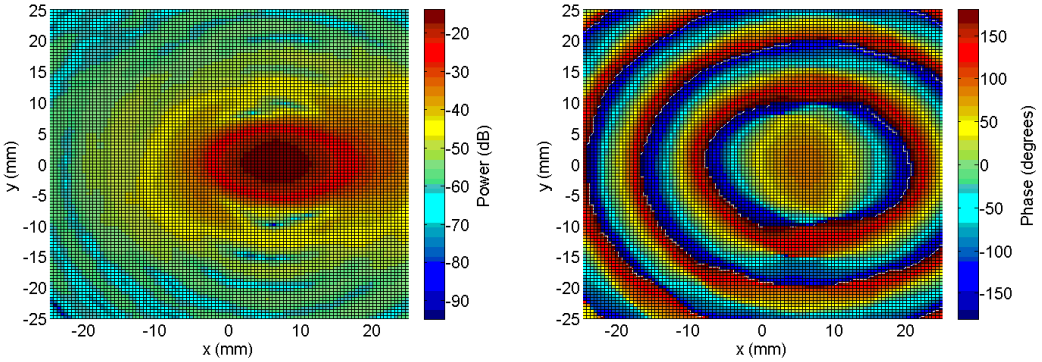


Figure 91: Full range scan of C1 uncoated lens at 10° angle at 100 GHz.

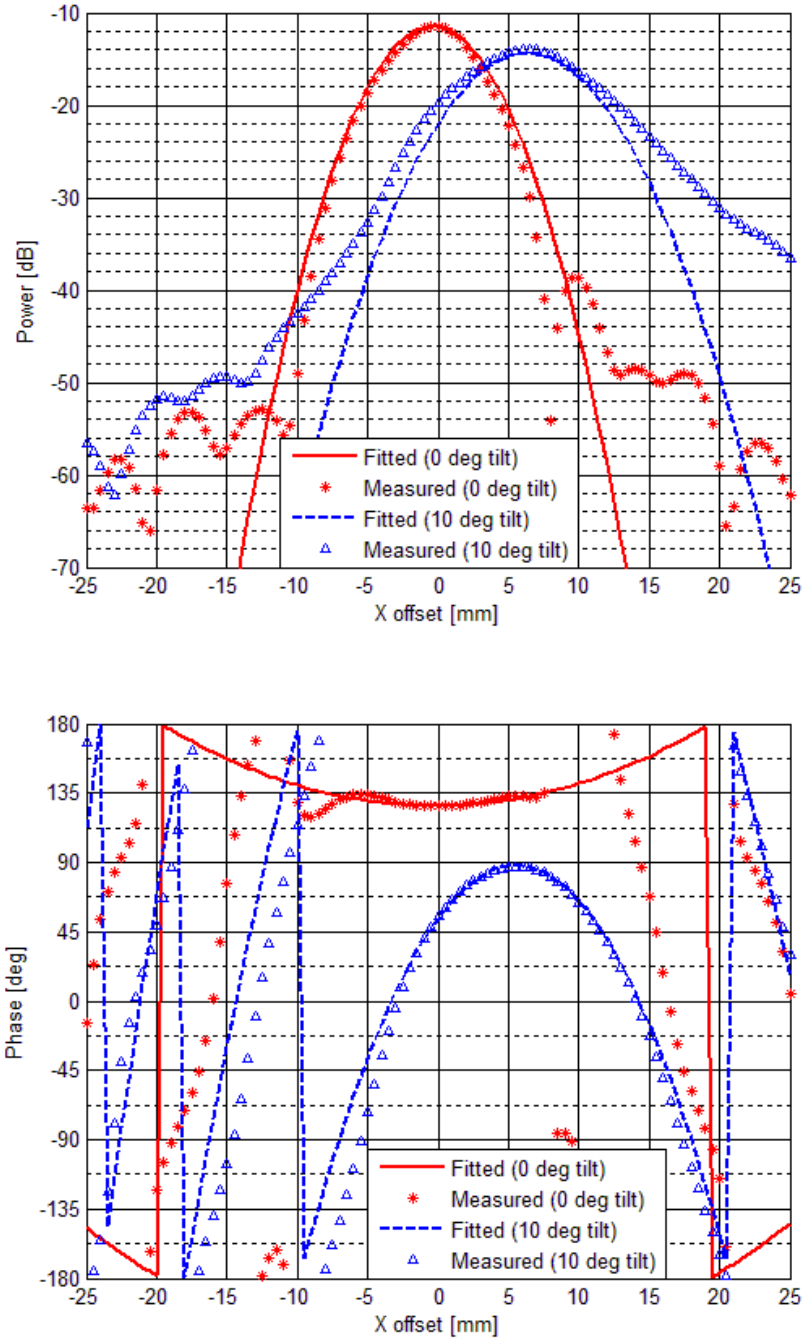


Figure 92: H-plane cuts through the measured field pattern of the C1 uncoated lens at 0° versus 10° tilt.

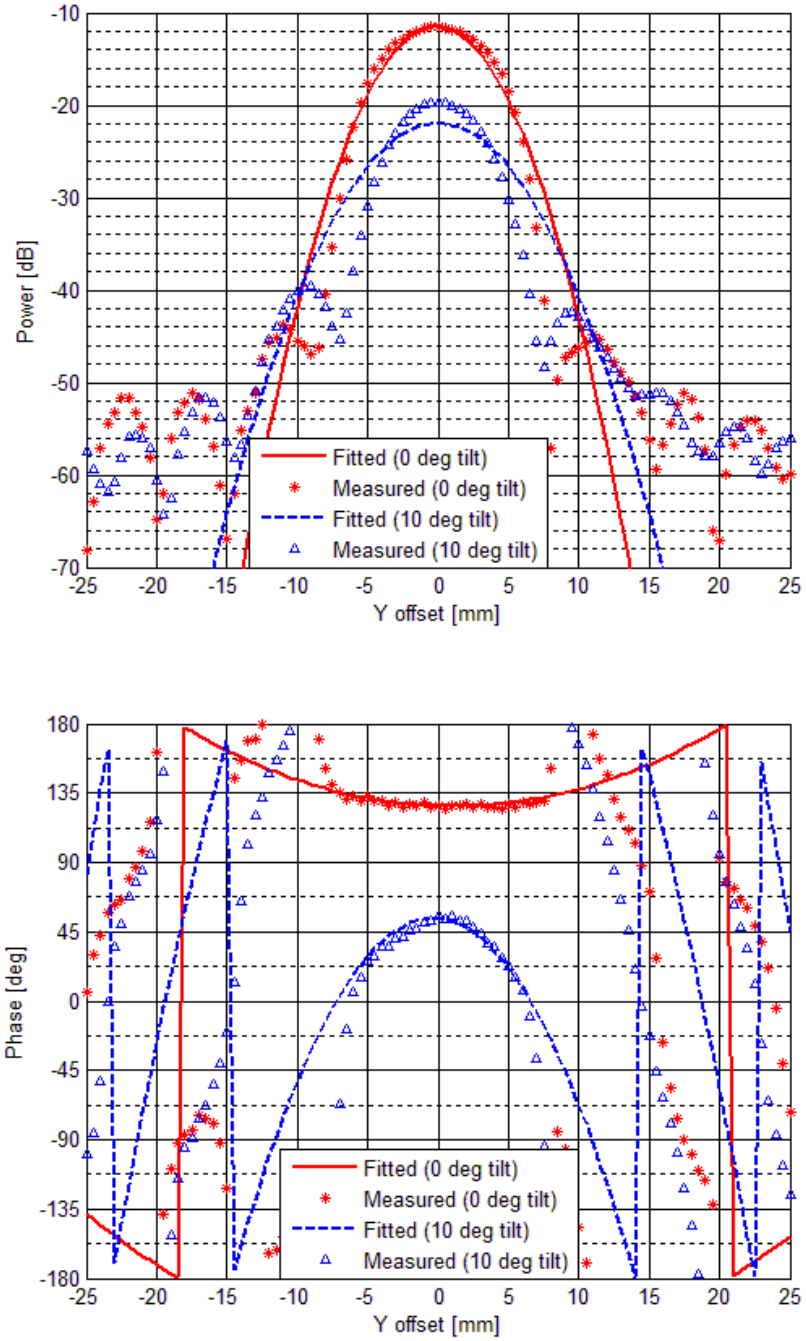


Figure 93: E-plane cuts through the measured field pattern of the C1 uncoated lens at 0° versus 10° tilt.

### 4.3.12 C1 coated (annealed)

| Parameter | Quantity | Unit |
|---|---|---|
| Distance from horn to lens face (B) | 342±0.4 | mm |
| Distance from receiver to lens face (A) | 369.4±0.4 | mm |
| Distance from centre of lens to rotation point (C) | 18.0±1.2 | mm |
| Length of receiver waveguide | 12.5±0.1 | mm |

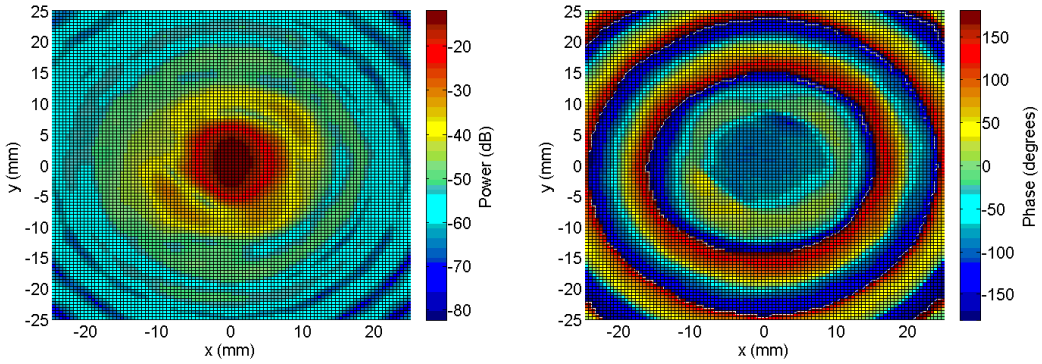


Figure 94: Full range scan of the C1 coated lens at 0° angle at 100 GHz.

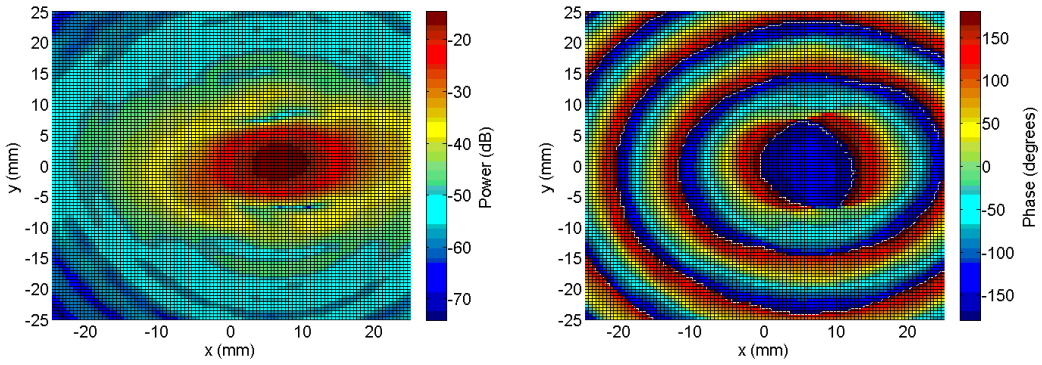


Figure 95: Full range scan of the C1 coated lens at 10° angle at 100 GHz.

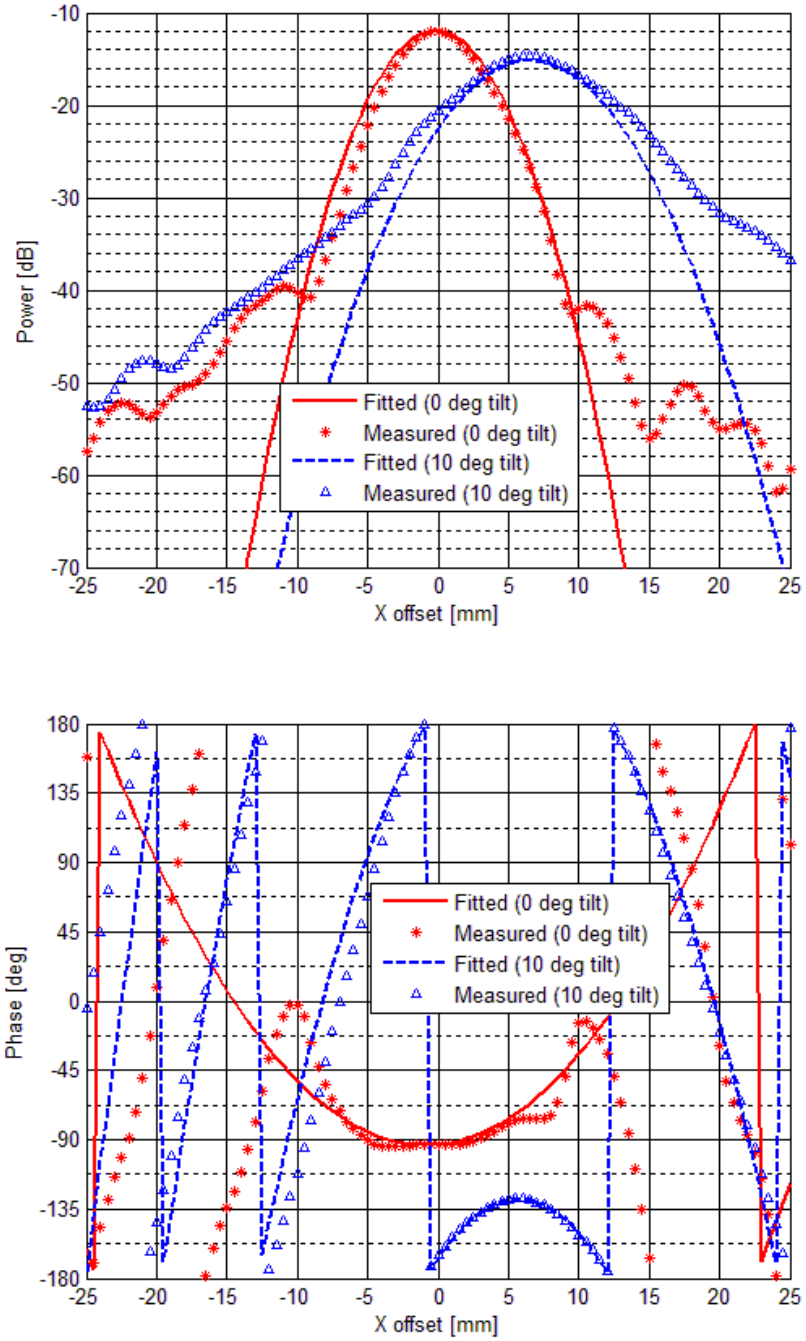


Figure 96: H-plane cuts through the measured field pattern of the C1 coated lens at 0° versus 10° tilt.

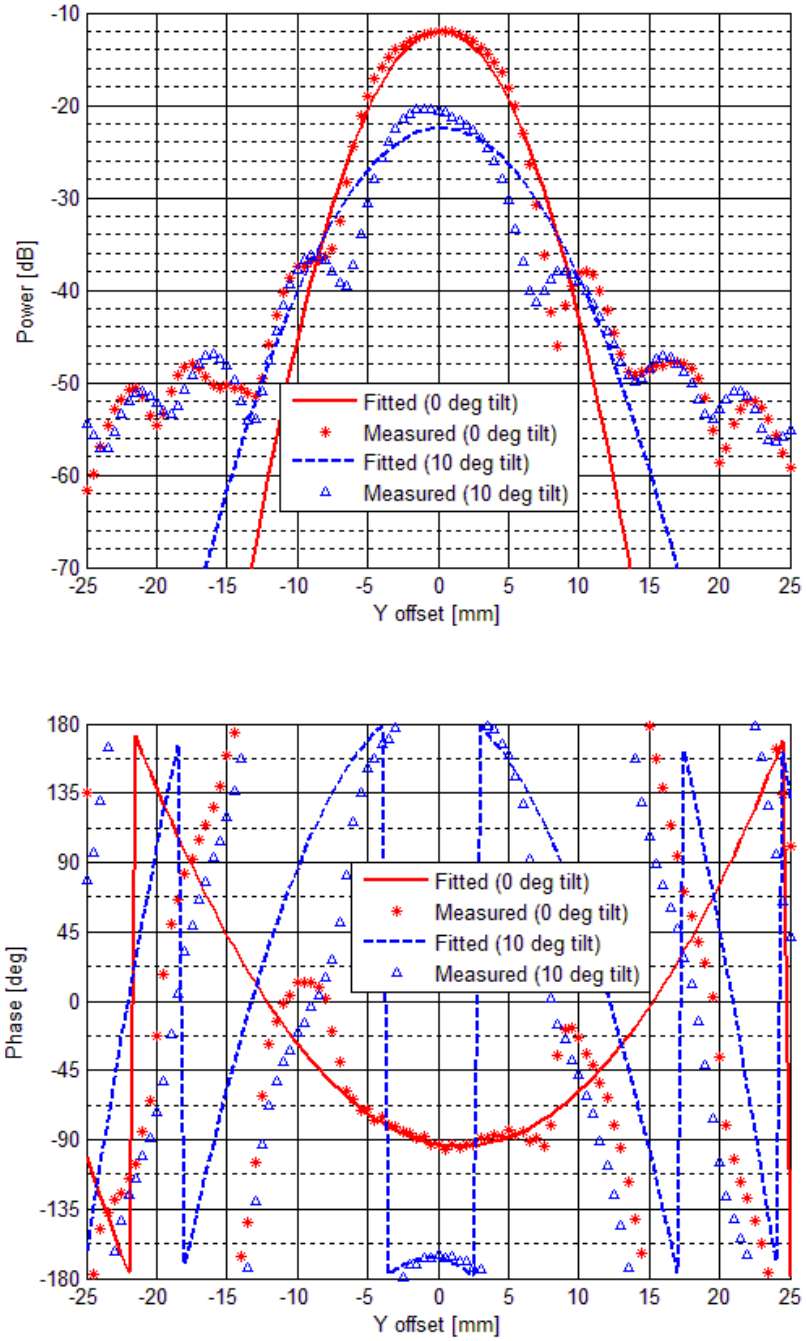


Figure 97: E-plane cuts through the measured field pattern of the C1 coated lens at 0° versus 10° tilt.

## 4.4 TICRA Lens Modelling

TICRA modelled the full set of M2 lens measurements to make a comparison between the measurements and the models. Following are the main results of the simulations he performed and the implications for the measurements.

### 4.4.1 M2 uncoated unannealed

The measurement of this lens was performed at two different distances of the horn from the face of the lens of 372 and 385 mm. The 385 mm value was the distance that gave flattest phase front at the scan plane. The primary comparison between the model and measurement was performed using the phase results as the power is not as sensitive to the change in distances within the system or the properties of the lens as that of the phase. The phase comparison for the 385 mm model and measurement displayed a significant deviation. In order to bring them into agreement two properties were changed separately in the model. These were the refractive index of the lens and the distance from the feed horn to the surface of the lens.

It was found that the refractive index value would need to be 1.515 to bring the model and measurement into agreement from the actual value of 1.51817. This value is considered to be too large due to the extensive measurements that were performed on the lens material to determine the refractive index and there high degree of accuracy. Varying the position from the feed horn to the surface of the lens to 382 mm produced an accurate comparison and could be the source of the deviation. Other possibilities to explain the discrepancies could be errors in the other lens parameters for curvature or thickness of the lens.

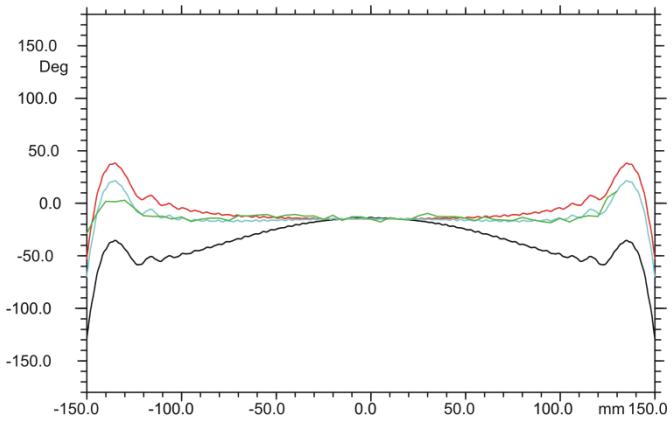


Figure 98: The green line is the measurement data at 100 GHz. The red line is the model performed with the distance at 385 mm. The black line is the model at 372 mm. The cyan line is the model with the adjusted distance of 382 mm which produces the best comparison between the measurement and model.

The model and measurement were compared using the 382 mm distance determined for the distance between the horn and lens with the lens rotated by 10 and 15 degrees with respect to the incident beam. The centre of the rotation stage was determined to be 18 mm from the centre of the lens on the receiver side. With this as the

position for rotation of the lens, the model was performed for the angular offsets of 10 and 15 degrees rotation. There was good agreement between the measurement and model particularly in the centre of the scan range, ± 100 mm, with discrepancies at the edges due to lower power in the measured data.

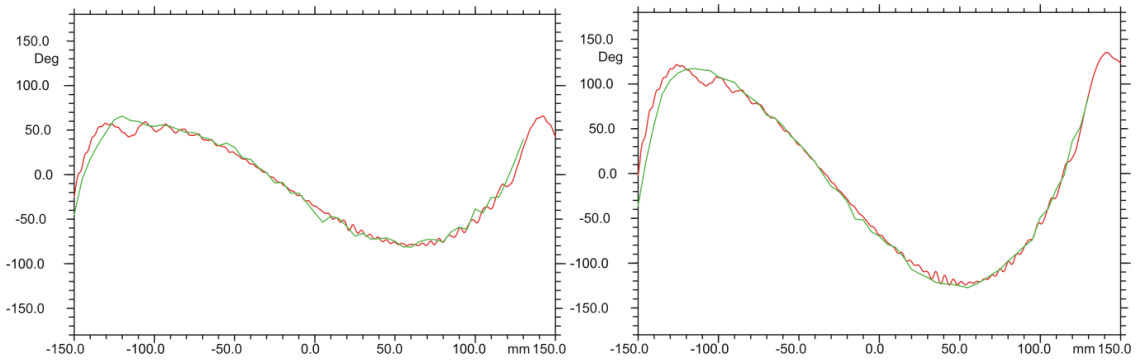


Figure 99: Comparison between the model and measurement for 10 degrees rotation on the left and 15 degrees rotation on the right at 75 GHz. Green lines are the measurement data and red lines are the model.

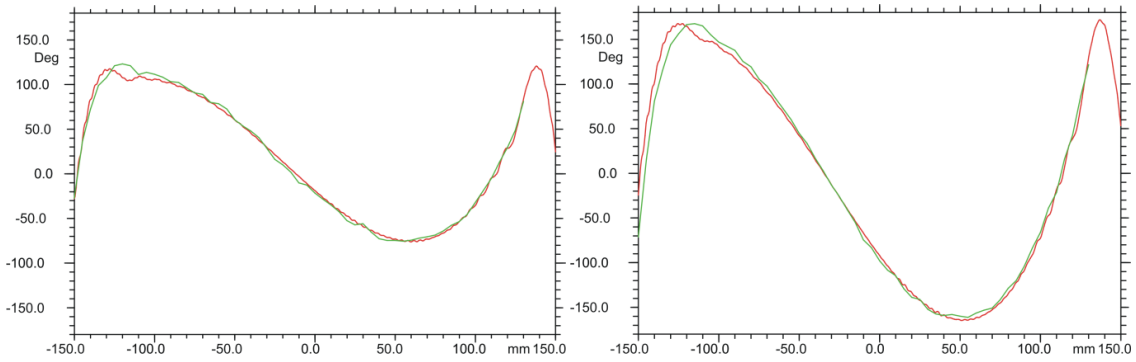


Figure 100: Comparison between the model and measurement for 10 degrees rotation on the left and 15 degrees rotation on the right at 100 GHz. Green lines are the measurement data and red lines are the model.

### 4.4.2 M2 uncoated annealed

The lens was modelled using the distance of 364.4 mm measured for the distance from the feed horn to the lens surface from the measurement system. The comparison showed good agreement with no significant improvement to the comparison with deviation from this value.

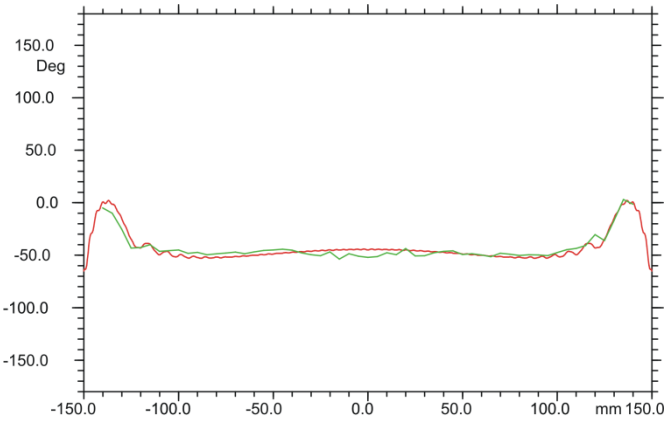


Figure 101: The green line is the measured signal at 100 GHz. The red line is the simulated system with the distance from the feed horn to the lens surface set to 364.4 mm.

The model and measurement were compared with the lens rotated by 10 and 15 degrees with respect to the incident beam. They showed good agreement between measurement and model as with the previous measurements at all frequencies with discrepancies only at the edges of the scan range where the power is low.

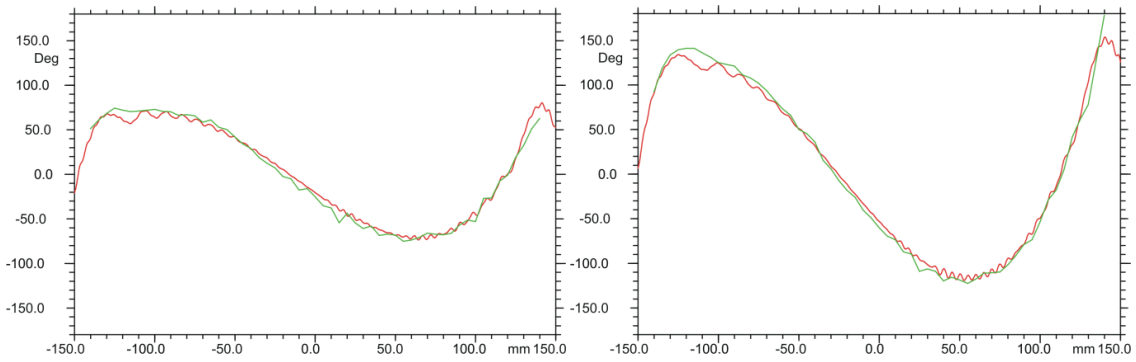


Figure 102: Comparison between the model and measurement for 10 degrees rotation on the left and 15 degrees rotation on the right at 75 GHz. Green lines are the measurement data and red lines are the model.

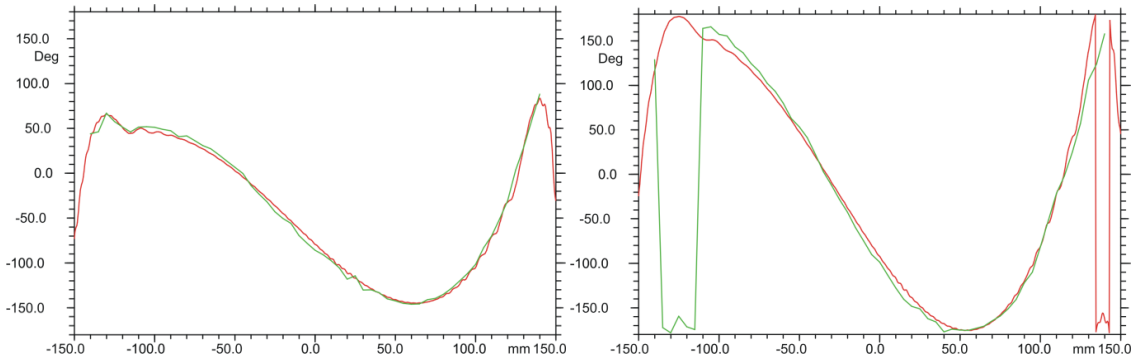


Figure 103: Comparison between the model and measurement for 10 degrees rotation on the left and 15 degrees rotation on the right at 100 GHz. Green lines are the measurement data and red lines are the

model.

### 4.4.3 M2 coated annealed

Due to the coating process affecting the refractive index and shape of the M1 lens, the shape of the M2 coated lens had to be assessed with the model starting with the parameters determined for the M2 uncoated annealed lens. The lens was modelled and the parameters for the radius of curvature and conical constant values for each side of the lens adjusted to determine the best match. It was found that the number 1 side had the same radius of curvature and conical constant values as before coating but the number 2 side required different values to bring the model into agreement with the measurement. This result indicates the annealing process was not sufficient to fully anneal the lens and a more substantial process may be required in future.

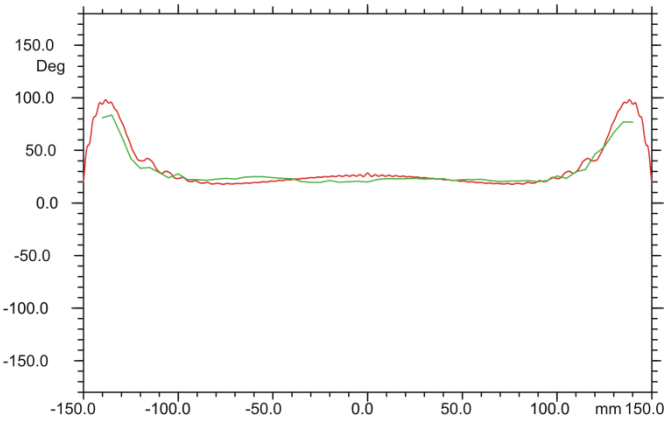


Figure 104: The green line is the measured signal at 100 GHz. The red line is the simulated system with the distance from the feed horn to the lens surface set to 360 mm.

The simulation was performed for the angular offsets of the lens with the incident beam of 10 and 15 degrees showing good agreement between the measurement and model as before.

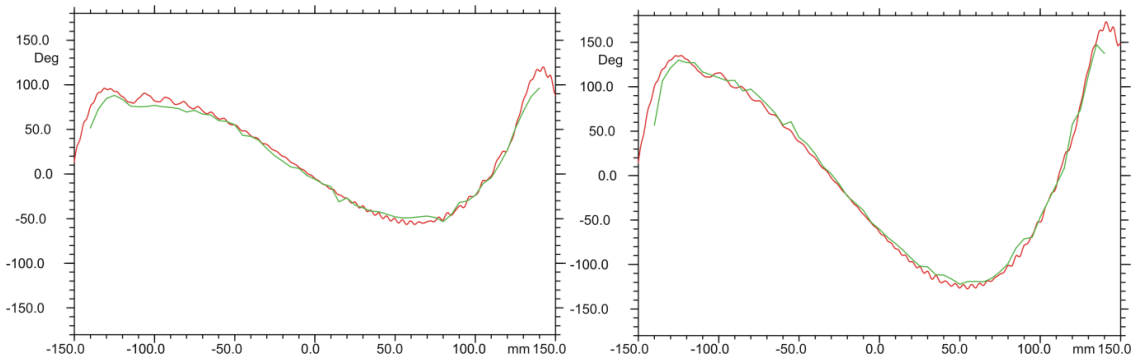


Figure 105: Comparison between the model and measurement for 10 degrees rotation on the left and

15 degrees rotation on the right at 75 GHz. Green lines are the measurement data and red lines are the model.

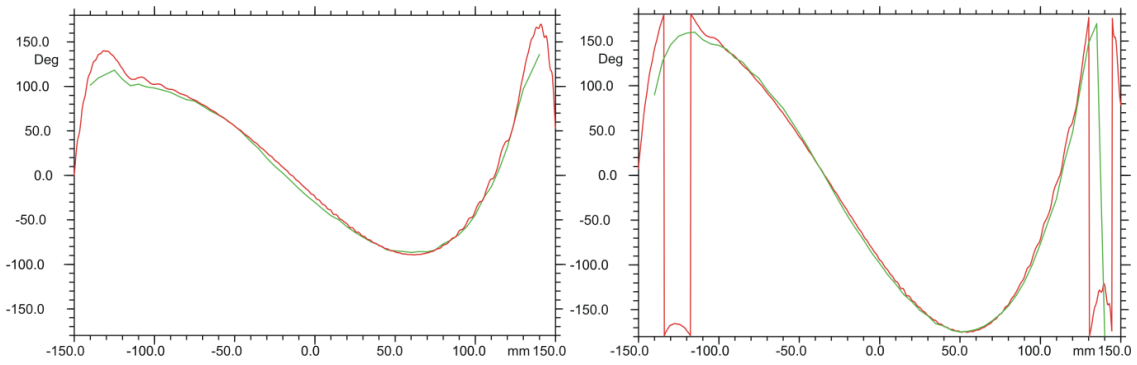


Figure 106: Comparison between the model and measurement for 10 degrees rotation on the left and 15 degrees rotation on the right at 100 GHz. Green lines are the measurement data and red lines are the model.

Overall the measurement and models were in good agreement, with the only major discrepancy between the M2 uncoated unannealed comparison were the distance from the feed horn to the front of the lens was found to have a discrepancy. For that measurement the position of the feed horn had to be set by manually adjusting its position by rotating the axis of the translation stage as the motor in the stage had malfunctioned. This rotation stage was repaired and performed normally for all subsequent measurements.

## 4.5 Improved Measurements

After completing the lens measurements it was determined that new laboratory equipment was required to enable more precise alignment and to ease the setup process. Components were required to increase the accuracy of the horn alignment to the translation stage and the alignment of the translation stage to the scan plane. More general equipment was also purchased to enable better positioning and alignment of system components and devices under test.

Using this new equipment, new alignment steps were created in order to reduce the offsets in the measurement system. This included a new setup for the rotation stage that enabled the offset between the lens centre and the rotation stage centre to be matched to the same point. The old receiver probe absorber was also replaced with a solid piece of absorber. This is due to the discovery of inconsistent results between scans of a system unchanged except for the removing and reapplying of the absorber. The new piece of

absorber allows reproducible application of the absorber to the receiver probe to obtain consistent results.

The use of these new components will be covered followed by the results from the measurements of the M1 and M2 coated lenses using the new alignment procedure.

### 4.5.1 New components

During work in performing the lens measurements some tasks were found to be difficult. It was determined that some new equipment was required for specific tasks and general alignment of system components. The alignment of the horn to translation stage was difficult and therefore new tip tilt stages would be required to ease this task. General alignment of components was also difficult. This included components such as lenses. In particular the height of such components was difficult to match to the height of the emitter and receiver.

Two tip tilt stages were acquired in order to improve the method of alignment of the emitter horn to the translation stage and receiver horn to the scan plane. These stages were mounted under the heads and allowed improved control of their pointing direction. As part of this system upgrade, the mounting plates were also replaced with new aluminium plates on which the heads could be mounted. To enable easier adjustment of the height of components between the heads a set of mounting poles of different heights were purchased along with a series of ring height adjusters. These ring height adjusters were fixed to the mounting poles under the components and used to make small height changes.

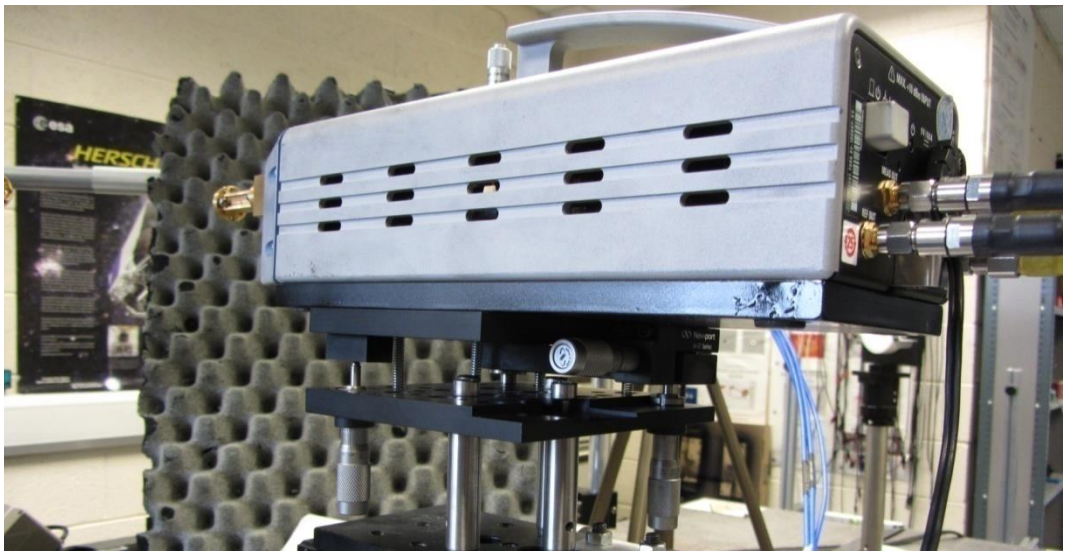

Picture 10: Photo of the receiver head with the new tip tilt stage mounted beneath it.

### 4.5.2 Improved alignment steps

In the previous alignment steps for the lens measurements the emitter horn mounted on the translation stage had to be aligned with respect to the stage's moving axis. To accomplish this, the head's position was changed by rotating it by hand around the mounting pole and by placing shims underneath the back of the head to tilt and tip the head respectively. This method was relatively crude and imprecise, requiring many attempts to obtain the required accuracy. The tip tilt stages allow the required tip and tilt to be calculated and precisely changed reducing the number of required adjustments.

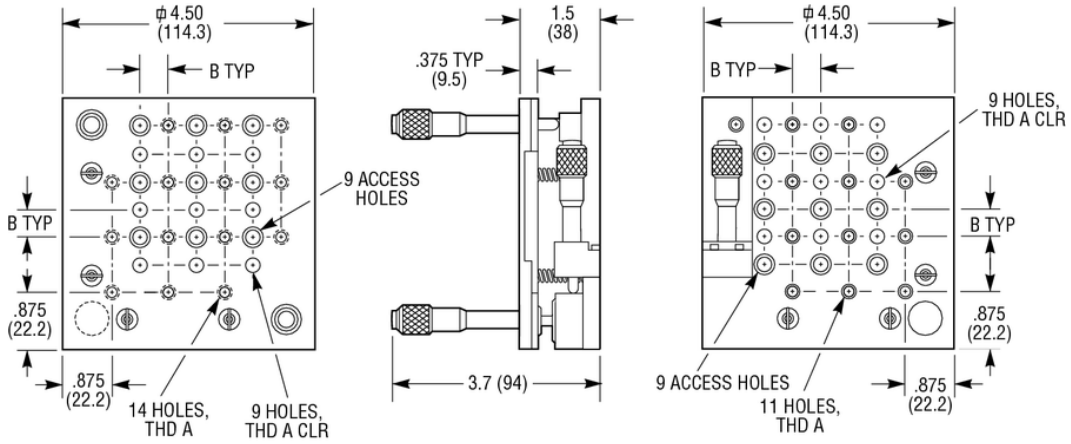


Figure 107: Schematic of the tip tilt stages used for the improved alignment measurements. The main dimension used is the distance from the rotation point to the micrometer screw that causes the rotation. For all three micrometer screws are at a distance of 87.5 mm from the rotation point.

To calculate the required change on the tip tilt stage, the offset angle is measured using the excel spreadsheet shown in Table 13. The position adjustment to be made on the tip tilt stage is then calculated using the distance from the micrometer adjusters to the pivot point of 87.5 mm and calculating the correct amount for adjustment of the micrometer. The remaining angle offset of the translation stage to the scan plane is adjusted by rotating the translation stage itself. Note that this means the $\beta$ angle can be reduced to zero but the $\alpha$ is limited by the agreement between the alignment table surface and scan plane.

Table 13: Excel spreadsheet example showing how the correction for offset of the horn to translation stage and translation stage to scan plane were calculated with the improved alignment setup. The change from the previous method is to the calculation for the correction of the horn, which now uses the tip tilt stage, requiring the distance for the correction to be calculated to change from 300 mm to 87.5 mm.

| Z (mm) | Alpha (deg) | Beta (deg) | X (mm) | Y (mm) |
|---|---|---|---|---|
| 0 | 0.01 | -0.02 | 3.84 | 22.87 |
| -100 | 0.01 | -0.01 | 3.6 | 22.58 |
| -200 | 0.02 | -0.01 | 3.35 | 22.3 |

| | 20140721_Alignment1 | | | |
|---|---|---|---|---|
| Beta Sec | 0.14 | | 87.5 mm | 0.21 mm |
| Alpha Sec | 0.16 | | 87.5 mm | 0.25 mm |
| | | | | |
| Beta Rem | -0.15 | | 600 mm | -1.6 mm |
| Alpha Rem | -0.15 | | 600 mm | -1.6 mm |

The lens alignment to the rotation stage was also improved using the new components. The lens was mounted using its holder on the mounting poles with the new ring height adjusters mounted on the poles underneath the holder. The new ring height adjusters allow better control of the height of the holder and precise small adjustments in height. The poles were mounted on dual axis translation stages that allow the lens to be moved along the *z* and *x* axes, shown in Picture 11. The offset of the lens to rotation stage centre could therefore be corrected by offsetting the lens centre.

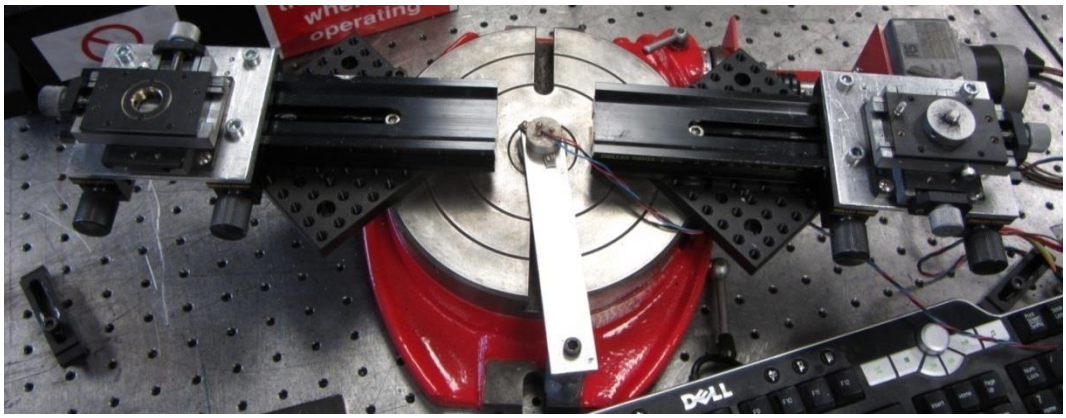


Picture 11: Rotation stage with new mounting system for lens. Allows the lens to be translated from left to right and backwards and forwards so the user can match the centre of rotation of the rotation stage to the centre of the lens.

To calculate and confirm the offset a sequence of photos were used, as previously described, but with a new grid mounted on a metal sheet at the same height as the top of the lens holder. This enabled the distance from the camera to the grid and the tracking points to remain the same. The grid is now also on a solid flat surface rather than the cardboard sheet that was used previously.

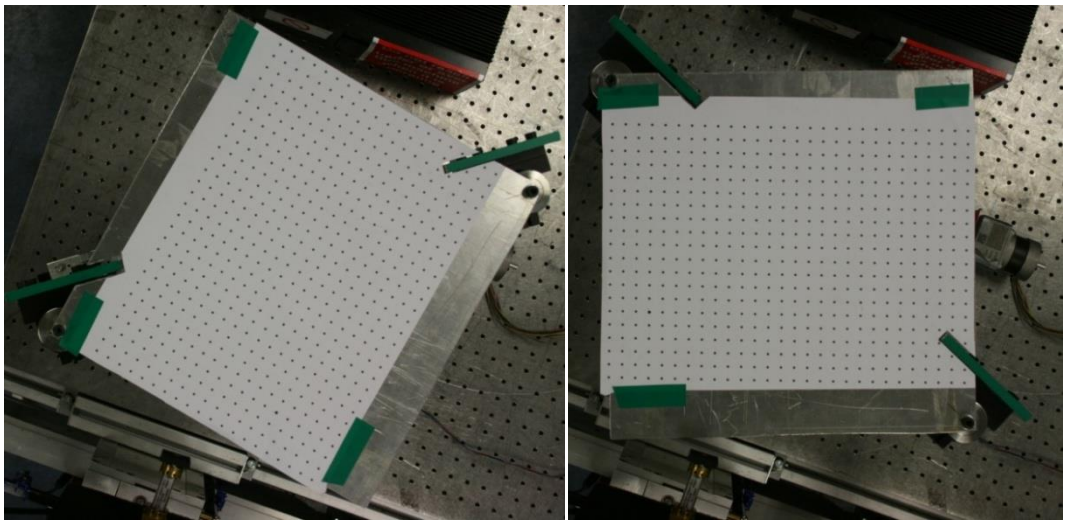

Picture 12: Rotation stage centre offset determination photos. The new grid is mounted on an aluminium sheet mounted at the same level as the top of the holder, edges marked with green tape.

During sequential measurements of the horn with no change to the system it was discovered that the determined $X_{\text{centre}}$ and $Y_{\text{centre}}$ from the Gaussian Fitter program were changing. At first the receiver was thought to be the cause and measurements were made removing and reattaching the receiver probe. The values were changing but with no pattern to the changes. The absorber mounted on the probe was then tested by removing and reapplying it. This was found to be the source of the discrepancies. To rectify this, a piece of solid absorber supplied by Thomas Keating was shaped for use as the new absorber on the probe. The absorber can only be mounted in two ways and as long as it is consistently attached in the same manner it has reproducible results for the $X_{\text{centre}}$ and $Y_{\text{centre}}$ positions.

Table 14 contains the results from testing the absorber. The measurements are ordered with the old absorber first in both the normal orientation (N) and the inverted orientation (I). The measurements for the new absorber are ordered in the same way as for the old absorber. Each receiver was measured at the 0 and -200 mm point of the translation stage, z-axis. Both N and I measurements for the old and new absorber were performed twice, given the labels 1 and 2 to distinguish between each measurement.

Between N and I, 1 and 2, for the old absorber we can see significant change in the *X* and *Y* centre positions. If the absorber has no effect on the results, the parameters should be the same for any piece of absorber with the same distance, *D*, parameter value. This is not the case for the old absorber which shows large changes in parameters, *X* and *Y* centre, and inconsistent results for measurements made with the absorber in the same orientation, only having been removed and reattached. Consistent results are therefore impossible with the old absorber type. The new absorber shows more stable results between its measurements with reproducible results after removing and reapplying the absorber while maintaining the same orientation.

Table 14: Results for testing the old and new absorber for mounting to the front of the probe. Each piece of absorber is completed in normal orientation (N) and inverted orientation (I). They are also completed at two distances of 0 and -200 mm on the translation stage.

| Measurement | *D* (mm) | *W* [mm] | *R* [mm] | $W_0$ [mm] | *Z* [mm] | $X_{centre}$ | $Y_{centre}$ | $\alpha$ | $\beta$ |
|---|---|---|---|---|---|---|---|---|---|
| Old N1 | 0 | 49.42 | 227.97 | 4.38 | 226.18 | -3.09 | 0.16 | -0.45 | -0.12 |
| | -200 | 94.46 | 426.62 | 4.31 | 425.73 | -3.32 | 1.17 | -0.5 | -0.18 |
| Old N2 | 0 | 49.83 | 228.78 | 4.36 | 227.02 | -5.03 | -0.14 | -0.4 | -0.62 |
| | -200 | 95.18 | 427.43 | 4.28 | 426.57 | -7.19 | 0.01 | -0.37 | -0.7 |
| Old I1 | 0 | 49.55 | 228.55 | 4.38 | 226.76 | -3.09 | -0.42 | -0.3 | -0.13 |
| | -200 | 94.56 | 425.57 | 4.29 | 424.7 | -2.98 | -0.16 | -0.33 | -0.13 |
| Old I2 | 0 | 50.39 | 229.28 | 4.33 | 227.59 | -3.11 | 0.6 | -0.55 | -0.1 |
| | -200 | 96.2 | 428.21 | 4.24 | 427.38 | -3.09 | 2.3 | -0.65 | -0.13 |
| New N1 | 0 | 49.61 | 226.52 | 4.34 | 224.79 | -3.52 | -0.01 | -0.34 | -0.23 |
| | -200 | 96.32 | 428.28 | 4.24 | 427.45 | -3.99 | 0.35 | -0.33 | -0.27 |
| New N2 | 0 | 50.46 | 229.3 | 4.32 | 227.62 | -3.48 | -0.36 | -0.28 | -0.21 |
| | -200 | 96.99 | 428.2 | 4.21 | 427.4 | -3.88 | 0.38 | -0.36 | -0.25 |
| New I1 | 0 | 49.55 | 226.52 | 4.35 | 224.78 | -3.19 | 0.62 | -0.51 | -0.16 |
| | -200 | 96.63 | 428.16 | 4.22 | 427.34 | -3.28 | 1.72 | -0.51 | -0.18 |
| New I2 | 0 | 50.42 | 229.16 | 4.32 | 227.48 | -3.19 | 0.3 | -0.46 | -0.15 |
| | -200 | 96.34 | 428.35 | 4.24 | 427.52 | -3.44 | 1.57 | -0.53 | -0.19 |

### 4.5.3 Repeated lens measurements

With the new alignment steps the measurements were completed for the M1 and M2 coated lenses. The alignment was completed using the previous alignment procedure and the two new stages outlined above. The list of the alignment steps is shown below:

- Alignment table and scanner levelled

- Translation stage and emitter horn geometrically aligned with table edge
- Emitter horn and translation stage aligned to scan plane using new tip tilt stages as outlined in section 4.5.2.
- New step to reduce the offset between the centre of rotation of the rotation stage and the centre of the lens. Method described in section 4.5.2. This step was not completed in the preliminary measurements as the offset was fixed and could not be minimised.
- Alignment of the rotation stage angularly to the emitter horn.
- Alignment of the aperture centre with incident beam at the rotation stage.

The flat phase position of the lens is then found using the same technique as described previously. Using the two new alignment techniques described earlier the offset of the horn to translation stage and scan plane is minimised and the offset of the lens centre to the rotation stage centre are adjusted so that they coincide. The offset of the horn to the translation stage can be minimised but the offset between the translation stage and the scan plane can only be minimised for the angle offset for rotation around the *y*-axis. Due to the translation stage sitting on the alignment table the offset for rotation around the *x*-axis cannot be corrected and is fixed at the offset value between the table and the scan plane.

### 4.5.4 Rotation stage centre offset

The rotation stage centre offset with respect to the centre of the lens is minimised before measurements. The centre point is at a distance half the rim thickness plus the thickness of the coating layer from the holder edge. The thickness of the lens rim is 10 mm and the thickness of the coating layer 0.64 mm. We therefore want the centre point to be 5.64 mm from the edge of the lens holder. This value didn't change due to the annealing as the effect on the rim of the lens was not significant. The points we choose to track are the four corners from the rectangular section marked in green on both sides of the lens holder seen in Picture 12. Two of these points are used in the Rotation Axis Measurement program in order to form a line matching the edge of the lens holder. We can then use this as a reference to measure the distance perpendicularly from this line to the centre of rotation and parallel along this line to the centre of rotation.

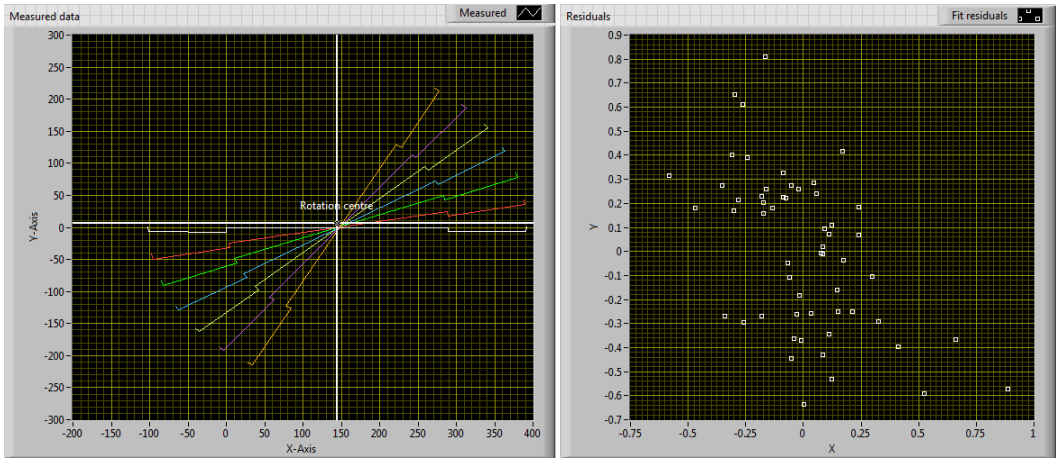


Figure 108: Image from the Rotation Axis Measurement program. The residual offsets in the point's positions can be seen on the left. On the right is a depiction of the points and the location of the Rotation Centre. The *x* and *y* axes are displayed in units of millimetres.

After several iterations the rotation centre was found to be 5.2 ± 0.85 mm from the holder edge and displaced 0.6 ± 0.8 mm along it. After minimising the offset between the centre of rotation and the centre of the lens the remaining distance is 0.72 ± 1.2 mm. This value was taken as accurate, as the residuals in the positions of the points for the fit plus the maximum error in position of the points given by the Vision Assistant program.

### 4.5.5 M1 coated

The M1 coated measurement was repeated using the new system components for alignment of the emitter and receiver heads. The new tip tilt stages allowed increased accuracy in aligning the emitter horn to the translation stage. The alignment was also completed in one step compared to the iterative process previously employed to achieve the required alignment accuracy using the previous method.

Table 15: System distances for the M1 coated lens with improved alignment.

| **Parameter** | **Quantity** | **Unit** |
|---|---|---|
| Distance from horn to lens face (B) | 386±0.4 | mm |
| Distance from receiver to lens face (A) | 75±0.4 | mm |
| Distance from centre of lens to rotation point (C) | 0.72±1.2 | mm |
| Length of receiver waveguide | 12.5±0.1 | mm |

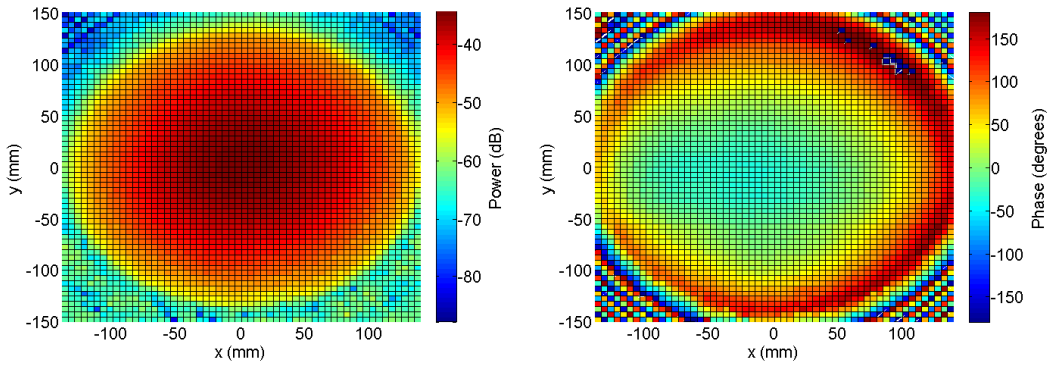


Figure 109: Plot of measured full range scan of the M1 coated lens with improved alignment at 100 GHz and 0 degrees rotation.

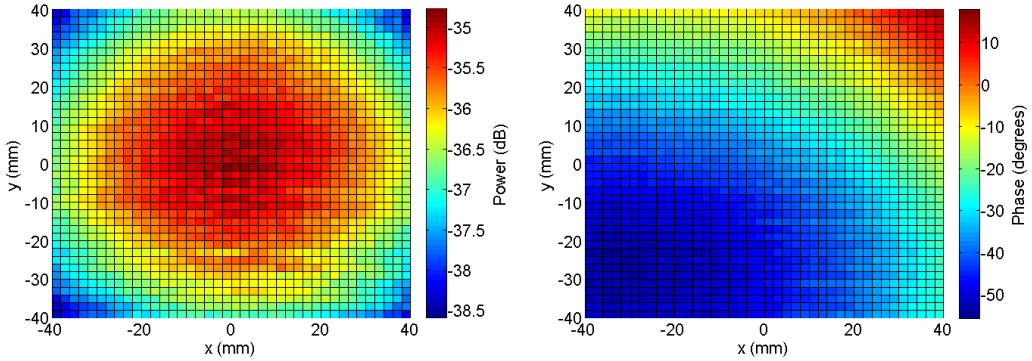


Figure 110: High resolution centre scan of the M1 coated lens at 100 GHz.

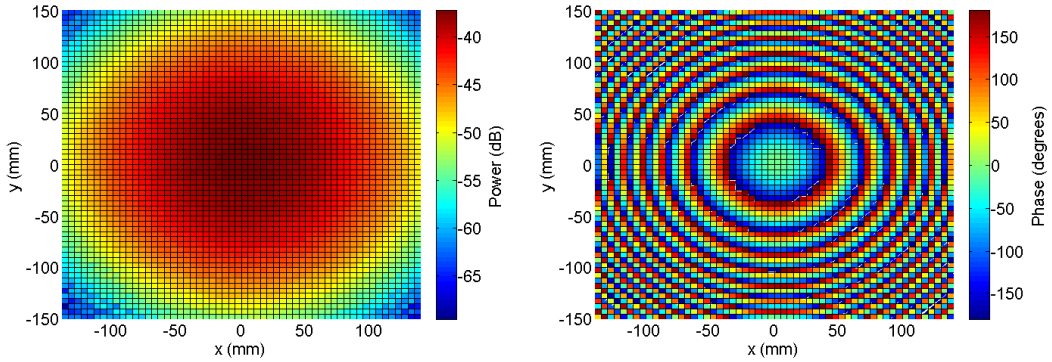


Figure 111: Plot of feed horn measurement for the M1 coated lens at 100 GHz.

### 4.5.6 M2 coated

The M2 coated lens was retested with the new measurement setup.

Table 16: System distances in M2 coated lens with improved alignment.

| Parameter | Quantity | Unit |
|---|---|---|
| Distance from horn to lens face (B) | 364.5±0.4 | mm |
| Distance from receiver to lens face (A) | 83.6±0.4 | mm |
| Distance from centre of lens to rotation point (C) | 0.72±1.2 | mm |
| Length of receiver waveguide | 12.5±0.1 | mm |

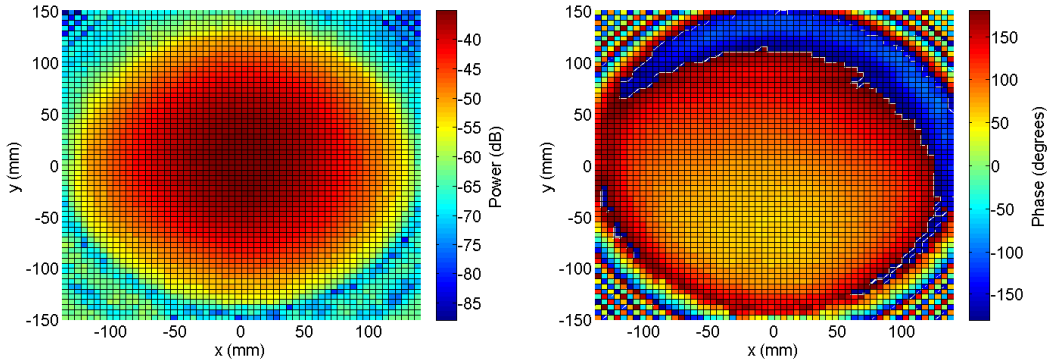


Figure 112: Power and phase at 100 GHz for the M2 coated lens using improved alignment steps.

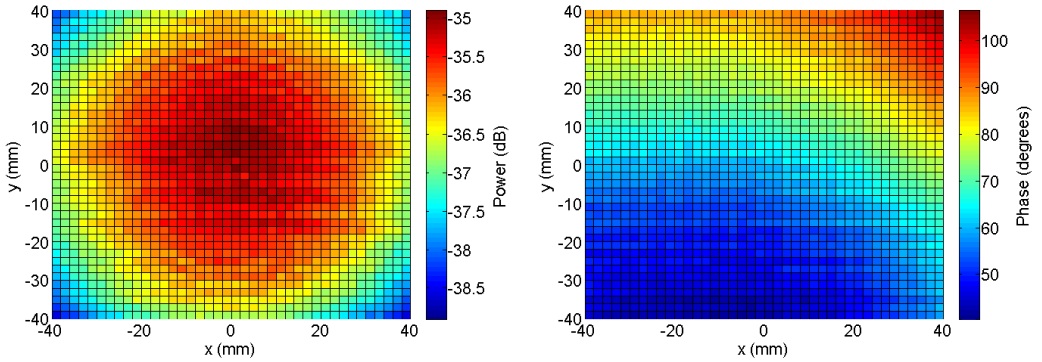


Figure 113: Centre high resolution scan of the M2 coated lens after improved alignment.

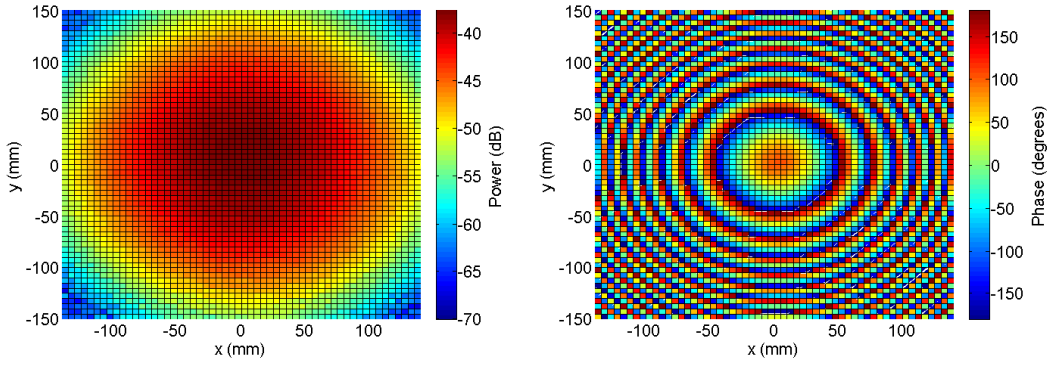


Figure 114: Feed horn scan for the M2 coated lens measurement with improved alignment.

## 4.6 Conclusion

The aim of the measurement campaign described in this chapter was to provide data in order to verify the performance of the lenses based on their design and for comparison to the computational models developed by TICRA. The initial results in conjunction with the models performed by TICRA brought to light the annealing issue in the manufacturing process. This was the first success of the measurements and proved that the measurement alignment process was robust and fit for purpose. Due to secondary annealing the lenses had shrunk during the coating process. This added inaccuracies in the mounting of the lenses as the holes in the edge of the lens used to mount them had to be expanded. The lens could no longer therefore be mounted precisely and could be inadvertently displaced both horizontally and vertically on the mounting screws.

The comparison between the measurements of the coated and uncoated M1 lenses validated the performance of the anti-reflection coating. The standing waves seen in the high resolution scans of the centre of the lens were reduced when the coating was applied, with best performance at 100 GHz. Further measurements were completed for the M2 lens and subsequently for the C1 and C2 lenses. Following the completion of the measurements the measurement system was upgraded with new components in order to increase the ease and accuracy of the alignment process and to reduce the time to complete it. This resulted in the alignment of the feed horn to the scan plane being completed in one iteration as opposed to the sequence of iterations that were required with the previous method. The new mount created for the lens allowed for the centre of rotation of the rotation stage to be aligned with the centre of the lens.

Following these upgrades to the alignment system the coated M1 and M2 lenses were re-measured to assess the improvements to the measurement system. The results showed only small improvement in the overall accuracy of the lens measurements but enabled faster alignment of the system before introducing the lens and will make the subsequent modelling easier without an offset between the rotation axis of the rotation stage and the centre of the lens.

# Chapter 5: Computational Modelling

## 5.1 Introduction

The final part of the work was to use the in-house modelling software, MODAL, to simulate the measurement system for each lens measurement. Modelling the system enables the accuracy of the measurement system setup to be assessed through direct comparison. The feed horn measurements taken for each lens are modelled first in order to verify that the offsets determined for the feed horn are accurate. After confirming the feed horn is aligned accurately in the model the lenses can be simulated. With the feed horn positioned correctly, any inconsistencies between the measurement and model should now be due to incorrect positioning of the lens or distortion of its shape. With the lens positioned in the location determined from measurements, changes can be made to the position and angle of the lens to determine the cause of discrepancies between measured and modelled beam patterns.

## 5.2 Computational Model of Measurement System

In order to simulate the lens system an in-house software program called 'Maynooth Optical Design and Analysis Laboratory' (MODAL) was used. MODAL uses a combination of physical optics (PO) and Gaussian beam mode analysis to simulate the optical system. The simulations run by MODAL utilise Maynooth Universy's 106-core computer cluster to enable simulations to be completed in a reasonable time. The software allows the user to build up a system of components and visualise the setup in a 3D viewer. The user can reference the position of components to a global reference grid or with respect to local frames as specified by the user. The system also allows use of geometry files in order to generate models of waveguide components in the system. This is used in particular to simulate the emitter horn and receiver probe.

To create a simulation we start with only the global reference frame defined. The first object specified is the source field for the system. The emitter horn is then defined through the use of a geometry file written to describe the Thomas Keating horn profile. The file defines the radius and thickness of each of the corrugated horns stepped

sections. A 100 GHz beam source is defined to feed the emitter horn. The WR-10 waveguide receiver probe profile is then simulated and placed at the centre of the scan plane at a specified distance in front of the feed horn. The lens profile is then input into the program. Two curved surfaces representing the sides of the lenses are defined and placed a distance away from each other equal to the thickness of the centre of the lens that was measured by Cardiff University. The refractive index of the lens is specified and the region bounded by the two sides of the lens given this refractive index. It should be noted that no loss due to absorption by the body of the lens is simulated. The components can then be rotated and offset relative to the global and user-defined local reference frames as required.

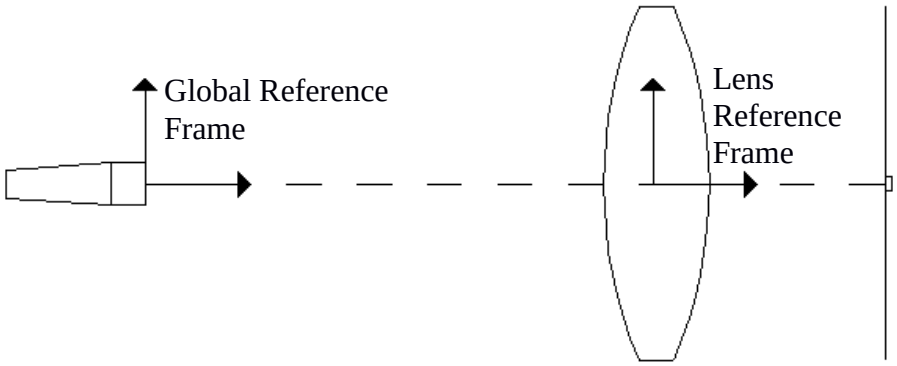


In order to approximate the measurement system as closely as possible, any positional and angular offsets in the measurement system are input into the model. This allows for direct comparison between the simulation and the measurement. A local reference frame is created for the two sides of the lens to be linked to. This frame position is then set to match that of the rotation centre of the rotation stage. This can be used to simulate the lens rotation on the rotation stage. The lens can also be displaced along the *x* or *y* axes to simulate an offset in the centre position of the lens. This enables the user to adjust the position of the lens to match the simulation to the measurement system as will be discussed in the following sections. Parameters are created in the simulation and linked to the offsets. The parameters can be changed in a batch run script to enable multiple runs of the simulation with different offsets to be completed without further user input.

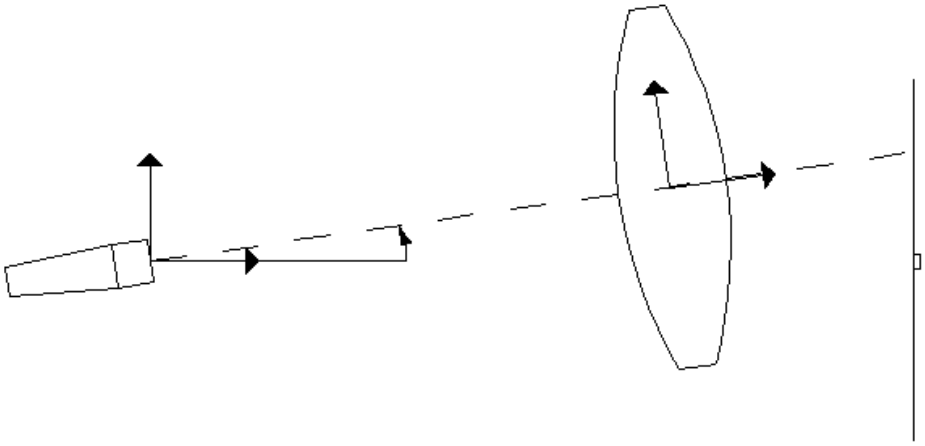

Figure 115: MODAL simulation setup with the horn rotated about the global reference frame centred at the front of the feed horn. The lens is also rotated around the global reference frame to align with the beam.

All these offsets are shown in a 3D image viewer in MODAL. This allows the user to vary the offsets and ensure the simulation is setup correctly after rotating or displacing objects in the same way as in the measurement system.

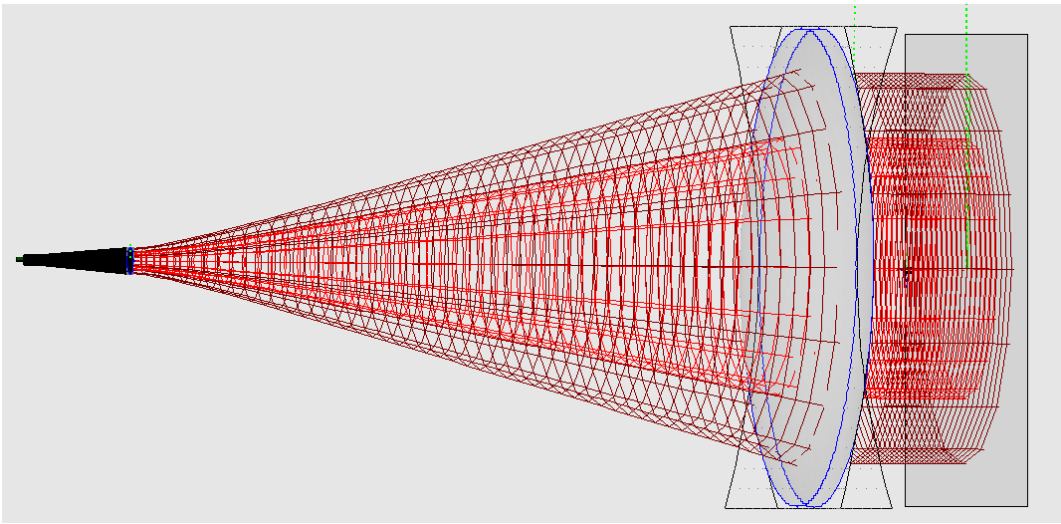

Figure 116: Screenshot of the simulation setup view provided in MODAL.

## 5.3 Comparison to MODAL Simulations

To accurately model the measurement system the model must be setup with the same feed horn and receiver probe position. This is achieved by first setting up the computational model with just the feed horn and receiver probe in place. The offsets for the feed horn angle with respect to the scan plane, as well as the offset of the centre position of the receiver probe relative to the preceding elements of the optical system on

the scan plane, are specified. To calculate these offsets, the feed horn reference measurements were provided as inputs to the Gaussian Fitter program. The offsets of the feed horn, relative to the scan plane for each distance of the feed horn on the z-axis translation stage are assessed separately. These offsets were used to calculate the relative position of the scan plane centre with respect to the feed horn, based on the angle offset of the feed horn to the scan plane and the centre offset of the scan plane provided by the Gaussian Fitter program.

The $\alpha$ and $\beta$ angles calculated by the Gaussian Fitter program are used to specify the orientation of the horn relative to the scan plane. The lens orientation is offset to match the horn.

Table 17: Offsets calculated for the MODAL model from the measurement feed horn measurements. The first row of values in the table represent the distances between components within the measurement system. B Offset is the distance the translation stage had been moved from the zero position. B Offset cal factor is a correction factor B Offset must be multiplied by due to a motor calibration error present in the measurements of the M1 and M2 uncoated (unannealed) lenses. The second row of values are the feed horn angle and centre position offsets relative to the scan plane as determined by the Gaussian Fitter program. The third row of values are the predicted position for the beam centre if the angle offsets are applied and the scan plane is otherwise perfectly centred with the horn. The fourth row of values are the determined distances to displace the scan plane in the simulation in order to replicate the measurement system.

***M1 Coated Improved***

***System distances for analysis***

| B [mm] | B Offset [mm] | B offset Cal factor | A [mm] | L [mm] | L2S [mm] | Total [mm] |
|---|---|---|---|---|---|---|
| 386.0 | 0.0 | 1 | 75.0 | 59.9 | 386.0 | 520.9 |

***Analysis at lens alignment frequency (100 GHz)***

| $\alpha$ [deg] | $\beta$ [deg] | $X_0$ [mm] | $Y_0$ [mm] |
|---|---|---|---|
| -0.12 | 0.00 | 0.16 | 1.03 |

***Predicted from 100 GHz fit with no motion control offsets***

| $X_{0Pred}$ [mm] | $Y_{0Pred}$ [mm] |
|---|---|
| 0.00 | 1.09 |

***Deduced motion control system offsets (constant)***

| $\Delta X_0$ [mm] | $\Delta Y_0$ [mm] |
|---|---|
| -0.16 | 0.06 |

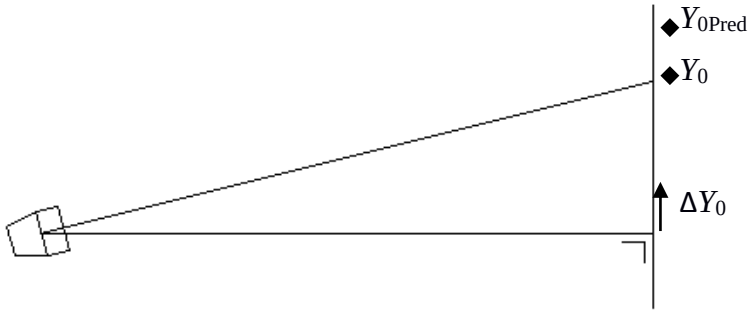


Figure 117: The position of the centre of the beam, $Y_0$, as provided by the Gaussian Fitter program. The predicted position from the offset angle, $Y_{0Pred,}$ and the distance that the centre of the scan plane is shifted along the *y*-axis $\Delta Y_{0,}$ on the global frame of reference.

Table 17 shows the offsets used to model the measurement system. The system distances used for the analysis are the same as shown earlier in Figure 46. For calculation of the scan plane centre offsets $\Delta X_0$ and $\Delta Y_0$ we use the total system distance and the angles $\alpha$ and $\beta$. $\Delta X_0 = X_{0Pred}$-$X_0$, where $X_{0Pred}$ is the offset deduced from the total angle offset of the scan plane with respect to the beam. In this particular case $\beta$ is zero, therefore $X_{0Pred}$ is zero. The same calculation is completed for the *y*-axis offset but due to $\alpha$ being non zero the $Y_{0Pred}$ is non zero. The values $\Delta X_0$ and $\Delta Y_0$ are used to offset the centre of the scan plane in order to accurately simulate the measurement system.

Next the local frames for each object in the system must be changed to match that of the measurement system. In the simulation the default axis system for the emitter horn is such that the *z*-axis increases towards the scan plane. In order for the orientation of the $\alpha$ and $\beta$ angles for the offset of the horn to conform to the measurement, the scan plane must be rotated about the *x*-axis 180 degrees. This is because the orientation of the *y*-axis of the scanner is inverted in the measurement system. The directions of the *y* and *z* axes of the scan plane are now opposite to the horn but the *x*-axis remains in the same direction. The frame of the lens is also rotated 180 degrees around the *x*-axis to match the scan plane axes orientation.

Parameters were then created in the model to offset the component positions by altering the reference frames in the system to match the measurement setup. The $\alpha$ and $\beta$ parameters in the model match the measurement $\alpha$ and $\beta$ parameters rotating the horn with respect to the scan plane. The rotation is performed around the centre front of the horn. Angles $\alpha_{Ref}$ and $\beta_{Ref}$ were defined in order to correctly orient the lens. These values are the same as the $\alpha$ and $\beta$ and angle the lens to be at the same angle with

respect to the scan plane as the horn is. The centre of the emitter horn is kept in line with the centre of the lens by rotating both the horn and lens about the same reference axis.

The scan plane is set to the correct distance relative to the global frame of reference, ie. with its centre shifted a distance ($\Delta X_0$, $\Delta Y_0$).

### 5.3.1 Simulating the feed horn

The first simulation compares the feed horn measurement to the feed horn model. Separate lens simulations were performed to test each lens:

- M1 uncoated (unannealed)
- M2 uncoated (unannealed)
- M2 uncoated (annealed)
- M1 coated (annealed)
- M2 coated (annealed)
- M1 coated (annealed) Improved Alignment
- M2 coated (annealed) Improved Alignment

For each simulation the relevant offset values for the feed horn and scan plane were inserted and the simulation run. After each simulation was completed the file was converted from the MODAL data file format to the measurement file format. This was done to enable the file to be directly input into the Gaussian Fitter program. If the results of the Gaussian Fitter program match the measurement we can say that the offsets are implemented correctly in the simulated system.

### 5.3.2 M1 uncoated (unannealed)

The system offsets for the M1 uncoated (unannealed) are given in the table Table 18. These values were input into the simulation and then the simulation was performed to measure the feed horn pattern.

Table 18: M1 uncoated (unannealed)

***System distances for analysis***

| B [mm] | B Offset [mm] | B offset Cal factor | A [mm] | L [mm] | L2S [mm] | Total [mm] |
|---|---|---|---|---|---|---|
| 372.0 | -13.4 | 0.9765625 | 71.0 | 56.7 | 385.1 | 512.8 |

***Analysis at lens alignment frequency (100 GHz)***

| $\alpha$ [deg] | $\beta$ [deg] | $X_0$ [mm] | $Y_0$ [mm] |
|---|---|---|---|
| 0.06 | 0.01 | 1.97 | -1.17 |

***Predicted from 100 GHz fit with no motion control offsets***

| $X_{0Pred}$ [mm] | $Y_{0Pred}$ [mm] |
|---|---|
| 0.09 | -0.54 |

***Deduced motion control system offsets (constant)***

| $\Delta X_0$ [mm] | $\Delta Y_0$ [mm] |
|---|---|
| -1.88 | 0.63 |

The simulation data was then input into the Gaussian Fitter program and the fit performed to obtain agreement between the model and measurement. Table 19 shows the values obtained from the Gaussian Fitter program with the simulated data as the input. These values when compared to those in the table above show $\alpha$ was 0.06° for both the model and simulation, $\beta$ was 0.01° for the measurement and 0° in the simulation fit, $X_{centre}$ from simulated data was 1.85 mm compared to 1.97 mm for measured data and $Y_{centre}$ was -1.17 mm matching $Y_0$ from measured data. This means that good agreement between the model and the measurement were achieved and that the offsets in the model appeared to be input correctly and with the correct orientation with respect to the measured system.

Table 19: Table of the $\alpha$, $\beta$, $X_{centre}$ and $Y_{centre}$ values obtained from the Gaussian Fitter program for the modelled feed horn beam pattern of the M1 uncoated lens setup.

| $\alpha$ (deg) | $\beta$ (deg) | $X_{centre}$ (mm) | $Y_{centre}$ (mm) |
|---|---|---|---|
| 0.06 | 0.01 | 1.85 | -1.17 |

### 5.3.3 M2 uncoated (unannealed)

Table 20: M2 uncoated (unannealed)

***System distances for analysis***

| B [mm] | B Offset [mm] | B offset Cal factor | A [mm] | L [mm] | L2S [mm] | Total [mm] |
|---|---|---|---|---|---|---|
| 385 | 0.0 | 0.9765625 | 71.0 | 56.7 | 385.0 | 512.7 |

***Analysis at lens alignment frequency (100 GHz)***

| $\alpha$ [deg] | $\beta$ [deg] | $X_0$ [mm] | $Y_0$ [mm] |
|---|---|---|---|
| 0.21 | -0.55 | 0.73 | -3.91 |

***Predicted from 100 GHz fit with no motion control offsets***

| $X_{0Pred}$ [mm] | $Y_{0Pred}$ [mm] |
|---|---|
| -4.92 | -1.88 |

***Deduced motion control system offsets (constant)***

| $\Delta X_0$ [mm] | $\Delta Y_0$ [mm] |
|---|---|
| -5.65 | 2.03 |

The $X_0$ and $Y_0$ in the table above are 0.73 and -3.91 mm respectively. Compared to the Gaussian fit values of 0.96 and -3.85 mm some discrepancies in the values were seen. These discrepancies are believed to have been caused by the absorber placed onto the front of the receiver probe which, when tested, caused inconsistent results for the $X_{centre}$ and $Y_{centre}$ positions. The $\alpha$ and $\beta$ values for the measurement of 0.21° and -0.55° respectively were close to the MODAL simulation measurements of 0.19° and -0.49°.

Table 21: Table of the $\alpha$, $\beta$, $X_{centre}$ and $Y_{centre}$ values obtained from the Gaussian Fitter program for the modelled feed horn beam pattern of the M2 uncoated lens setup.

| $\alpha$ (deg) | $\beta$ (deg) | $X_{centre}$ (mm) | $Y_{centre}$ (mm) |
|---|---|---|---|
| 0.19 | -0.49 | 0.96 | -3.85 |

### 5.3.4 M2 uncoated (annealed)

Table 22: M2 uncoated (annealed)

***System distances for analysis***

| B [mm] | B Offset [mm] | B offset Cal factor | A [mm] | L [mm] | L2S [mm] | Total [mm] |
|---|---|---|---|---|---|---|
| 364.4 | 0.0 | 1.0 | 71.0 | 58 | 364.4 | 493.4 |

***Analysis at lens alignment frequency (100 GHz)***

| $\alpha$ [deg] | $\beta$ [deg] | $X_0$ [mm] | $Y_0$ [mm] |
|---|---|---|---|
| 0.00 | -0.01 | -0.33 | 1.83 |

***Predicted from 100 GHz fit with no motion control offsets***

| $X_{0Pred}$ [mm] | $Y_{0Pred}$ [mm] |
|---|---|
| -0.09 | 0.00 |

***Deduced motion control system offsets (constant)***

| $\Delta X_0$ [mm] | $\Delta Y_0$ [mm] |
|---|---|
| 0.24 | -1.83 |

The $X_0$ and $Y_0$ values are -0.33 and 1.83 mm which compare well with the -0.3 and 1.76 mm values for the centre from the simulation. The $\alpha$ and $\beta$ values from measurement of 0° and -0.01° match the 0.01° and -0.01° from the simulation.

Table 23: Table of the $\alpha$, $\beta$, $X_{centre}$ and $Y_{centre}$ values obtained from the Gaussian Fitter program for the modelled feed horn beam pattern of the M2 annealed lens setup.

| $\alpha$ (deg) | $\beta$ (deg) | $X_{centre}$ (mm) | $Y_{centre}$ (mm) |
|---|---|---|---|
| 0.01 | -0.01 | -0.3 | 1.76 |

### 5.3.5 M1 coated (annealed)

Table 24: M1 coated (annealed)

***System distances for analysis***

| B [mm] | B Offset [mm] | B offset Cal factor | A [mm] | L [mm] | L2S [mm] | Total [mm] |
|---|---|---|---|---|---|---|
| 371.4 | 0.0 | 0.9765625 | 71.0 | 59.8 | 371.4 | 502.2 |

***Analysis at lens alignment frequency (100 GHz)***

| $\alpha$ [deg] | $\beta$ [deg] | $X_0$ [mm] | $Y_0$ [mm] |
|---|---|---|---|
| -0.12 | 0.10 | -3.02 | -0.17 |

***Predicted from 100 GHz fit with no motion control offsets***

| $X_{0Pred}$ [mm] | $Y_{0Pred}$ [mm] |
|---|---|
| 0.88 | 1.05 |

***Deduced motion control system offsets (constant)***

| $\Delta X_0$ [mm] | $\Delta Y_0$ [mm] |
|---|---|
| 3.90 | 1.22 |

The measurement $X_0$ and $Y_0$ are -3.02 and -0.17 mm. The model $x$ centre and $y$ centre are -3.05 and -0.13 mm. The parameters $\alpha$ and $\beta$ were -0.12° and 0.10° for the measurement and -0.12° and 0.09° for the model.

Table 25: Table of the $\alpha$, $\beta$, $X_{centre}$ and $Y_{centre}$ values obtained from the Gaussian Fitter program for the modelled feed horn beam pattern of the M1 coated lens setup.

| $\alpha$ (deg) | $\beta$ (deg) | $X_{centre}$ (mm) | $Y_{centre}$ (mm) |
|---|---|---|---|
| -0.12 | 0.09 | -3.05 | -0.13 |

### 5.3.6 M2 coated (annealed)

Table 26: M2 coated (annealed)

***System distances for analysis***

| B [mm] | B Offset [mm] | B offset Cal factor | A [mm] | L [mm] | L2S [mm] | Total [mm] |
|---|---|---|---|---|---|---|
| 360 | 0.0 | 1.0 | 71.0 | 59.9 | 360.0 | 490.9 |

***Analysis at lens alignment frequency (100 GHz)***

| $\alpha$ [deg] | $\beta$ [deg] | $X_0$ [mm] | $Y_0$ [mm] |
|---|---|---|---|
| -0.33 | 0.01 | -1.41 | -0.57 |

***Predicted from 100 GHz fit with no motion control offsets***

| $X_{0Pred}$ [mm] | $Y_{0Pred}$ [mm] |
|---|---|
| 0.09 | 2.83 |

***Deduced motion control system offsets (constant)***

| $\Delta X_0$ [mm] | $\Delta Y_0$ [mm] |
|---|---|
| 1.50 | 3.40 |

The $X_0$ and $Y_0$ for the measurement are -1.41 and -0.57 mm. For the model the $x$ centre and $y$ centre are -1.36 and -0.64 mm. The $\alpha$ and $\beta$ for the measurement are -0.33° and 0.01°. For the model they are -0.32° and 0.02°.

Table 27: Table of the $\alpha$, $\beta$, $X_{centre}$ and $Y_{centre}$ values obtained from the Gaussian Fitter program for the modelled feed horn beam pattern of the M2 coated lens setup.

| $\alpha$ (deg) | $\beta$ (deg) | $X_{centre}$ (mm) | $Y_{centre}$ (mm) |
|---|---|---|---|
| -0.32 | 0.02 | -1.36 | -0.64 |

### 5.3.7 M1 coated (annealed) improved alignment

Table 28: M1 coated (annealed) improved

***System distances for analysis***

| B [mm] | B Offset [mm] | B offset Cal factor | A [mm] | L [mm] | L2S [mm] | Total [mm] |
|---|---|---|---|---|---|---|
| 386.0 | 0.0 | 1.0 | 75.0 | 59.9 | 386.0 | 520.9 |

***Analysis at lens alignment frequency (100 GHz)***

| $\alpha$ [deg] | $\beta$ [deg] | $X_0$ [mm] | $Y_0$ [mm] |
|---|---|---|---|
| -0.12 | 0.00 | 0.16 | 1.03 |

***Predicted from 100 GHz fit with no motion control offsets***

| $X_{0Pred}$ [mm] | $Y_{0Pred}$ [mm] |
|---|---|
| 0.00 | 1.09 |

***Deduced motion control system offsets (constant)***

| $\Delta X_0$ [mm] | $\Delta Y_0$ [mm] |
|---|---|
| -0.16 | 0.06 |

The $X_0$ and $Y_0$ are 0.16 and 1.03 mm respectively. The $X_{centre}$ and $Y_{centre}$ form the Gaussian Fitter are 0.16 and 1 mm matching well with the offsets from measurements. The $\alpha$ and $\beta$ angles are -0.12° and 0° respectively compared to -0.11° and 0° from the model matching closely.

Table 29: Table of the $\alpha$, $\beta$, $X_{centre}$ and $Y_{centre}$ values obtained from the Gaussian Fitter program for the modelled feed horn beam pattern of the M1 coated improved alignment lens setup.

| $\alpha$ (deg) | $\beta$ (deg) | $X_{centre}$ (mm) | $Y_{centre}$ (mm) |
|---|---|---|---|
| -0.11 | 0.00 | 0.16 | 1.00 |

### 5.3.8 M2 coated (annealed) improved alignment

Table 30: M2 coated (annealed) improved

***System distances for analysis***

| B [mm] | B Offset [mm] | B offset Cal factor | A [mm] | L [mm] | L2S [mm] | Total [mm] |
|---|---|---|---|---|---|---|
| 364.5 | 0.0 | 1.0 | 83.6 | 59.9 | 364.5 | 508.0 |

***Analysis at lens alignment frequency (100 GHz)***

| $\alpha$ [deg] | $\beta$ [deg] | $X_0$ [mm] | $Y_0$ [mm] |
|---|---|---|---|
| -0.12 | 0.00 | -2.98 | -3.77 |

***Predicted from 100 GHz fit with no motion control offsets***

| $X_{0Pred}$ [mm] | $Y_{0Pred}$ [mm] |
|---|---|
| 0.00 | 1.06 |

***Deduced motion control system offsets (constant)***

| $\Delta X_0$ [mm] | $\Delta Y_0$ [mm] |
|---|---|
| 2.98 | 4.83 |

The $X_0$ and $Y_0$ values are -2.98 and -3.77 respectively. These compare well with the $X_{centre}$ and $Y_{centre}$ values of -2.92 and -3.81 respectively. The $\alpha$ and $\beta$ values are -0.12 and 0 compared to -0.11 and 0.01 from the model.

Table 31: Table of the $\alpha$, $\beta$, $X_{centre}$ and $Y_{centre}$ values obtained from the Gaussian Fitter program for the modelled feed horn beam pattern of the M2 coated improved alignment lens setup.

| $\alpha$ (deg) | $\beta$ (deg) | $X_{centre}$ (mm) | $Y_{centre}$ (mm) |
|---|---|---|---|
| -0.11 | 0.01 | -2.92 | -3.81 |

Now that the feed horn model matched the measurement we can analyse the lens simulation knowing any offsets were due to the lens and not the feed horn or scan plane setup.

## 5.4 MODAL Measurement Matching

The lens modelling and analysis can now be performed in the knowledge that the feed horn in the simulation is setup accurately with respect to the measurement system. The next process is to simulate the lens and then subsequently alter its position in order to obtain better agreement between the model and measurement. First simulations were completed using the lens rotated at the same angle as the horn and aligned with the axis of the centre of the Gaussian beam emitted by the horn. After this, the results were analysed and parameters changed marginally within an expected tolerance to find better agreement between the model and measurement. Each lens had to also contain the correct value for the refractive index. For the unannealed lenses a refractive index of 1.51817 and for the annealed lenses a refractive index of 1.5174, as measured by Cardiff University for the lenses, see section 2.3.

A program, called the MODAL comparison tool, included in the Gaussian Fitter program package, in order to compare measurement with MODAL simulated data and assess the agreement between the two. The program compares both the power and the phase between measured and simulated data. A difference in power was found due to the limitation of the model of the probe. The deviation is caused by the way in which the model calculates the total power received at the port. It calculates the total power received over the area of the probe aperture assuming a fundamental Gaussian beam mode only. This does not take into account induced currents in the waveguide or higher order modes coupling to the waveguide. Figure 118 shows the power level received by

the receiver probe through measurement and different simulation setups. F1 MODAL shows the power over a range of frequencies taken directly from a MODAL simulation. F1ref is the total power incident on the area covered by the probe. F1pw is the power predicted including coupling through surface currents induced on the probe.

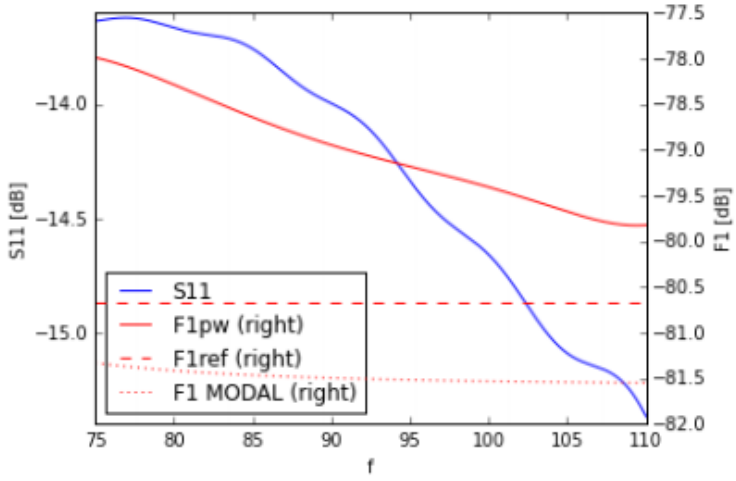


Figure 118: The power received by the probe with different parameters taken into account over a range of frequencies. F1 MODAL is the power MODAL calculates for the probe. F1ref is the total power incident on the receiver probe. F1pw is result obtained Finite Difference Time Domain in CST Microwave Studio, using complete model of the probe.

This data shows that the deviation seen between the MODAL model and measurement can be accounted for by the use of only the fundamental mode and through exclusion of induced currents. This deviation is nearly uniform across the scan plane, as seen in Figure 119, and was therefore removed through averaging the offset and applying it to the model to bring them into close agreement. The phase was also changed as the model had a different starting phase at the input signal to the measurement creating a phase change between them. As comparison from the zero phase position was desired, the model phase was offset to match the measured phase at the centre of the scan plane.

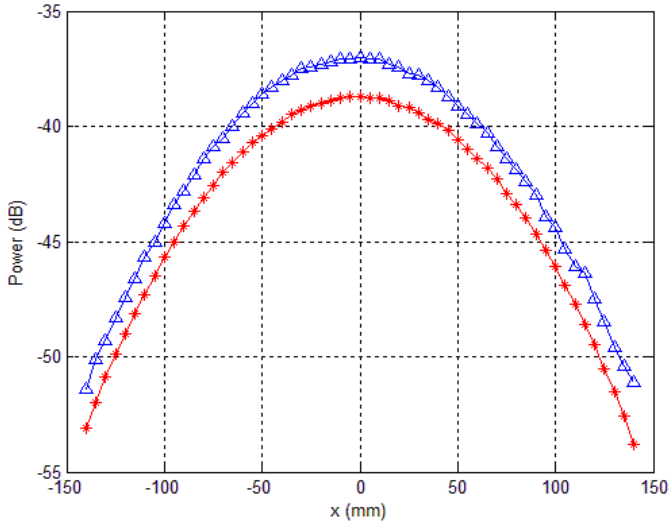


Figure 119: A cut taken along the x-axis for a feed horn scan at 100 GHz showing the deviation between the measurement in blue and model in red. The offset between them is 1.7 dB on average.

The power was then compared as the absolute value of the difference between the measurement and the model divided by the maximum power value at each point. This gives a difference relative to the maximum power at each point. For comparison of phase a direct difference between phase values was used, after adjusting the model phase to match the phase of the measurement at the centre of the scan plane. This means they will match at the centre, with the difference producing a zero value, with any deviations away from the centre represented as non-zero values.

When looking at the comparison the power levels should be small at all points and the phase should be flat at zero phase position across all values. There will be discrepancies at the edges of the area, as the holder for the lens in the measurement system is not modelled in the simulation and because the power falls off, so phase becomes undefined. Initially the focus was on one lens to assess what were the most likely causes of differences between the model and the measurement. The M1 uncoated (unannealed) lens was simulated with two passes to simulate reflection within the system. The result was a beam with the power agreeing well in the centre but deviating towards the edges. For the coated lens simulations the number of passes of the lens was reduced to one to approximate the effect of the coating.

The phase difference had a slope for both the $\alpha$ and $\beta$ angles. In order to quantify the agreement between the phase of the measurement and simulation, the variance and standard deviation of the residuals were calculated. Masking imposed so that only

values within 130 mm of the centre of the grid were considered. This was done to exclude the outlying pixels where power is negligible. The variance and standard deviation in phase difference before changing any parameters was 0.07 and 0.26°.

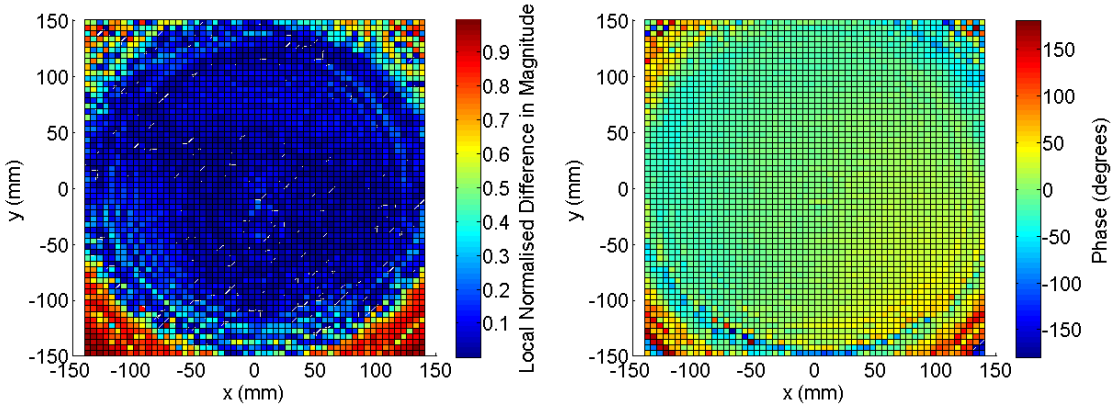


Figure 120: Figure from the comparison program showing the result of taking the difference between the measurement and the model. The power difference on the left shows good agreement in the centre. The phase difference on the right has a slope along both the *x* and *y* axes.

### 5.4.1 Angular adjustment

In order to correct for the slope in the phase, the lens was rotated within its local frame about the *y* and *x* axes, corresponding to angles $\beta$ and $\alpha$. In measurements the $\alpha$ angle was fixed to the angle that the lens holder made with the scan plane. This angle was therefore more likely to be offset and the source of deviation in the system. The angle in the simulation was changed in steps of 0.5 degrees from 0 to ±2 degrees. The angle made little appreciable difference to the phase of the beam and could only account for the offset at a point beyond 2 degrees. This value was too large to be a reasonable offset in the system, due to the accuracy of the system alignment. For a 2 degree rotation around the *x*-axis the variance is 0.08 and the standard deviation is 0.28, an increase from the default lens simulation.

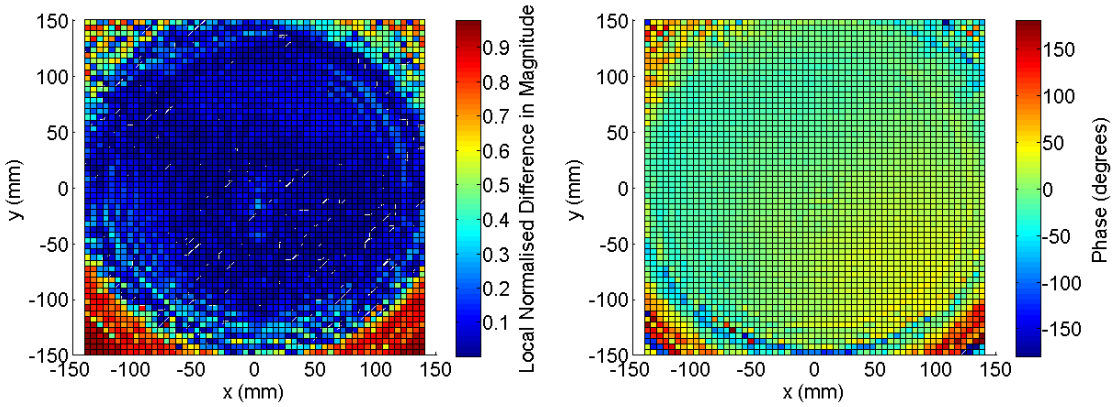


Figure 121: Figure of the comparison between the lens measurement and the model after the model lens was rotated by 2° around the *x*-axis. This results in a small change to the phase which only decreases the level of agreement between the measurement and model.

### 5.4.2 Lens translation

Another possible source of error between the measurement and the simulation was the centre position of the lens. This could be incorrect, as the alignment of the rotation stage centre relied on perfect alignment between the feed horn and scan plane, which could not be attained in the measurement system. The lens was translated in both the *y* and *x* directions of its local frame to test the effect on the phase comparison. The parameters $X_{\text{OffsetLens}}$ and $Y_{\text{OffsetLens}}$ were created in the MODAL simulation to represent these offsets. Small changes in the position of the lens in both *x* and *y* axes had appreciable effects on the residual phase. These parameters were therefore thought to be the main source of error between the measurement and model. To determine the model that agreed best with the measurement, the variance and standard deviation of the difference in phases were calculated and the lens then translated in order to minimise the variance and standard deviation.

### 5.4.3 M1 uncoated (unannealed)

The M1 uncoated lens was displaced in steps of 0.5 mm in order to analyse the agreement between the measurement and model. The lens was displaced by -0.5 mm in the *x* direction and 0.5 mm in the *y* direction. This resulted in a significant increase in the agreement between measurement and model, with variance in phase difference changing from 0.07 to 0.01 and standard deviation changing from 0.26° to 0.12°.

## M1 uncoated unannealed

| $X_{OffsetLens}$ [mm] | $Y_{OffsetLens}$ [mm] | Variance | Standard Deviation [degrees] |
|---|---|---|---|
| 0 | 0 | 0.07 | 0.26 |
| -0.5 | 0.5 | 0.01 | 0.12 |
| -1 | 1 | 0.07 | 0.26 |

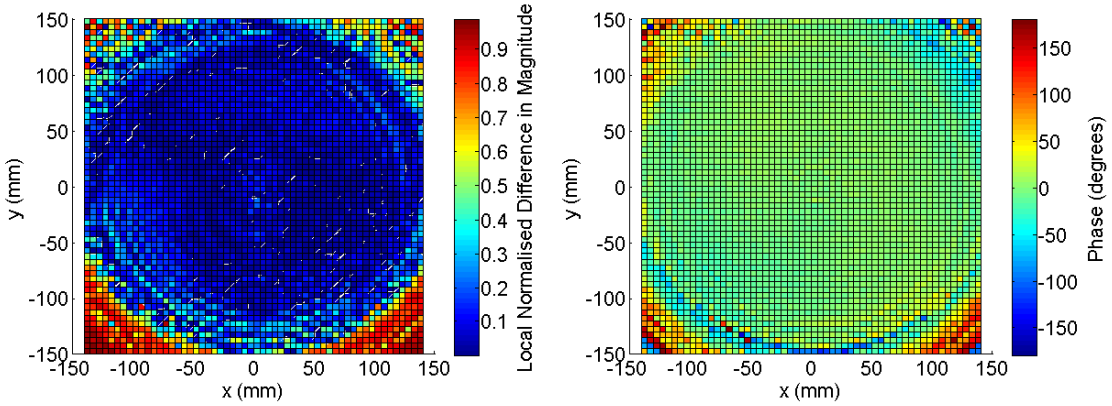


Figure 122: Comparison between measurement and model of lens M1 uncoated (unannealed) displaced -0.5 mm in the *x*-axis and 0.5 mm in the *y*-axis.

### 5.4.4 M2 uncoated (unannealed)

For the M2 uncoated unannealed lens the offset of the lens position in the *x*-axis was large due to the large offset of the centre position of the feed horn relative to the scan plane centre of -5.65 mm. The best result was found with $X_{OffsetLens}$ set to 2.5 mm and the $Y_{OffsetLens}$ to -1.0 mm. The variance changed from 0.84 to 0.02 and the standard deviation from 0.92° to 0.15°.

## M2 uncoated unannealed

| $X_{OffsetLens}$ [mm] | $Y_{OffsetLens}$ [mm] | Variance | Standard Deviation [degrees] |
|---|---|---|---|
| 0 | 0 | 0.84 | 0.92 |
| 1 | -1 | 0.31 | 0.56 |
| 2.5 | -1 | 0.02 | 0.15 |

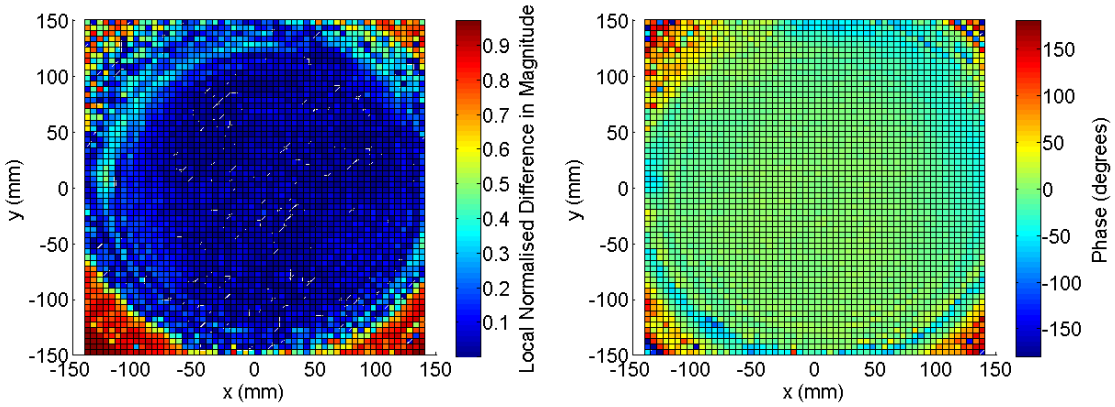


Figure 123: Image of the best comparison from the comparison program for lens M2 uncoated (unannealed) with $X_{\text{OffsetLens}}$ set to 2.5 mm and the $Y_{\text{OffsetLens}}$ set to -1 mm.

### 5.4.5 M2 uncoated (annealed)

For the M2 uncoated annealed lens the *y* axis had a larger misalignment due to the horn centring on the scan plane. Therefore a larger correction in this axis was required. The best result was acquired with $X_{\text{OffsetLens}}$ at -0.5 mm and $Y_{\text{OffsetLens}}$ at -1.2 mm. The variance changed from 0.22 to 0.01 and the standard deviation from 0.46 to 0.1.

**M2 uncoated annealed**

| $X_{\text{OffsetLens}}$ [mm] | $Y_{\text{OffsetLens}}$ [mm] | Variance | Standard Deviation [degrees] |
|---|---|---|---|
| 0 | 0 | 0.22 | 0.46 |
| 0 | -0.5 | 0.1 | 0.31 |
| -0.5 | -1 | 0.02 | 0.14 |
| -0.5 | -1.2 | 0.01 | 0.1 |
| -0.5 | -1.5 | 0.02 | 0.13 |

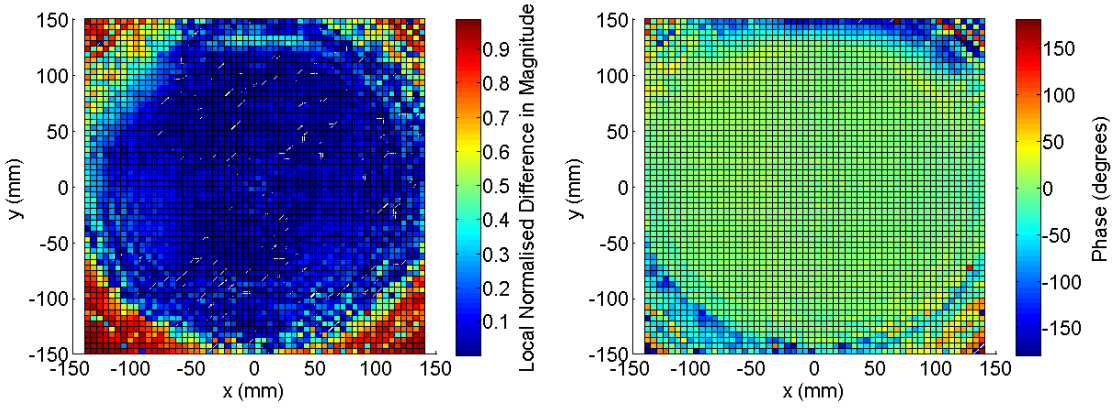


Figure 124: Image of the best comparison from the comparison program for lens M2 uncoated annealed with the $X_{\text{OffsetLens}}$ set to -0.5 mm and the $Y_{\text{OffsetLens}}$ set to -1.2 mm.

### 5.4.6 M1 coated (annealed)

To bring the simulation of lens M1 coated (annealed) into better agreement with the measurement and model, $X_{\text{OffsetLens}}$ was set to 0.5 mm and $Y_{\text{OffsetLens}}$ was set to -0.5 mm. The variance changed from 0.27 to 0.08 and the standard deviation reduced from 0.51° to 0.28°.

**M1 coated annealed**

| $X_{\text{OffsetLens}}$ [mm] | $Y_{\text{OffsetLens}}$ [mm] | Variance | Standard Deviation [degrees] |
|---|---|---|---|
| 0 | 0 | 0.27 | 0.51 |
| 0.5 | -0.5 | 0.08 | 0.28 |

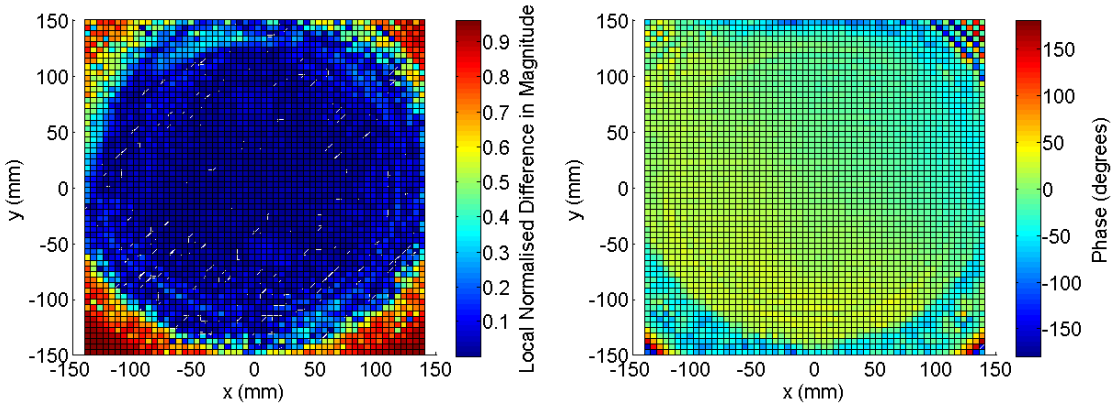


Figure 125: Image of best comparison between measurement and model of M1 coated (annealed) with $X_{\text{OffsetLens}}$ set to 0.5 mm and $Y_{\text{OffsetLens}}$ set to -0.5 mm.

### 5.4.7 M2 coated (annealed)

To bring the M2 coated lens into best agreement between the measurement and model, $X_{\text{OffsetLens}}$ was set to 0.5 mm and $Y_{\text{OffsetLens}}$ to -0.5 mm. The variance reduced from 0.11 to 0.03 and the standard deviation reduced from 0.33 to 0.17.

**M2 coated annealed**

| $X_{\text{OffsetLens}}$ [mm] | $Y_{\text{OffsetLens}}$ [mm] | Variance | Standard Deviation [degrees] |
|---|---|---|---|
| 0 | 0 | 0.11 | 0.33 |
| 0.25 | -0.25 | 0.06 | 0.24 |
| 0.5 | -0.5 | 0.03 | 0.17 |

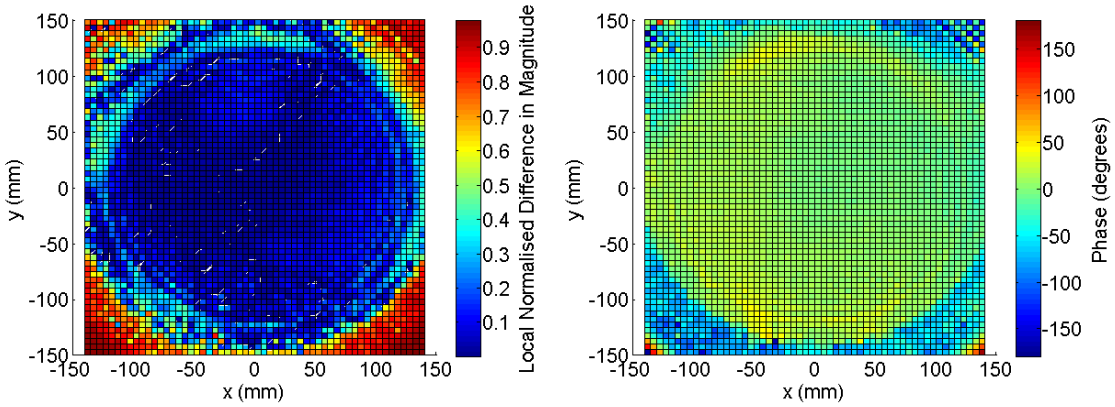


Figure 126: Image of the best comparison between measurement and model of M2 coated (annealed) with $X_{\text{OffsetLens}}$ set to 0.5 mm and $Y_{\text{OffsetLens}}$ set to -0.5 mm.

For both the M1 and M2 coated lenses the phase residuals had curvature. This is believed to be due to not including the coating in the simulation, as the effect becomes more predominant towards the edges of the lens, where the coating would have a larger effect due to its relative thickness to that of the lens becoming more significant towards the edges.

### 5.4.8 High resolution comparison

Simulations were also performed for a comparison with the high resolution measurements that were performed at the centre of the lens. These measurements were made to assess the performance of the coating material applied to the lens. The phase comparison between the two should be flat as with the previous comparisons. For the M1 uncoated lens there is a difference in the standing wave pattern of the measurement and simulation, which appears as rings in the phase residuals due to a difference the standing waves in the measurement and model. The ringed pattern also appears in the residual power. The same pattern was observed in the residuals of the M2 uncoated measurement as well. For these high resolution simulations $X_{\text{OffsetLens}}$ and $Y_{\text{OffsetLens}}$ were set to values that gave the lowest variance and standard deviation values.

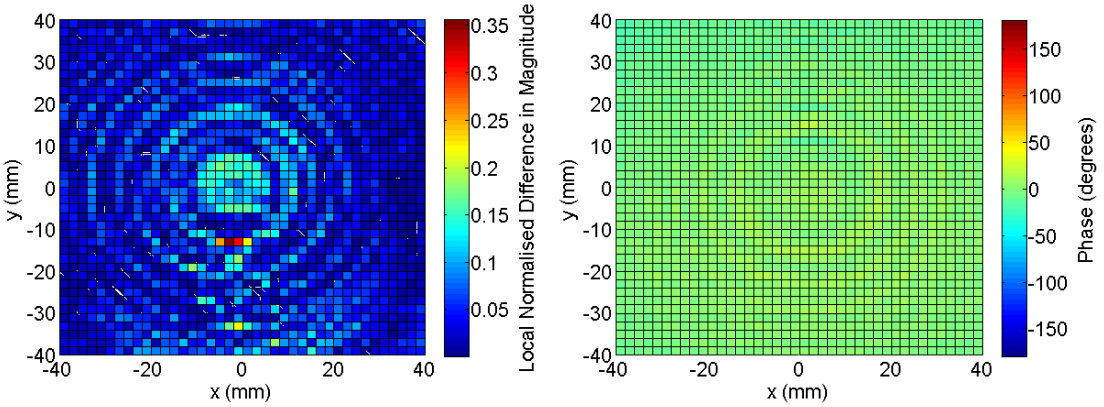


Figure 127: Comparison of the linear power and phase between the high resolution measurement and model of the M1 uncoated lens.

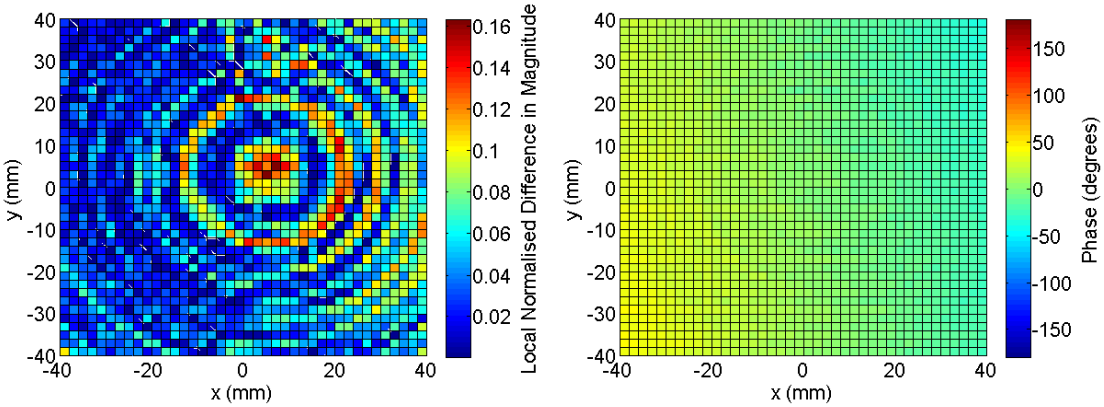


Figure 128: Comparison of the phase and power for the M2 uncoated lens high resolution simulation and phase.

For the coated M1 and M2 high resolution comparisons the power has no distinguishable standing wave pattern present. This is due to the effectiveness of the coating to suppress reflections for the 100 GHz frequency. The phase residuals do not display the standing wave pattern either. The residual phase is sloped in one direction indicating an offset still present in the system and a curvature due to the coating not being implemented in the simulation.

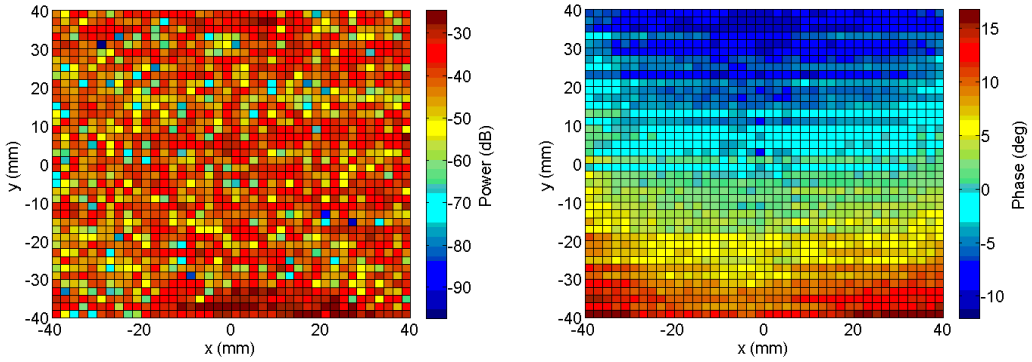


Figure 129: Plot of the residual power and phase for the M1 coated lens.

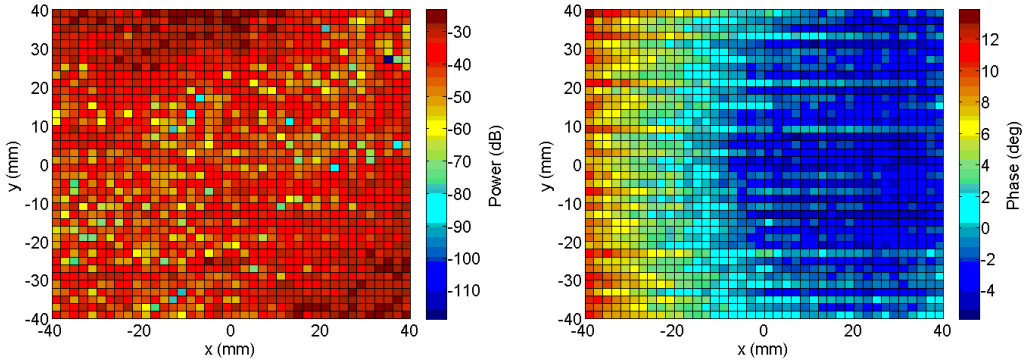


Figure 130: The residual power and phase for the M2 coated lens.

## 5.5 Conclusion

The modelling system enabled an accurate representation of the measurement system to be setup with accurate positioning of components including any positional offsets. This furthered our understanding of the offsets present in the measurement system and to identify some areas in which the setup of the measurement system could be improved. Firstly the feed horn setup in model and measurement setups were compared. These showed good agreement between the model and measurement between each feed horn setup for all lens measurements after the determined system offsets were input into the model. This confirms that the alignment procedure for the horn was both accurate and enabled full determination of the offsets still present in the system after alignment.

The lens modelling that was performed thereafter showed that the measurement and model were out of agreement. To determine the offset in the system causing this disagreement the lens orientation and position could be modified within reasonable ranges for each parameter. The most significant offset was identified as the centre

position of the lens. After the lens was annealed it shrunk. This effected the position of the mounting holes that were used to mount the lens on the lens holder. In order to enable the lens to be mounted subsequently, the holes were expanded by removing the material from the mounting holes to the edge of the lens. This resulted in inaccurate centring of the lens in the holder in terms of both vertical and horizontal positions. The correction offset values for the centre position of the lens for both the annealed and coated lenses were therefore larger than those required for the unannealed lenses.

The high resolution comparison between the measurement and model showed that the uncoated lens included the standing wave pattern, caused due to multiple reflections within the lens, whereas the coated lenses displayed no pattern in the residual power and phase. The residual phase for the high resolution results also shows a non uniform phase profile from one side of the lens to the other. This shows subsequent work to bring the measurement and model into alignment could be performed. The angular offset of the lens could now be assessed again with the lens in its current position to determine if this has a greater effect with the lens closer to the correct centre position. The distance from the horn to the lens could also be adjusted but the measurement method for this distance is believed to be very accurate.

# Chapter 6: Summary of Results and Conclusions

## 6.1 Introduction

There were several aims of this project as follows:

1. Determine the most appropriate material for the lens body and coating. This was carried out by Cardiff University.
2. Confirm the accuracy and reproducibility of the manufacturing process, for both the main body of the lens and the coating.
3. Characterise the optical performance of the lenses and compare to the predicted performance.
4. Confirmation of the model developed to simulate the lens and the coating. This was done by the TICRA institute and subsequently in Maynooth University for verification of the in-house software MODAL.

## 6.2 Material and Manufacturing

In order to determine the material to use for the body of the lenses and the anti-reflection coating, Cardiff University performed tests on different materials. They measured the refractive index of different materials from different manufacturers in order to determine the best material. For the body of the lenses UHMW-PE was chosen. PTFE was chosen for the anti-reflection coating. From the test batch material supplied by Ensinger Ltd. the refractive index for the body was experimentally determined by Cardiff University to be an average of 1.5275±0.0008 across the frequency range from 90-1200 GHz. This value was the refractive index from which the lenses were designed. Three M type lenses were then manufactured for MU and three C type lenses were manufactured for Cardiff University. The third of each type of lens was held in reserve, for use in the event of an issue with one of the main lenses. The surface profile of each lens was measured to determine the offset of the curvature of the lens away from the designed value. This was done by measuring the distance deviation across the lens with

the Cardiff surface measurement system. The deviation was found to be a maximum of 521 μm across the surface of the lenses.

After completion of testing of the first M type lens at MU and the subsequent modelling by TICRA, an error was found. The refractive index from the test batch when used in the simulation did not correlate the measurement to the model. TICRA therefore changed the refractive index value in order to better correlate the theory with measurement. This succeeded in bringing the measurement and model into better agreement.

In order to confirm the suspicion that the lens had a different value of refractive index to the test batch, the extra C3 lens made for Cardiff University had off cuts removed in order to determine its refractive index. The results of the measurement confirmed that the refractive index was significantly different to the test batch value at 1.51817±0.00006. This was consistent with the value used by TICRA in their simulations of the lens of 1.5188.

This was the first success of the measurements performed at MU but brought into doubt the reproducibility of the manufacturing process to ensure consistent refractive index values of the material. It is critical that the refractive index be predictable between material batches for accurate design of the lenses. If the value cannot be guaranteed then the process may require a further step, to test the refractive index of the batch that the lens will be manufactured from, before the lens is designed.

During the measurement of the M2 uncoated lens the M1 uncoated lens was in the process of being coated. During this process the lens was found to have shrunk due to the heating used in the coating process. This would not have occurred if the material had been annealed before the lens was manufactured, as was intended. Therefore the annealing process effect on the lens had to be tested. To do this the remains of the extra C3 lens was annealed and the refractive index measured again. This produced a value of 1.5174±0.0002 for the refractive index of the lens. Lens M2 was also annealed separately before it was coated in order to measure the change in the shape of the lens due to the annealing process. The lens shrunk at the sides but increased in thickness at the centre. This produced a significant change in the curvature on both surfaces of the lens.

## 6.3 Lens Measurements

Optical lens measurements were performed to assess the performance of the lenses over the frequency range of MU's measurement system, from 75-110 GHz in 5 GHz steps, and also to test the performance of the antireflective coating that was applied to the lens. First it was necessary to determine a sequence of measurements to perform in order to assess the lens and the coating. It was decided that two main measurements would be performed on the lens. The first was a full range scan performed over the entire area of the lens to measure the entire transmitted beam. This would allow the performance of the lens to be tested in comparison to the design of the lens. The second measurement was a high resolution scan of the centre area of the lens to assess the effect of standing waves generated by reflections in the lens and the subsequent performance of the anti-reflective coating to mitigate these effects.

One other key scan performed was a scan of the feed horn without the lens in the system but over the same area as used for the main lens measurement. This scan was used in order to determine the offsets between the feed horn and scan plane in the system for input into the computational models. Using these measurements improvements were made to the alignment of the system. The absorber mounted on the front of the receiver probe was found to cause inconsistencies between measurements. To resolve this, the absorber was replaced with a solid piece of absorber that made reproducible measurements possible. Due to difficulty in aligning the horn to the scanning plane of the translation stage, two tip tilt stages were incorporated to allow the emitter and receiver heads to be tilted by small increments precisely. This resulted in a more accurate alignment procedure that required, in most cases, only one attempt in order to obtain good alignment.

A measurement was performed over a small area at the centre of the lens in order to assess the effectiveness of the antireflection coating that was applied to the surface. For the uncoated M1 and M2 lens measurements, standing waves were clearly visible due to reflections within the lens. After the anti-reflection coating was applied these reflections were significantly reduced at 100 GHz. The coating's performance decreased in effectiveness away from this frequency. At 75 GHz the standing waves were thus visible even with the coating applied.

## 6.4 Comparison between Measurements and MODAL Simulations

After lens measurements were completed, the lens measurements were simulated using the in-house software package MODAL. This was done to confirm the accuracy of the alignment process for the measurement system. For the lens modelling, the first test was to compare the feed horn measurements with simulations. This would confirm the accuracy of the measurements and the correct implementation of the offsets that were calculated for the system. The measured feed horn patterns were numerically fitted to a Gaussian beam using the Gaussian Fitter program. This was to determine the angular and positional offsets of the feed horn with respect to the scanning plane. The offsets were included in the simulation and the model run for a direct measurement of the feed horn to the scan plane. The data from the model feed horn was then input into the Gaussian Fitter program to ensure correct implementation of the offsets in the model. For all the feed horn comparisons made the simulations and measurements were very close to each other. Causes of remaining discrepancies between the model and the measurement arose 1) from the absorber that was used for the first measurements of the lenses and 2) where the offsets for the angles or scan plane centre location were high.

For the lens modelling the simulations were run for the uncoated cases first. The number of passes through the lens was set to two in order to simulate the standing waves caused by reflections within the lens. There was an offset between measured and simulated phase fronts. This was believed to be due to an angle offset of the lens with respect to the incoming beam. The lens was angled with rotation around its local $x$ and $y$ axes to assess the effect on the detected beam. The resultant phase was not significantly impacted and could not account for the offset in the residual phase measured. The lens was then displaced in the $x$ and $y$ axes of its local frame. This produced a significant change in the phase and gave good agreement between the model and the measurement for the full lens scan. The phase comparisons did not match perfectly for the high resolution scans, as the standing wave pattern in the residuals was still present after applying the offsets for the centre position.

For the coated lenses the simulations were completed with one pass through the lens to approximate the effect of the lens coating. The comparison of model to measurement for the full range scans required the same displacement procedure in the $x$ and $y$ directions in order to resolve the phase tilt in the comparison patterns. After the

best fit was achieved with the comparison phase there was still a curvature in the residual phase. This is believed to be caused by the coating, which was not included in the model of the lens, as the phase curvature is at its most extreme at the edge of the lens where the coating would produce the largest effect. The high resolution measurements show that the phase has a curvature but there is no standing wave effect present at a frequency of 100 GHz, displaying the effectiveness of the coating at this frequency.

# Bibliography


Alpher, R. A., H. Bethe, and G. Gamow. “The Origin of Chemical Elements.” *Physical Review*, 1948: 803-804.

Alpher, Ralph, and Robert Herman. “Evolution of the Universe.” *Nature*, 1948: 774-775.

Bennett, C L, M Halpern, and G Hinshaw. “First-Year Wilkinson Microave Anisotropy Probe (WMAP) Observations: Preliminary Maps and Basic Results.” *The Astrophysical Journal Supplement Series*, no. 148 (September 2003).

Bennett, C. L., D. Larson, J. L. Weiland, N. Jarosik, and G. Hinshaw. “Nine Year Wilkinson Microwave Anistropy Probe (WMAP) Observations: Final Results and Maps.” *Astrophysics Journal*, 2013: 100.

Benoit, A, and P Ade. “First detection of polarization of the submillimetre diffuse galactic dust emission by Archeops.” *A&A*, 2004: 571-582.

Boggess, N. W., J. C. Mather, R. Weiss, C. L. Bennett, E. S. Cheng, and E. Dwek. “The COBE mission - Its design and performance two years after launch.” *Astrophysical Journal*, 1992: 420-429.

B-Pol collaberation. “A B-Polarisation Satellite Mission (B-Pol) For Detecting Primordial Gravitational Waves Generated During Inflation.”

B-Pol collaboration. *Proposal List.* 2007. http://www.b-pol.org/pdf/BPOLFullList.pdf (accessed May 26, 2015).

Bradley, Carroll, and Ostiel Dale. *An Introduction to Modern Astrophysics.* Person Addison/Wesley, 2007.

Brown, M. L., P Ade, and C O'Sullivan. “Improved Measurements of The Temperature and Polarisation of The Cosmic.” *The Astrophysical Journal*, 2009: 978-999.

ESA. *Image of Planck sky maps.* 2013. www.esa.int/spaceinimages/images/2013/04/Planck_all-sky_frequency_maps.

—. *Planck Mission.* September 2009. http://sci.esa.int/planck/ (accessed August 19, 2014).

Gibson, Walter C. *The Method of Moments in Electromagnetics.* Boca Raton: Taylor & Francis Group, LLC, 2008.

Goldsmith, Paul F. *Quasioptical Systems: Gaussian Beam Quasioptical Propagation and Applications.* IEEE Press/Chapman & Hall, 1998.

Gradziel, M. L., et al. “Modelling and Experimental Validation of Dielectric Lenses for use in Future Cosmic Microwave Background Satellites.” 2013.

Hargrave, Peter, et al. “Critical Breadboards Manufacture and Tests Report (TN6).” 2013.

Hu, Wayne. *Quadrupole Types and Polarisation Patterns.* 2001. http://background.uchicago.edu (accessed November 11, 2014).

Hu, Wayne, and Martin White. “A Polarisation Primer.” *New Astronomy 2,* 1997: 323-344.

NASA. *COBE.* 23 August 2013. http://nssdc.gsfc.nasa.gov/nmc/spacecraftDisplay.do?id=1989-089A (accessed 2014).

—. *FIRAS Images.* 13 April 2013. http://lambda.gsfc.nasa.gov/product/cobe/firas_image.cfm (accessed March 3, 2015).

—. *Parameters of Cosmology: What WMAP Records.* 21 December 2012. map.gsfc.nasa.gov/mission/sgoals_parameters_wmap.html (accessed Feburary 25, 2015).

O'Sullivan, C, and G Cahill. “The quasi optical design of the QUaD telescope.” *Infrared Physics and Technology*, 2008: 277-286.

Planck Collaboration. “Planck 2013 Results. XV. CMB Power Spectra and Likelihood.” *EDP Sciences,* 2014.

Planck Collaboration. “Planck 2015 results. XIII. Cosmologiacal Parameters.” *Astronomy and Astrophysics*, Feburary 2015.

Team B-Pol. *Introduction.* 2007. http://www.b-pol.org/index.php (accessed 2014 йил 28-August).

Tegmark, Max. “The Angular Power Spectrum of the 4 Year COBE Data.” *Astrophysics Journal*, 1996.

TICRA. *GRASP: Technical Description.* Copenhagen: TICRA Enginerring Consultants, 2005.